

Non-canonical interactions of the Mitogen Activated Protein (MAP) kinases

Ph.D. thesis

Klára Pongorné Kirsch

Biochemical engineering, M.Sc.



Eötvös Loránd University, Faculty of Science,

Doctorate School in Biology, Structural Biochemistry Ph.D. Program

Head of the Doctorate School in Biology:

Prof. **László Nyitrai**, Ph.D., D.Sc.

Head of the Structural Biochemistry Ph.D. Program:

Prof. **Mihály Kovács**, Ph.D., D.Sc.

Supervisor:

Attila Reményi, Ph.D., D.Sc.



Prepared at the:

Institute of Organic Chemistry, Research Centre for Natural Sciences

Budapest, 2021.

Table of Contents

1. Introduction.....	4
1.1 General properties of the MAP kinase pathways.....	4
1.2 The MAP kinase domain with interaction partner recognition sites.....	8
1.2.1 D-motifs.....	9
1.2.2 F-motifs.....	13
1.3 Non-canonical interactions of MAPKs.....	15
1.3.1 Bidentate interactions.....	16
1.3.2 Three-dimensional docking to the DRS and FRS.....	17
1.3.3 New interaction surfaces in the MAPK.....	18
1.3.4 Kinase-kinase complexes.....	19
1.4 Phospho-regulation of the MAPK substrates.....	23
1.4.1 The position of the phosphorylation sites relative to DRS or FRS in substrate proteins.....	23
1.4.2 Proximity-induced catalysis – case studies from the ETS transcription factor family.....	23
1.4.3 Multi-site phosphorylation driven by docking sites.....	24
1.5 An AP-1 transcription factor – ATF2.....	25
1.6 A microtubule associated protein - DCX.....	29
2. Aims.....	32
3. Material and Methods.....	33
3.1 Protein expression and purification.....	33
3.2 Protein-protein binding assays.....	35
3.3 Kinase assays.....	35
3.4 NMR spectroscopy.....	37
3.5 HADDOCK modeling.....	38
3.6 Protein crystallization and X-ray structure solution.....	40
3.7 Protein sample preparation for SAXS and modeling.....	42
3.8 Cell culture.....	43
3.9 Cell-based protein-protein interaction assays.....	44
3.10 Transcription activation assays.....	45
3.11 Simulation of TAD phosphorylation.....	46
4. Results.....	49
4.1 Characterization of the JNK-ATF2 interaction.....	49
4.1.1 Evolutionary sequence analysis of ATFs and JUNs.....	50
4.1.2 Zn-finger dependent interaction of ATF2 with JNK.....	50
4.1.3 Structure determination of the JNK-ATF2 complex.....	52
4.1.3.1 NMR spectroscopy.....	52
4.1.3.2 <i>In silico</i> modeling and model validation of the ATF2-JNK complex.....	54
4.1.3.3 Crystal structure of the ATF2-JNK complex.....	55
4.1.4 Activation of ATF2 by JNK in living cell.....	56
4.2 p38 as an activator of ATF2.....	59
4.2.1 Phosphorylation dependent interaction of p38 and ATF2.....	59
4.2.2 JNK phosphorylation attenuates p38-SPFENEFF motif binding.....	62
4.2.3 Structural basis of p38-ATF2 binding.....	63

4.2.3.1 X-ray structure of the p38-SPFENEFF motif complex.....	63
4.2.3.2 Analysis of the N-terminal cap of the FENEFF helix in ATF2.....	64
4.2.3.3 HADDOCK model of the bipartite interaction of ATF2 and pp-p38.....	66
4.2.4 Specificity determining factors of ATF2 phosphorylation among MAPK-s.....	67
4.3 Co-regulation of ATF2 activity by JNK and p38.....	69
4.3.1 Transcriptional activation by two MAPKs.....	69
4.3.2 Quantitative modeling of MAPK mediated ATF2 TAD phosphorylation.....	71
4.4 D-motif mediated interaction of JNK and DCX.....	75
5. Discussion.....	81
5.1 Non-canonical interactions of MAPKs at the DRS and FRS.....	81
5.2 Non-canonical interactions enable fine-tuned activation of phosphoswitch motifs in MAPK substrates.....	86
6. Acknowledgment.....	91
7. Summary.....	92
8. Összefoglalás.....	93
9. References.....	94
10. Publication list.....	107
11. Appendix.....	108

1. Introduction

The human cell is composed of an extremely complex molecular network of nodes (protein, DNA, RNA), edges (molecular interactions) and reactions (e.g. post-translational modifications). This network is very flexible, capable of adapting to different environmental cues by varying node composition, creating new interactions or modifying reaction rates. Protein kinases are one of the most important nodes in the cellular network and they catalyze the phosphoryl transfer from ATP to serine, threonine or tyrosine amino acids of their substrates. Phosphorylation of a particular region can result in increased enzymatic activity (e.g. in substrate kinases) or affects binding to other molecules (phosphoswitches). In the lowest level of the signaling pathway, transcription factors often respond to pathway activation by using phosphoswitches that enable them to bind to cofactors, ultimately leading to increased transcription of a specific gene [1]. After pathway activation the molecular network returns to resting state because of phosphatases mediating dephosphorylation. Mitogen-activated protein kinases (MAPKs) are ubiquitous nodes in the human molecular network, as they mediate responses to growth factors, various stress signals, or proinflammatory cytokines [2]. Misregulation of MAPK pathways are present in cancer, autoimmune and neurodegenerative diseases [3]. However, the way MAPKs specifically recognize their activators (upstream kinases), de-activators (phosphatases) and substrates is not fully understood.

There have been 50,886 human 3D protein structures deposited in the RCSB PDB database to this day, and approximately half of them represent a protein-protein complex [4]. With this atomic level information on protein-protein interactions, researchers now can better understand the molecular logic underlying the organisation of signaling pathways. In the case of MAPKs, we already know how a dedicated protein-protein interaction groove on the kinase domain can be engaged for binding by a precisely defined motif from the disordered region of the partner protein [5]. These regular or **canonical** interactions play a well-established role in the MAPK interactome. In some – **non-canonical** - cases, the complex formation is structurally unique and cannot be predicted from recent knowledge of sequence analysis. Examination of non-canonical, but biologically relevant interactions, are similarly important, moreover, these can provide more promising targets for interaction-specific inhibitor design.

1.1 General properties of the MAP kinase pathways

The ERK1/2, p38, JNK and ERK5 MAPK pathways are central to evolutionarily conserved signaling pathways present in all eukaryotic cells. General architecture of the three-tiered MAPK cascades are presented in Figure 1. Each MAPK cascade is activated in response to a diverse array of

extracellular signals, and the pathway activation follow the same strict hierarchy of events. Briefly, the external signals, through receptor recognition modules, trigger the relief of MAP3K (MAPKKK) autoinhibition, which then trans-phosphorylate its homodimer in the activation loop. The fully active MAP3K phosphorylate the MAP2K (MAPKK), which then specifically recognize their substrate MAPK. The signal culminates in the dual-phosphorylation of a threonine and a tyrosine residue in the MAPK-activation loop [6]. The propagation of MAPK signals is reduced through the actions of the MAPK specific phosphatases.

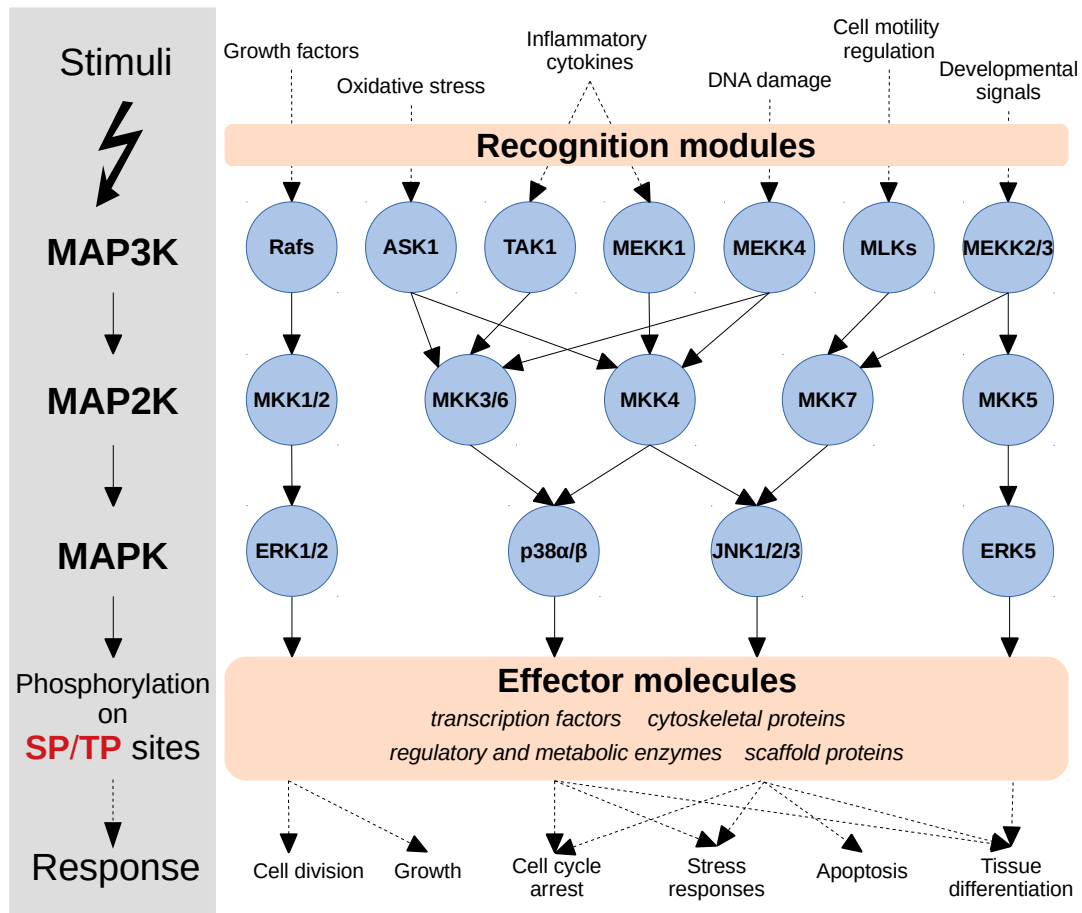


Figure 1 Schematic overview of the human MAPK cascades. The complex architecture of the network can be divided into three main signaling modules (ERK1/2, p38/JNK, ERK5). Black arrows mean direct phosphorylation reactions between the nodes, while the dashed arrows indicate indirect biological effects.

Recognition modules for each pathway consist of multi-protein complexes of cell surface receptors specific to different extracellular stimuli. The well-known ERK1/2 (extracellular-signal-regulated kinase 1/2) pathway responds to growth factors (e.g. epidermal growth factor, EGF) and

mitogens directly through receptor tyrosin kinases (RTKs), inducing cell growth and differentiation. In contrast, the slightly overlapping and more complicated p38/SAPK (stress-activated protein kinase) and JNK (Jun N-terminal kinase) kinase modules respond to extracellular and intracellular stress. Different abiotic stressors (UV->DNA damage, ionizing radiation, heat, oxidative stress, osmotic stress), inflammatory cytokines and developmental factors trigger their pathways to induce apoptosis, inflammation, cytokine production or differentiation and control survival [7]. Apart from cell membrane receptors, MAP3K activation may also be induced by intracellular proteins, e.g. by GADD4 which is expressed after DNA damage and it activates the MEKK4 MAP3 kinase [8]. Crosstalk between the JNK and p38 pathways are important regulatory mechanism involved in many cellular processes, but JNK1/2/3 kinases are more associated with cell death and apoptosis in general, while p38 isoforms (α, β, γ and δ) are more involved in inflammatory response. They are differentially expressed in distinct tissues, so their individual effect is cell-type specific. JNK expression is critical for the central nervous system, while p38 isoforms are particularly important in muscle development[9–11]. The ERK5 pathway is less characterized, and its biological role is quite distinct from the other MAPK pathways. Its activity plays a role in endothelial differentiation, vasculogenesis and embryonic heart development [12].

The MAPKs transfer the signal to the effector molecules by phosphorylating them on serine or threonine followed by a proline (S/TP motif, will be explained below). Many effector molecules are transcription factors that can induce the expression of specific genes by recruiting the general transcription machinery following MAPK mediated phosphorylation at specific sites referred to as phosphoswitches [13]. Phosphorylation may enhance ubiquitin-mediated degradation of the substrate molecules, as was described in the case of a p38 dependent phosphodegron in PGC-1 α protein [14]. Cytoskeletal protein phosphorylation by JNK can affect organization of the cytoskeleton, because of their altered binding affinity to actin or tubulin filaments [15]. Effector molecules can also be enzymes, like the MAPK activated protein kinases (MAPKAPK), involved in continuing signal transduction towards their nucleic target [16].

From a structural point of view, MAP kinases belong to the ancient family of CMGC protein kinases together with cyclin-dependent kinases (CDKs), glycogen synthase kinases (GSKs), CDK like kinases (CLKs) and dual-specificity tyrosine-regulated kinases (DYRKs). CMGC kinases catalyze phosphorylation of a serine or threonine residue preferably followed by a proline, and share a conserved architecture and catalytic mechanism with other kinases [17]. Briefly, the kinase (or catalytic) domain has a characteristic two-lobed (N- and C-lobe) structure, with a deep catalytic and ATP binding core between the two lobes (Figure 2). A hinge region connecting the two lobes

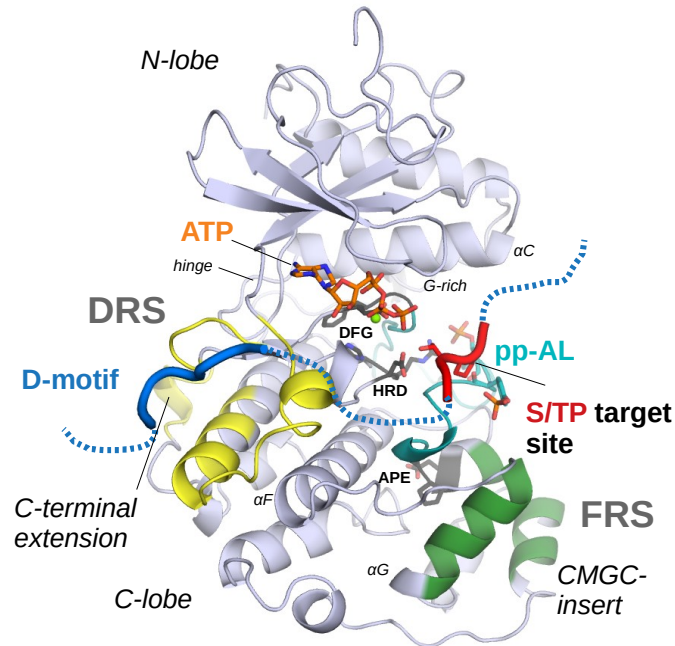


Figure 2 MAP kinase architecture with the active site and modular docking sites. The theoretical model of active ERK2 during the act of substrate phosphorylation. The model of DCC peptide binding to double-phosphorylated ERK2 was prepared using PDB ID: 2ERK, 1GOL, 3O71 and 2WO6. DCC D-motif is blue and connected with DCC phosphorylation site (red) with dashed line. Double-phosphorylated activation loop (pp-AL) of the kinase is cyan, while the DFG, HRD and APE motif are black. The DRS docking site (yellow) is occupied in the model, while the FRS (green) is free.

participates in hydrogen bonding with the adenine ring of the ATP, while the glycine rich (G-rich) loop from the N-lobe serves to orient the nucleotide phosphate groups to the correct position for phosphoryl transfer. The activation loop (AL) of the kinase is an intrinsically disordered region (IDR) just below the ATP binding site, responsible for regulating the kinase activity. In case of MAPKs, the AL contains a characteristic TxY motif, which needs to be phosphorylated by an upstream kinase on both T and Y. This results in a disorder-to-order conversion of the AL, locking the kinase domain in a catalytically

competent conformation. For an optimal orientation of the S/T target site, a shallow substrate binding pocket is formed by phospho-Y intramolecular interactions and supported by the APE motif from the bottom, that can be accommodated by a proline residue at +1 position to S/T target site. Hence we often call the MAPK-s (and other CMGC kinases) as “proline directed” kinases. The phosphoryl-transfer involves highly conserved short motifs from the N-lobe: the DFG motif aspartate at the AL N-terminus coordinates magnesium ion(s) to the active site, the HRD motif aspartate (in the catalytic loop) acts as a catalytic base deprotonating the optimally placed hydroxyl group of serine or threonine substrate. Two conserved lysines from the catalytic loop and the β -sheet together with the magnesium ions act as an electron withdrawing group for the γ -phosphorous atom. The perfectly aligned active site with the substrates and cofactors catalyzes a nucleophilic attack on the γ -phosphate group of ATP and carry out the phosphoryl transfer reaction to the peptide S/TP site [18,19].

As explained above, MAPKs can phosphorylate S/TP motifs, but this motif cannot provide any specificity, due to the high occurrence of this motif in disordered regions in the proteome. Moreover, this motif is too short to bind with high affinity and the K_m (Michaelis constant) of the reaction is usually very weak ($>100 \mu\text{M}$), which means that the phosphorylation is very inefficient [20]. Therefore, as in the case of many kinases, MAPKs use additional protein-protein interactions to enhance the possibility of the phosphorylation by dragging the substrate in close proximity to the active site [21]. This mechanism - also known as proximity mediated catalysis – utilizes the so called docking sites remote from the catalytic sites [22]. MAPKs use their docking patches in various ways, not only for engaging substrates, but to specifically recognize their activating MAPK kinases (MAPKKs), and inactivating phosphatases and other regulatory and scaffold proteins [23].

1.2 The MAP kinase domain with interaction partner recognition sites

MAPKs phosphorylate their substrates on Ser/Thr-Pro target motifs (S/TP), but efficient phosphorylation requires at least one distinct protein-protein – so-called “docking” - interaction [20]. Docking is quite common in several other kinases as well. CDK kinases and PLK (Polo like kinases) use a distinct domain for substrate recognition [24,25]. Although MAP kinases do not have another domain for docking, they have a unique C-terminal extension in the kinase domain, which is not available in other CMGC kinases. This extension is part of a unique patch for substrate binding. This modular recognition system is called the docking-groove (or D-motif recruitment site, DRS), which is capable of binding short linear interaction motifs (SLiMS) with a specified consensus sequence. These motifs (docking or D-motifs) are embedded in an intrinsically disordered protein region (IDR) of the

substrate and comprised of positively charged and hydrophobic amino acids [5]. Another – functionally independent - recognition site is the F-motif recruitment site (FRS), located at the opposite side of the kinase compared to the DRS. The FRS binds phenylalanine containing F(xFP)-type linear motifs with increased affinity if the MAP kinase is double-phosphorylated [26,27].

1.2.1 D-motifs

The MAPK specific D-motifs - also known as kinase interaction motif (KIM), δ -domain or “Docking site for ERK and JNK, LXL” (DEJL) - are located in an IDR region of the MAPK partner protein. If the partner is a substrate, then the motif is located N-terminally from the phosphorylation target site. The D-motifs recognize an ancient surface on MAPK, conserved from yeast to human, which is on the backside of the kinase compared to ATP binding pocket.

Common and highly similar feature of the DRS in each MAPK paralog is a charged CD region and three hydrophobic binding grooves, namely φ_A , φ_B (upper pocket) and φ_L (lower pocket). Conversely, a loosely defined D-motif contains one or more positively charged amino acids (θ), followed by a linker and three alternating hydrophobic residues (φ). They can be described with the following common D-motif sequence : $\theta_{(1-2)}-X_{(0-5)}-\varphi_L-X_{(1-2)}-\varphi_A-X-\varphi_B$ (x denotes any amino acid) Figure 3. From the ~20 D-motif-MAPK X-ray structures available so far we know that many variations of canonical D-motif sequences exist, allowing MAPK-binding partners to occupy the DRS in various binding modes related to the difference in kinase surface topography and charge distribution of each MAP kinase family.

Which regions of the DRS are responsible for the specificity of binding? Small, but conserved differences are apparent between MAP kinases by the upper and lower hydrophobic groove. This groove is bordered by $\beta 7$ - $\beta 8$ loop (specificity loop) from the top, a hinge connecting the N and C-lobe from the right, αD - αE loop and helices from the bottom (base) and define the amino acid preference for the core and linker residues in the hydrophobic motif (see Figure 3, left panel). The charged pocket for basic residues are more diverse among MAP kinases. The CD groove, formed by the C-terminal MAPK extension and the C-terminal end of αC , is comprised of 3 acidic residues in the case ERK and p38 the CD groove, but only two in JNK. In p38 and ERK the CD groove is complemented with an other negatively charged patch, the ED region and also a φ_U hydrophobic anchor point between the CD and ED binding sites (Figure 3, right panel). In JNK the ED glutamate is replaced by an evolutionary conserved small polar residue (T164). Moreover, instead of the third negative charge in the JNK CD groove, a basic residue (K83) forms a salt bridge with the E329 from C-terminal extension, and makes

the upper hydrophobic pocket (φ_U) buried. Because of these differences, the JNK docking groove is less charged and topographically narrower than in ERK/p38. Therefore, JNK-specific D-peptides are well-separated from the ERK/p38 (and ERK5) binding motifs, and the intervening region between the hydrophobic and basic residues is shorter than in p38/ERK specific motifs.

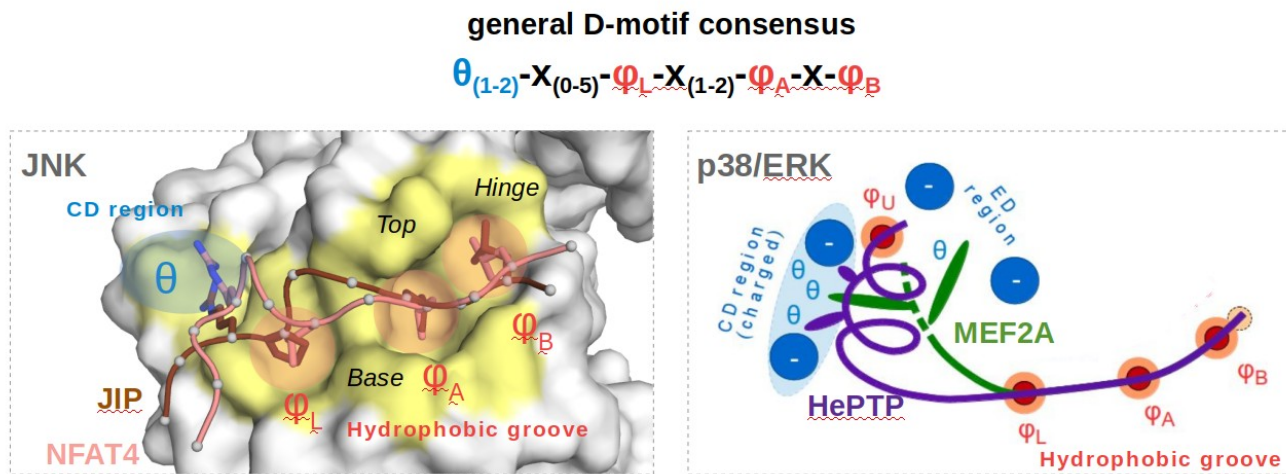


Figure 3 DRS-D-motif interaction. A canonical linear motif specific to MAPK DRS contains basic and hydrophobic residues (blue and red, respectively). In the left, the hydrophobic and CD groove in the JNK-DRS are bound by the D-motif of NFAT4 and JIP (PDB ID: 2XRW, 4H39). Grey dots show CA atoms in the peptide main chain. In the right, schematic figure shows the p38 and ERK2 docking groove from the top with MEF2A and HePTP peptides (PDB ID: 1LEW, 2GPH). Dashed line means invisible part in the crystal structure (modified after Zeke et al. (2015)).

D-motifs specific to JNK occupy the DRS in two known conformations. The NFAT4 types of motifs form a short alpha helix between φ_L and θ by internal hydrogen bonds, which provide optimal positioning for the basic residue to reach the CD groove. In the JIP-type motifs a proline from φ_L directs the arginine to the CD. Compared to JNK, p38 and ERK2 have a wider and more complex charged region which can be engaged by numerous conformations of different D-motif classes (see Table 1). The MEF2A and DCC-type motif classes occupy the p38/ERK2 CD region in an extended conformation, whereas the HePTP, Gra24 and RevD class motifs bind the charged groove in an alpha-helical conformation in various ways. The secondary structure formation of the peptide is assisted by intermolecular (MAPK specificity loop – peptide) and intra-peptide hydrogen bond networks that altogether contribute to affinity and to the specificity to discriminate between p38 and ERK2. These H-bond staples prevent the peptide from binding in an alternative conformation compatible with a non-cognate kinase. In contrast, the MKK6 and DCC peptides (pepMKK6-p38 PDB ID: 2Y8O, pepDCC-

ERK2 PDB ID: 3O71) only go through a disorder-to-order conversion at residues covering the hydrophobic grooves, while the basic residues are invisible in the crystal structure and may adopt multiple conformations, and therefore can not be used to discriminate between p38 and ERK2.

Table 1. Classification of the MAPK DRS binding SliMs. JNK (grey), p38/ERK1/2 (blue) and ERK5 (yellow) specific motifs are grouped based on their loose consensus motifs where basic residues and hydrophobic residues are colored in red and blue, respectively. X-ray structures for each class available are collected and the number of experimentally validated motifs from human are indicated in bracket.

Type	Subtype	PDB ID	Loose consensus	More refined consensus (deposited to ELM database)
JIP1		4H3B 4H39 (30)	θ -P-X-X- φ _L -X- φ _B	[RK]P[^P][^P]L.[LIVMF]
NFAT4		2XS0 2XRW (16)	θ -X-X- φ _L -X- φ _A -X- φ _B	[RK][^P][^P][LIM].L.[LIVMF]
MEF2A	MEF2A	1LEW (8)	θ - θ -X-X- φ _L -X- φ _A -X- φ _B	[RK].{2,4}[LIVMP].[LIV].[LIVMF]
	MKK6	2Y8O (6+2)	θ -X- θ -X-X- φ _L -X- φ _A -X- φ _B	
DCC	DCC	4H3Q (2)	θ ₍₁₋₂₎ -X ₍₂₋₄₎ - φ _L -P-X- φ _A -X- φ _B	[RK].{2,4}[LIVP]P.[LIV].[LIVMF]
	Far-1	2B9J (4)	θ ₍₁₋₂₎ -X ₍₂₋₄₎ - φ _L -X-P- φ _A -X- φ _B	[RK].{2,4}[LIVP].P[LIV].[LIVMF]
HePTP	Ste7	2B9H 2B9I (2)	φ _U -X-X- θ -X ₍₄₎ - φ _L -X- φ _A -X- φ _B	[LIV][^P][^P][RK]...[LIVMP].[LIV].[LIVMF]
	HePTP	2GPH (3)	φ _U -X-X- θ -X ₍₅₎ - φ _L -X- φ _A -X- φ _B	[LIV][^P][^P][RK][RK]G.{4,7}[LIVMP].[LIV].[LIVMF]
GRA24		5ETA (2 from <i>T. gondii</i>)	φ _U -X-X- θ -X ₍₄₎ - φ _L -P-X- φ _A -X- φ _B	[LIV][^P][^P][RK][RK]G.{3,6}[LIVP]P.[LIV].[LIVMF]
			φ _U -X-X- θ -X ₍₄₎ - φ _L -X-P- φ _A -X- φ _B	[LIV][^P][^P][RK][RK]G.{3,6}[LIVP].P[LIV].[LIVMF]
RevD		3TEI 2OZA 2Y9Q (5)	φ _B -X- φ _A -X-X- φ _L -X ₍₄₋₆₎ - φ _U -X-X- θ	[LIVMPFA].[LIV].{1,2}[LIVMP].{4,6}[LIV]..[RK][RK]
MKK5		4IC7	MEF2A-like ?	?

Despite of the fact that D-motifs are highly variable, the available structural and sequence data made it possible to establish consensus sequences for the different motif classes (loose consensus in Table 1). In the work of Zeke et al. (2015), a motif search algorithm was implemented to find new MAPK partners using those consensus sequences. The simple pattern matching procedure from human proteome was complemented with filtering for accessible, unstructured regions in proteins to reduce false positive hits. The ANCHOR algorithm was used to find regions with propensity for disorder-to-order transition in IDR protein regions [28]. This was complemented with compartment-filtering and modeling for structural compatibility with the MAPK surface (by Foldx) [29]. The best motif candidates were tested with an experimental method. Finally, for the validated positive hits, an evolutionary conservation analysis was performed. To examine the newly found and formerly known sequences, a position specific scoring matrix (PSSM) was generated and weighted with an arbitrary evolution conservation score (Figure 4) [30]. This analysis highlighted the privileged role of prolines between φ _L and φ _A in the greater DCC motif class which maintains a short type II polyproline helix

(Figure 4, dark magenta). Proline preference in MEF2A are at +1 position to φ_B is also apparent, and act as an additional hydrophobic contact point (Figure 4, magenta). Moreover, the PSSM matrices suggest that in JIP-type motifs small residues with a hydroxyl group at -1 position to φ_A are enriched, so that to make a H-bond with a JNK specific arginine in the base (Figure 4, green). Based on this work, the precisely curated regular expressions for each D-motif classes were updated in the Eukaryotic Linear Motif (ELM) database in 2018 which is summarized in Table 1 [31].

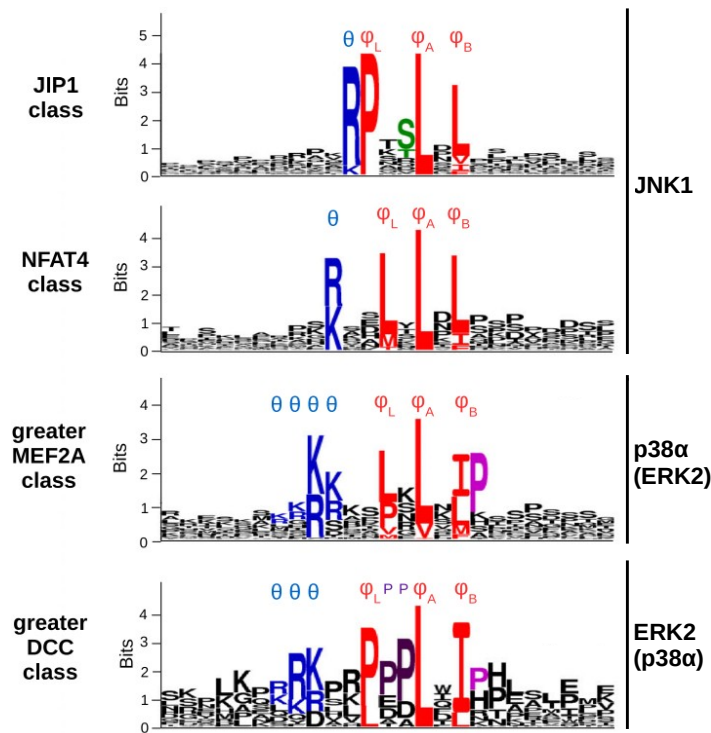


Figure 4 PSSM logos of the four main D-motif classes. The matrices built from experimentally validated human motifs and weighted with evolutionary conservation related score. The logos also highlight the privileged role of prolin (purple and magenta) and polar residues (green) important for enhancing specificity. (modified after Zeke et al. (2015))

Although the major D-motif classes are well explored, some still awaits discovery. Interestingly, the GRA24 *Toxoplasma gondii* has a combination of polyproline-helix motifs from the DCC motif class with a HePTP-like alpha-helical N-terminus which binds to the human p38 [32]. The existence of reversed D-motifs also proves the variability of possible D-motif conformations. Reverse D-motifs are found in the RSK and MAPKAPK kinase families specifically binding to p38/ERK. In their bound

form, they are comprised of an alpha-helix between θ and φ_U and a 3-10 helix between φ_L and φ_U . Specific side-chain interactions help to discriminate between p38 or ERK1/2 [5]. ERK5 forms a distinct MAPK signaling pathway, but unfortunately the number of known ERK5-specific D-peptides are very low. Biochemically examined example is the D-motif from its activator, the MKK5, which is highly specific to ERK5 (PDB ID: 4IC7). The ERK2 DRS is very similar to ERK5 – and the MEF2A peptide is indeed able to bind to both kinases with similar affinity – but some differences in the specificity loop and in the base may provide distinct interaction capacity [33]. Further motif instances are needed to define ERK5 specific consensus sequences.

In summary, the short 7-20 amino acid long D-motifs have large variability in binding at the DRS due to the different intervening regions connecting the anchoring consensus motif positions. The linker regions shape the MAPK specificity profile by forming inter- or intramolecular H-bonds, or by prolines to provide conformational rigidity. Despite all this, structural and biochemical studies highlight the limitations of simple D-motif mediated interactions regarding specificity, although these may be efficiently relieved in the context of full length proteins where other binary interactions also contribute to protein-protein recognition [5].

1.2.2 F-motifs

Another class of canonical MAPK docking motifs is the phenylalanine containing FxF(P) SliM. It specifically binds to a hydrophobic surface located just below the activation loop. The F-motif or DEF motif (“docking site for ERK, FXF”) mediated interactions are less characterized - compared to D-motif - and only a few examples known until this day.

F-type interaction was first identified between ERK2 and transcription factors of the Ets-family, including Elk-1, Lin-1 and Sap-1 by Jacobs et al. (1999) [20]. The binding site for the FxFP containing peptide from Elk-1 was mapped to the pp-ERK2 using hydrogen-deuterium exchange mass spectrometry (HDX-MS) combined with site-directed mutagenesis. This study revealed a distinct hydrophobic pocket (F-recognition site: FRS) which is fully formed only in the active double-phosphorylated form of ERK2. The FRS groove is bordered by the AL from the top, and formed by the APE motif containing α EF helix, the N-termini of the α G helix and the MAPK insert [27]. Using NMR spectroscopy Piserchio et al (2015) identified the critical contacts for the F-motif-FRS interaction of the pp-ERK2-Elk1 complex. Based on these NMR experiments, an ensemble structure of the ELK1 bound form was generated where NMR-based restraints between the two molecules were used in the HADDOCK docking approach. In the HADDOCK model the ELK1 peptide binds to the FRS with the

two phenylalanine side chains buried in two contiguous hydrophobic grooves of FRS (Figure 5A). The first groove (ϕ_1) is formed by the phosphorylated-Y185 - ordered only in the active state of the kinase -, I196 and M197 from the α EF helix (also called as P+1 loop or APE motif) and the N-terminal part of the α G helix. The second ϕ_2 groove is formed by the L232 and L235 from α G helix; L198 from α EF helix; and Y261 and A258 of the α 2L14 helix as part of the MAPK insert. Based on NMR titration data and the structural model, the proline from the FxFP motif is more solvent exposed and relatively unimportant, but residues located N-terminally from the FxFP might participate in an additional interaction with the negatively charged activation loop in pp-ERK [34].

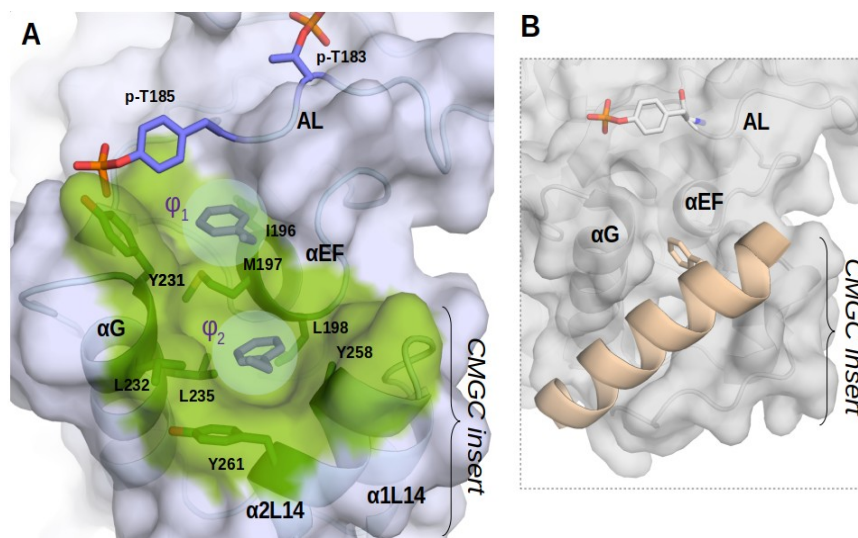


Figure 5 Hypothetic binding of the FxFP motif to the double-phosphorylated ERK2. A) As there are no crystal structure available for FRS-F-motif complex, apo-pp-ERK2 (PDB ID: 2ERK) and findings of Piserchio et al. (2017) were used for drawing the model. The probable position of phenylalanines from F-peptide shown in grey color in the ϕ_1 and ϕ_2 groove of the FRS. B) Activated GSK3 kinase in complex with axin peptide shows a similar interaction patch formed below the activation loop. The phenylalanine from axin is represented as sticks and binds in a ϕ_2 -like groove (PDB ID: 1O9U).

In contrast to the numerous MAPK-D-motif structures, there is no crystal structure available for a canonical FxFP linear motif – MAPK complex to this day.

While the utilization of DRS is only described in the case of MAP kinases, an FRS-like groove is available in other CMGC kinases formed by the CMGC insert, APE region and α G helix. Although both the α 1L14 and α 2L14 segments from CMGC insert are helical in MAPKs, in the case of the other CMGC kinases the α 2L14 region varies, which makes the FRS groove different - bigger and more

flexible - compared to the MAPK binding pocket. This FRS-like pocket has been described in the case of GSK-3 kinase, where a single short helix from the axin scaffold protein (PDB ID: 1O9U) or a helix-turn-helix peptide from FRAT1 (Frequently rearranged in advanced T-cell lymphomas 1, PDB ID: 1GNG) bind to this site by the AL (p-Y216) phosphorylated GSK-3 β (Figure 5B). Similarly to the ELK-1-pp-ERK2 interaction (described above), the bound peptide does not inhibit the GSK kinase activity, so it acts as a modular interaction patch separate from the kinase active site [35,36].

To further highlight the complexity of the MAPK interactome, we already know from previous studies, that numerous biologically relevant MAPK partners exist without bearing canonical linear motifs. These non-canonical interaction partners sometimes combine the interaction with DRS and FRS, perhaps to compensate for non-ideal binding to these docking regions alone. I summarize these intriguing examples in the next chapter and examine their particular interaction mode.

1.3 Non-canonical interactions of MAPKs

Non-canonical partners of MAPK use alternative ways to interact with the canonical docking sites (DRS or FRS) of MAPKs, which are occasionally accompanied by the utilization of a new binding surface on the kinase. In some cases, part of a D-motif can be detected, but it cannot mediate binding alone. In this case, the defective docking motif is complemented with a use of extra motifs or domains to achieve biologically relevant binding. In other cases, instead of using linear motifs, the DRS or FRS interacting elements are completely folded globular domains (**domain-domain interactions**). As in the case of classical D-motifs and F-motifs, other non-canonical IDR binding motifs also undergo **disorder-to-order** conversion upon binding. Sometimes a part of the linear motif constantly scans the MAPK surface, and remains conformationally heterogeneous in their bound state. Those motifs are participating in **fuzzy** interactions with the MAPK, contributing to binding affinity and specificity [37].

We can further categorize the non-canonical interactions according to the number of isolated binding sites on the MAPK surface. Single binding site (or **unipartite**) interactions utilize only one docking site (e.g. in the case of canonical DRS-D-motif interaction; e.g. c-Jun-JNK). For efficient binding, most of the known non-canonical MAPK partners use two well-separated interaction surfaces on the kinase, which we call **bipartite** or bidentate interactions.

Because of the weak or dynamic nature of many non-canonical binding element, sometimes the structure of the protein complex cannot be examined by X-ray crystallography. Therefore various NMR methods or HDX-MS (hydrogen deuterium exchange mass spectrometry) are used to map the binding surface followed by experimental data based model building (HADDOCK, Flexible-meccano).

HADDOCK is a widely used molecular docking framework, as many type of experimental restraints can be incorporated into the docking approach. Flexible-meccano algorithm can be used to generate statistical coil ensemble for IDP regions for further modeling [38,39]. SAXS (Small-angle X-ray scattering) measurements are also useful for investigating the in-solution behavior and conformational diversity of protein-protein complexes with IDR regions. Softwares like the Ensemble refinement of SAXS (EROS) were developed to generate and optimize ensembles with multiple disordered regions to fit the scattering data [40].

In the next sub-chapters I provide detailed description of already known non-canonical MAPK interactions and summarize the interaction modes in Figure 6 and Table 1.

1.3.1 Bidentate interactions

The classic example for non-canonical MAPK interaction is the Elk1+pp-ERK2. Elk-1 interact with pp-ERK2 with its canonical D- and F-motif in a bipartite way. Whereas the Elk-1 D-motif (KGRKPRDLEL) can be bound by JNK and ERK2 as well, its F-motif is specific to the double phosphorylated ERK2 FRS (described earlier). Deletion of both D or F-motif affect the binding affinity and the kinetic parameters of the phosphorylation of target sites located between them [41]

Interestingly, despite the absence of canonical D- and F-motif, Ets-1 transcription factor also engages both the DRS and the FRS of ERK2 with its two suboptimal regions. The N terminus of Ets-1 interacts with a hydrophobic part of the ERK2 DRS by a short hydrophobic motif (Φ_A -X- Φ_B) with low intrinsic affinity. The C-terminal globular Pointed (PNT) domain of the Ets-1 engages the FRS. Only a partial occupancy is predicted for the Φ_2 groove by a PNT phenylalanine. This groove is solvent exposed in the inactive kinase as well, therefore this bipartite binding ($K_d \sim 30 \mu\text{M}$) is independent from the kinase activation state [42].

Bidentate interaction of PEA-15 (15 kDa phosphoprotein enriched in astrocytes) with ERK2 was captured in a crystal structure, where the N-terminal death effector domain (DED) utilizes the FRS and a partial reverse D-motif binds to the DRS. The DED domain accommodates the FRS in an unusual way without any hydrophobic residue sitting in the ϕ_1 or ϕ_2 grooves, and more importantly forces the ERK2 activation loop into an inactive conformation. PEA-15 binds to ERK2 with relatively high affinity ($K_d \sim 0.2 \mu\text{M}$) and is able to sequester the phosphorylated ERK2 pool by protecting it from dephosphorylation, but at the same time it also inhibits the ERK1/2 activity. Therefore, PEA-15 was promoted to act as a tumor-suppressor in the MEK-ERK pathway [43].

1.3.2 Three-dimensional docking to the DRS and FRS.

Three-dimensional docking to MAPKs is a common feature for the dual-specificity phosphatase (DUSP or MKP) family consisting of 10 members. They are the most important phosphatases for the downregulation of the MAPK activity as they have the ability to dephosphorylate both p-Y and p-S/p-T residues. The specific interaction with their cognate MAPK substrate is defined by their folded domains: KBD (kinase binding domain) and CD (catalytic domain) engage the DRS and FRS site of the kinase, respectively. They do not utilize both interaction site in most cases, but bipartite interaction also occurs.

MKP7 and MKP5 are JNK/p38 specific phosphatases from the DUSP family. Biochemical and cell-based studies clearly show that MKP7 uses its CD domain, but not the KBD domain for JNK binding. Crystal structure of MKP7-CD in complex with JNK reveals the interaction through a contiguous surface involving C-terminal helices of MKP7-CD and α G and α 2L14 helices in the FRS from the JNK1 C-lobe. The aromatic ring of F285 on α 5 helix of MKP7 is buried in the same ϕ 2 hydrophobic pocket of FRS, as it was defined for the binding of linear FxFP motifs. The binding is stabilized by additional hydrophobic contacts, hydrogen bonds and salt bridges provided by different regions of MKP7. Moreover, another phenylalanine (F215) of MKP7 seems to be an important anchoring point to α EF/ α F loop and α 2L14 N-terminal region. Similarly, MKP5 also binds JNK with only the CD-FRS interaction, but with lower affinity due to the less favorable leucine at a key position instead of the bulky F285 (optimal for the FRS ϕ 2 groove), and due to weaker interactions at other hydrophobic positions [44].

In contrast, p38 recruits MKP7/MKP5 phosphatases to the DRS site by their rhodanese-like KBD domains. The crystal structure of a complex between the MKP5-KBD and p38 α revealed a distinct interaction mode for MKP5. In contrast to the canonical D-motif binding mode, separate helices of the KBD (α 2 and α 30) engage the p38 α docking site in a three-dimensional way [45]. NMR and biochemical studies indicate that MKP7-KBD may interact with p38 α in a similar way as MKP5-KBD [46]. Contrary to MKP5, MKP7 is able to establish bidentate interaction with p38 utilizing the CD-domain-FRS binding as well.

The ERK specific MKP3 phosphatase has been described as intrinsically inactive, because in the apo state it samples an inactive conformation of the PTPase loop in the CD domain. Similarly to MKP7-CD+JNK interaction, its FxP-motif (³³⁴FNF³³⁷) is essential for the binding to the F-site of unphosphorylated or phosphorylated ERK. Moreover, molecular dynamic simulations showed that

interaction with ERK triggers a network of allosteric changes in the CD domain promoting an inactive to active transition of the catalytic site [47]. The KBD domain of the MKP3 was also identified to contribute to the binding affinity and specificity. Although an X-ray structure of a D-motif-like peptide from MKP3-KBD bound to ERK2 exists (PDB ID: 2FYS) [48], it is unlikely that this structure is biologically relevant in the context of the well-folded rhodanase domain (KBD). NMR titration of ^{15}N labeled MKP3-KBD with ERK together with biochemical experiments and sequence analysis suggest that MKP3-KBD binds to ERK2 in a similar manner as MKP5-KBD binds to p38 α [49,50]. In conclusion, MKP3 utilizes a bipartite recognition mechanism for ERK2 with two globular domains.

Compared to the proposed canonical FRS-F-site interaction, MAPK-MKP studies showed that the F-site can bind the CD domain regardless of the phosphorylation status of the kinase, probably because the $\phi 2$ groove is available in the inactive state as well. The catalytic structure of KAP phosphatase with phospho-CDK2 (PDB ID: 1FQ1) is strikingly similar to the MKP7-CD+JNK complex with an isoleucine sitting in the $\phi 2$ groove analogue. This structure gives an explanation how the kinase activation loop with the phosphorylated residues sample a conformation to reach the catalytic site of the phosphatase [51].

1.3.3 New interaction surfaces in the MAPK

Some of the non-canonical binding partners use an additional surface (besides of DRS or FRS) on the kinase to enhance binding affinity or specificity, which in some cases has an allosteric effect on the kinase structure.

Intriguingly, the binding of a partner may lead to the auto-phosphorylation of the MAP kinase by inducing rearrangement of the activation segment. The first example is the yeast Fus3-Ste5 complex where the scaffold protein Ste5 binds both the N- and C-terminal lobe of Fus3 (ERK ortholog) kinase with its 28 residue peptide in a bipartite manner. Here the first part of the linear peptide binds to the DRS, whereas another part integrates itself to and stabilizes a β -sandwich at the Fus3 N-terminus. The linker length between the two peptides are naturally engineered to obtain optimal hinge motion between the N- and C-terminal lobe of the kinase, therefore promoting maximum enhancement on autophosphorylation [52].

In case of p38 α , bipartite binding of a peptide from TGF β -activated kinase 1 binding protein 1 (TAB1) causes autophosphorylation *in cis* using a different molecular mechanism. The C-terminal part of the TAB1 peptide engages the DRS, and the N-terminal part binds to a hydrophobic patch of αF , αH

and α H- α 2L14 in the C-lobe of p38 α just below the DRS. The binding of the two peptide regions cause the reorientation of several structural elements of the kinase anchored to the α F helix, resulting in N- and C-lobe closure with a dramatically increased affinity of p38 α for ATP. The allosteric modulation also displaces the TGY motif toward to the catalytic site enabling the *cis*-autophosphorylation reaction [53,54].

Interestingly, similar part of the C-lobe in p38 α is accommodated by a kinase specificity sequence (KIS) of HePTP (hematopoietic tyrosine phosphatase) and MKK4 by a fuzzy interaction, although they show no sequence identity with TAB1 or with each other in this region. The KIS regions that are located immediately C-terminal to the regular D-motif contribute to stronger binding affinity and specificity by its hydrophobic amino acids. NMR studies indicate, that while the docking site behavior is rigid in the complex, the KIS sequence displays fast dynamics and samples several conformations in a dynamic equilibrium on the surface of p38 α as a fuzzy complex [55,56].

1.3.4 Kinase-kinase complexes

While most MAPK substrates have a phosphorylation sites in a longer IDR region, some protein substrates, such as kinases, are folded, and have phosphorylation sites in a loop between structural elements. MAPK-activated protein kinases (MAPKAPKs) are well known examples of this group, with crystal structures available for the C-terminal kinase domains of RSK (Ribosomal protein S6 kinase) with ERK2 (PDB ID: 4NIF), as well as MK2 (MAP kinase-activated protein kinase 2) with p38 (PDB ID: 2OZA, 6TCA). They both interact with MAP kinases using a reverse D-motif, and additional domain-domain contacts contribute to a well-defined quaternary structure forming an efficient pre-catalytic complex. The ERK2-RSK crystal structure shows that the RSK1 kinase domain forms a face-to-face antiparallel heterodimer with the ERK2 kinase domain, and apart from the DRS-D-motif, an interface forms between the glycine-rich P-loop of ERK2 and the APE motif of RSK1. Molecular dynamics simulations suggested that upon pathway activation this arrangement could easily shift into a catalytically competent state, where the RSK1 activation loop (with a TP motif) flips into the pp-ERK2 substrate binding pocket [57].

While the quaternary arrangement of ERK2-RSK1 complex is always antiparallel and independent of the phosphorylation state of ERK, the p38-MK2 complex can be captured in two different conformations. The un-phosphorylated p38-MK2 (PDB ID: 2OZA) form a parallel complex, where the N-lobes of two kinase domains face each other [58]. In this conformation the activation loop (AL) of MK2 with the T222 phosphorylation site is unable to reach the p38 active site. This inactive

parallel state is stabilized by a unique interaction patch between MK2 inhibitory helix and p38 R57 in the β 3- α C loop, which cannot form in the case of ERK2-RSK1. After activation of p38, the heterodimer ensemble is dominated by an anti-parallel and AL phosphorylation-competent state. This anti-parallel orientation, and therefore MK2 activation can be inhibited by a small molecule inhibitor specific to the p38-MK2 complex (PoA). The ternary complex of pp-p38+MK2+PoA inhibitor (PDB ID: 6TCA) suggests that the parallel conformation can exist in the active double-phosphorylated form of p38 as well, so that other auxiliary regulation sites (T272 and T344) important for MK2 function can be in position to get phosphorylated [59].

From the currently known non-canonical cases listed above we can conclude that the diversity of the non-canonical interactions of the MAPKs are not only driven by enhancing specificity or binding affinity but to also to regulate the signal-response curve of the signaling pathway. These unusual interactions can lead to allosteric activation (e.g. p38-TAB1) or can sequester the MAPK in the active state (ERK2-PEA15).

Except from the ELK1 transcription factor, which consists of a canonical D-type and an F-type motif, none of the presented structural assemblies could be predicted by current bioinformatics methods.

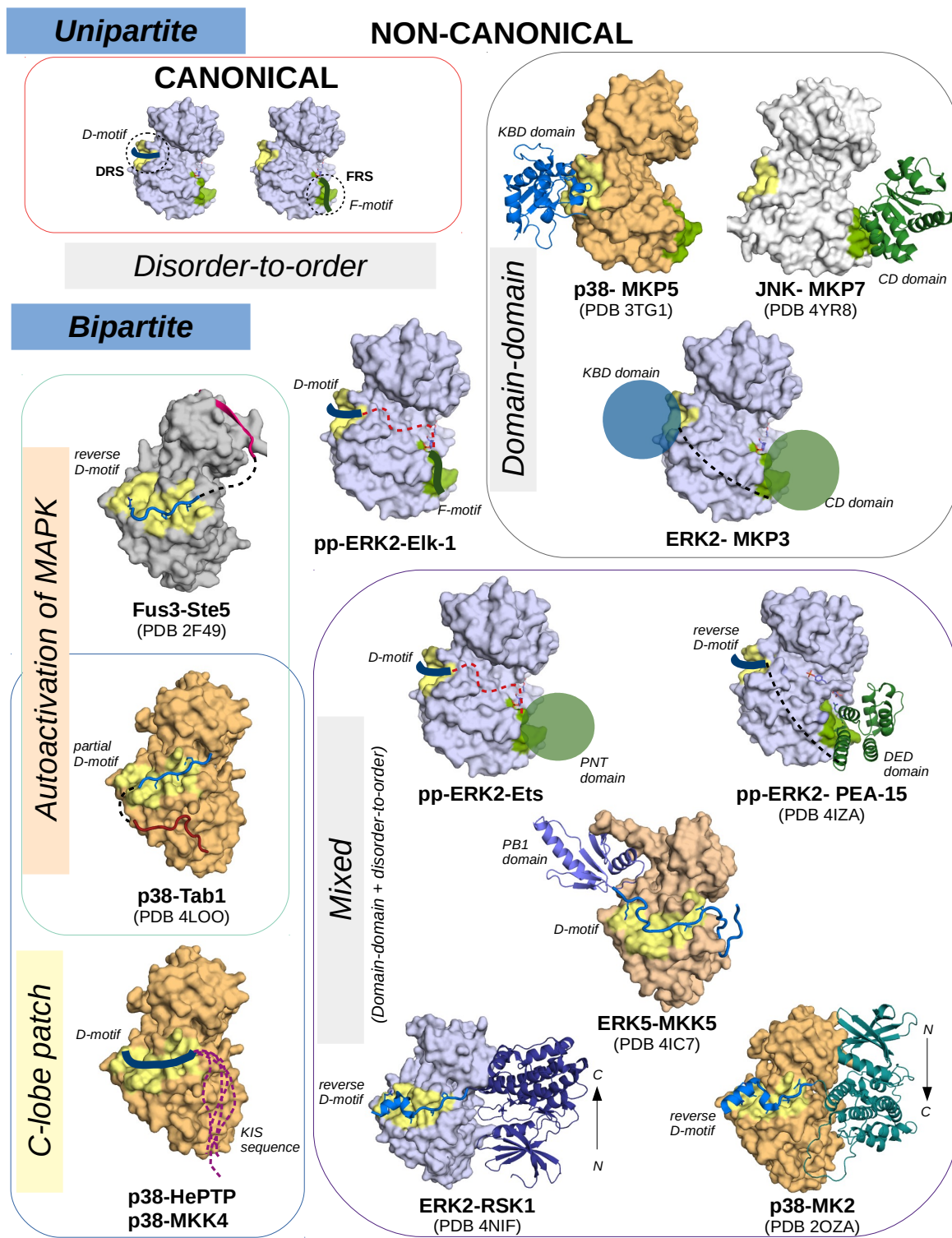


Figure 6 Non-canonical interactions of the MAP kinases. X-ray structures of complexes - if available – are shown in the figure with PDB ID. Hand drawn parts are prepared based on other structural biology methods. Yellow and green patch on the MAPK surface indicate DRS ad FRS, respectively. Black dashed line means disordered connecting regions. Red dashed lines means disordered regions with multiple phosphorylation sites. Purple dashed line means fuzzy or disordered region.

Table 2 Non-canonical interactions of the main MAPK families

MAPK	Partner	Interaction mode	Interaction surface [MAPK] - [Partner]	Experimental method/Modeling software	Ref.
JNK					
JNK1	MKP7	domain-domain	[extended FRS] – CD	X-Ray (PDB ID: 4YR8)	[44]
p38					
p38 α	MKP5 (DUSP10)	domain-domain	[extended DRS] – [α 2, α 3, (α 4?) helices of KBD]	X-Ray (PDB ID: 3TG1)	[45]
p38 α	MKP7 (DUSP16)	domain-domain	[extended DRS] – [α 2, α 3, α 4 helices of KBD]	NMR/HADDOCK	[46]
p38 α	MKK4	disorder-to-order + fuzzy	[DRS+ C-lobe] - [D-motif + KIS sequence]	NMR/Flexible-Meccano	[56]
p38 α	HePTP	disorder-to-order + fuzzy	[DRS+ C-lobe] - [D-motif + KIS sequence]	NMR/SAXS/EROS	[55]
p38 α / pp-p38 α	TAB1	bipartite disorder-to-order	[DRS + C-lobe (α F, α H, α H- α 2L14)] - [D-motif + peptide]	X-ray (PDB ID: 4LOO, 5NZZ)	[53,54]
p38 α / pp-p38 α	MK2	domain-domain + disorder to order	[DRS + kinase domain]- [rev-D-motif + kinase domain]	X-Ray (PDB ID: 2OZA, 6TCA), SAXS	[58,59]
ERK1/2					
ERK2	MKP3	domain-domain	[DRS + FRS] – [KBD + CD]	MD	[47–49]
pp-ERK2	HePTP	disorder-to order + domain-domain	[DRS + activation loop-F-site?] – [D-motif + CD]	X-Ray (PDB ID: 2GPH), SAXS/EROS	[60]
ERK2/ pp-ERK2	PEA-15	bipartite domain-domain + disorder to order	[DRS + FRS] – [DED domain + rev-D-motif]	X-Ray (PDB ID: 4IZA, 4IZ5, 4IZ7)	[43]
pp-ERK2	ELK1	bipartite disorder-to-order	[DRS + FRS] – [D-motif + F-motif]	HX-MS, NMR/HADDOCK	[22,27]
ERK2	Ets-1	bipartite domain-domain + disorder to order	[DRS + FRS] – [partial D-motif + PNT]	NMR/HADDOCK	[42]
ERK2	RSK	domain-domain + disorder-to-order	[DRS + kinase domain]- [rev-D-motif + kinase domain]	X-Ray (PDB ID: 4NIF)	[57]
Other					
ERK5	MKK5	domain-domain + disorder-to-order	[N-lobe + DRS] – [PB1 + D-motif]	X-Ray (PDB ID: 4IC7)	[33]
Fus3	Ste5	bipartite disorder-to-order	[N-lobe β -sheets + DRS] - [peptide + rev-D-motif]	X-Ray (PDB ID: 2F49)	[52]

1.4 Phospho-regulation of the MAPK substrates

1.4.1 The position of the phosphorylation sites relative to DRS or FRS in substrate proteins

In MAPK substrates the phosphorylation target site (S/TP) is differently positioned from the D-motifs and F-motifs due to the topologically different locations of the DRS, active site and FRS in the kinase. D-motifs are usually located 10-50 amino acids N-terminally from the S/TP, while F-motifs are located 10-20 amino acids C-terminal from the target site [61]. A single substrate protein may contain a D-motif or an FxFP motif or even both. Since the FxFP motifs bind independently on a different surface of the MAPK, they can combine with D-motifs in the same polypeptide chain and act synergistically to enhance phosphorylation [41].

1.4.2 Proximity-induced catalysis – case studies from the ETS transcription factor family

Multiple phosphorylations directed by distinct binding sites were extensively studied in the case of ELK-1-ERK2 complex. It has been known for a long time that almost all of the binding energy for the association of the phosphoacceptor T/SP motif with ERK2 originates from the interaction between DRS-D and FRS-F motifs. The T/SP motif makes an insignificant contribution to the binding affinity [62]. The phosphorylation efficiency of the particular (S/T)P site is a function of the number, type, position and arrangement of docking sites which was first described by Fantz et al. (2001) [41]. Based on those observation a mechanism – called proximity induced catalysis – was proposed, which state that the docking interactions serve to increase the local concentration of the phospho-acceptor site near the kinase active site [22]. The enhanced local concentration increases the formation of a pre-chemistry ensemble where the S/TP motif is bound optimally at P+1 site for phospho-transfer and thereby the possibility of phosphorylation is enhanced [63].

Enzyme kinetic studies with the ETS transcription factor and ERK2 showed that T38 is optimally placed to have the highest catalytic efficiency (k_{cat}/K_M) with high catalytic rate (k_{cat}) with respect to the D-motif and the FRS binding PNT domain. Mutant constructs with TP motifs shifted 1-3 amino acids upwards or downwards had decreased catalytic rate. Deletion of either the D-motif or the PNT domain increased the K_M (5 and 28 fold, respectively), but essentially did not change the k_{cat} . These results suggest that k_{cat} is dependent on the intrinsic flexibility around the phospho-acceptor site and the relative position from docking regions, while K_m mainly originate from the binding affinity of the docking motifs. Notably the mutation of proline to alanine in the -38-TP-39 site negatively affects both k_{cat} and K_m , with increased flexibility of the substrate at the P+1 position [42,64]. These

observations are only true if the binding to DRS, FRS and active site were not allosterically coupled, which is proven in the case of ERK2.

Piserchio et al. (2015) calculated the exchange rate of the binding from ^{15}N relaxation dispersion curves of Elk1-F-motif bound to ppERK. They also made an elegant estimation from the k_{off} and k_{cat} values that only 1 of 800 docking events result in productive catalysis [34]. This analysis supports the distributive phosphorylation theory, which means that the substrate protein dissociates after every phosphorylation event and has to rebind for the phosphorylation of another target site. Distributive phosphorylation (with little or no processivity) was described in the MKK6/p38/ATF2 signaling module as well [65][66]. Generally, processivity (multiple phosphorylation without dissociation) leads to a hyperbolic dose-response curve, while distributive kinetics generate an activation threshold in the curve of multi-target site substrates. Whether a reaction is distributive and processive depends on the ratio of k_{cat} and k_{off} [67]. Many biochemically characterized MAPK-substrate interactions suggest that they have been tuned to have fast k_{off} rate, enabling the switch-like response for the signaling pathway [68].

1.4.3 Multi-site phosphorylation driven by docking sites

The ELK-1 is one of the most characterized example how a transcription factor responds to environmental cues through the multi-site phosphorylation in its TAD domain. Similarly, most of the transcription factors use their TAD domain distinct to their DNA binding domain (DBD) to affect cell physiology. Common feature of the TAD domains that they are unstructured and contain multiple phosphoswitches that can enable regulated binding to different cofactors [13].

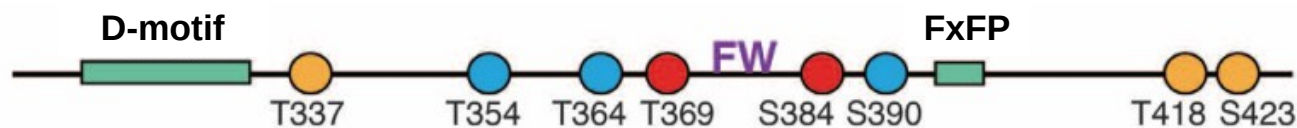


Figure 7 Phosphorylation sites in ELK1 transactivation domain (modified after Mylona et al. (2016)). Most of the regulation sites is lying between D-motif and F-motif. Red, blue and yellow color mean fast, intermediate and slow S/TP phosphorylation sites. FW indicates the residues essential for Mediator association.

For ELK-1, the apparent rate of the phosphorylation depends on the relative location of the phospho-target site compared to the D-motif and F-motif. Faster phosphorylated sites (red) are located in the conserved central part of the TAD and are essential for transcriptional activation (Figure 7). These sites are in close proximity to the FW hydrophobic motif required for Elk-1 interaction with

Med-23 from the RNAII polymerase binding Mediator coactivator complex [69]. Interestingly, the slowly phosphorylated residues (yellow) inhibit Mediator recruitment suggesting that the phosphorylation of ELK-1 TAD by ERK is self-limiting [70].

Multi-site phosphorylation of the AP-1 transcription factors by MAP kinases (such as c-Fos, ATF2 or c-JUN) in their TAD (trans-activation domain) is also necessary for their transcriptional activity [71–73]. The molecular mechanism underlying the phosphorylation mediated coactivator binding is less understood compared to the ELK-1-TAD example. For the ATF2/cJUN heterodimer, the p300/CBP – a cofactor protein with histone acetyltransferase activity – is an important coactivator, but its binding is not mediated by the TAD [74,75]. Several studies suggest that p300/CPB cooperates with other coactivators, like the viral oncoprotein E1A to induce the AP-1 mediated transcription. Nevertheless, direct physical contact of a human coactivator protein with the activated ATF2 or c-JUN phosphoswitch in the TAD has not been found so far [76]. We know that in the c-JUN N-terminal TAD domain an NFAT4-type D-motif regulates phosphorylation of S63 and S73 sites solely by JNK [77]. Interestingly, the c-JUN heterodimerization partner, ATF2 (Activating transcription factor) has slightly different modular composition of the transactivation region and it can be activated by JNK and p38 as well [78,79]. The molecular basis of ATF2 recognition by the two different kinases has not been characterized yet.

Besides transcription factors, MAP kinases often regulate cytoskeletal proteins by multisite phosphorylation. In most cases, phosphorylation regulates their association to microtubule or actin filaments. A microtubule binding protein, the X-linked lissencephaly DCX is an important player in embryonic brain development. The C-terminal IDR region is rich in phosphorylation sites that can be activated by JNK and hence modulate the DCX microtubule binding activity. Interestingly, the proposed JNK-interaction surface on DCX is in a globular doublecortin-domain, which suggested a new type of non-canonical interaction [80].

In the next chapters, the recent knowledge will be summarized about ATF2 and DCX protein substrates.

1.5 An AP-1 transcription factor – ATF2

Activating transcription factor 2 (ATF2) was first described in a yeast screen as a CRE sequence binding protein and is also known as cyclic AMP (cAMP) response element (CRE) binding protein 2 (CREB2) and CRE-BP1 [81]. It is ubiquitously expressed in most cell types and acts as an important mediator for a broad spectrum of stimuli by regulating the transcription of more than >300 genes

involved in cell growth, development and stress [82]. The function of ATF2 is multifaceted, and not limited to transcriptional regulation, as it is involved in chromatin remodeling, ATM mediated response to DNA damage and mitochondrial-based cell death [83]. It is not surprising that ATF2 has been functionally implicated in cancer and in the resistance to genotoxic stress-inducing agents, however, depending on the cancer type different studies described its oncogenic or tumor-suppressor role [82]. The complete somatic loss of ATF2 results in postnatal lethality and is associated with neurological, skeletal and respiratory defects in mouse suggesting a role in development as well [84,85].

ATF2 is a member of the activating protein-1 (AP1) transcription factor family, binding to specific DNA sequences depending on the hetero-dimerization partner (such as c-Jun, CREB, Fos or Maf AP-1 transcription factors) [86]. They all contain a C-terminal basic leucine zipper (bZIP) domain, which is responsible for the homo- or hetero-dimerization and DNA binding. The transactivation activity of ATF2 (and other AP-1 members) is regulated by a distinct N-terminal transactivation domain (TAD) consisting of regulatory phosphorylation sites (Figure 8A). It is well-known that the ATF2 phosphoswitch 69-TPTP-72 needs to be phosphorylated both on T69 and T71 to gain functionality, but the biochemical reason behind it remained surprisingly poorly understood [78]. T69 and T71 alanine mutant transgenic mouse exhibited similar lethality and phenotypes to the knockout model, confirming the crucial role of this phosphoswitch in ATF2 function [87].

Formerly, it was proposed that phosphorylation of 69-TPTP-72 inhibits the intramolecular interaction and autoinhibition between the TAD and bZIP domains. Activation of the phosphoswitch was described to be required for nuclear translocation and heterodimerization with other AP-1 factors to induce transcription. [88]. However, this phosphoswitch is able to control transcription in an artificial system as well, regardless of the DNA binding domain (e.g. if GAL4 DNA binding domain is fused to ATF2 TAD) [73]. Additionally, the carefully performed experiments of Liu et al (2006) ascertained that ATF2 translocation and heterodimerization with c-JUN are not affected by T69A/T71A or phosphomimetic mutants of the TAD domain. Moreover, they proved in multiple cell lines that the major driving force of the ATF2 nuclear localization is the physical interaction with c-Jun. Although ATF2 contains two nuclear localization signals (NLS), the overexpressed ATF2 mainly localized in the cytoplasm due to a nuclear export signal (NES) in the leucine zipper region. Dimerization with c-Jun sterically blocks this ATF2 NES signal, and prevents the nuclear export of the protein. Hence, the endogenous level ATF2 localization mainly depends on its relative expression level compared to c-Jun, which can be upregulated by extracellular stress through the MAPK pathway [89].

Phosphorylation of ATF2 TAD on the 69-TPTP-72 phosphoswitch by JNK and p38 occurs within minutes of the stress stimulus, rendering ATF2 an ‘early response’ protein [90]. First, Gupta et al

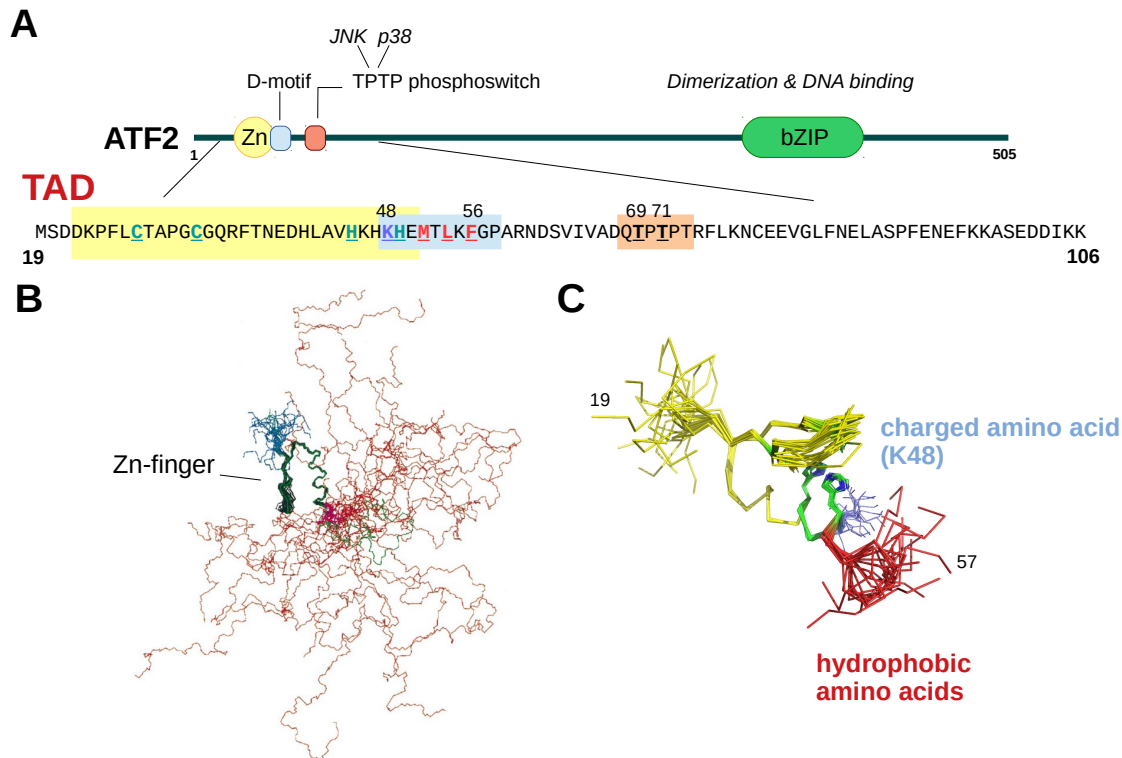


Figure 8 Architecture of the ATF2 transcription factor. A) The long, mainly unstructured ATF2 consists of two main domains, the transactivator TAD region and DNA-binding bZIP domain. The sequence of the TAD is shown with Zn-coordinating residues as green (C27, C32, H45 and H49), basic and hydrophobic residues of the D-motif blue and red, and the T69T71 phosphoswitch as bold. B) Ensemble of 20 model for ATF2 TAD calculated based on NMR data (adapted from Nagadoi et al. (1999)). C) Deposited NMR structure (PDB ID: 1BHI) shows, that the N- and C-terminal part of the Zn-finger is highly mobile. The basic lysine (blue) from an NFAT4-type docking sequence is part of the Zn-finger, whereas the hydrophobic amino acids (red) are disordered in solution.

(1995) described that JNK phosphorylates the T69 and T71 sites *in vitro* and *in vivo* upon UV irradiation or interleukin-1 treatment in COS and CHO cells. They also mapped the interaction region for JNK to be N-terminal from the phosphoswitch with GST-pulldown assay [78,79]. In this region a D-motif conferring to the classical NFAT4-type MAPK binding consensus can be found [91]

The structure of the unphosphorylated ATF2-TAD (19-106) was analyzed by NMR spectroscopy, and apart from a small C2H2-type zinc finger, it was found to be disordered (PDB ID: 1BHI) (Figure 8B). Although this single zinc-finger module is very similar to tandem zinc-fingers in TFIIIA type DNA-binding domains, it does not interact with DNA, as it lacks basic residues at important positions to bind the phosphate backbone. The C-terminal part (51-106) of the ATF2-TAD is

unstructured and highly dynamic, which was easily observable from the backbone ^1H - ^{15}N NOE experiments [92]. Although ATF2 TAD contains a NFAT4 type D-motif sequence, the basic part of the motif (K48) is not disordered, but embraced by the two zinc-coordinating histidines (H45 and H49) and embedded in the α -helix of the zinc-finger. The NMR ensemble on Figure 8C shows that the side chain of the K48 lysine (colored as blue) is oriented as part of the α -helix. On the other hand, M51 (corresponds to ϕ_L) side chain is relatively freely rotating, and the 52-56 backbone (with ϕ_A and ϕ_B) adapt many conformational states and is disordered in the 1BHI ensemble. If JNK interacts with this NFAT4-type motif of the ATF2, it is possible that other zinc-finger residues also contribute to this interaction, simply because of their proximity to each other.

A short peptide covering the D-motif region (46-KHKHEMTLKFG-56) of ATF2 was co-crystallized with JNK3 by Laughlin et al (2012). (PDB ID: 4H36). In this X-ray structure the peptide bound to the surface of JNK3 in a way that is incompatible with Zn^{2+} coordination. In addition, the thermodynamic parameters of the interaction and the binding affinity could not be determined by isothermal titration calorimetry (ITC), and this peptide only had very low inhibitory effect ($\text{IC}_{50} \sim 100 \mu\text{M}$) in JNK3 kinase activity assays [93].

In the first experiments of Gupta et al (1995), construct lacking the first 40 amino acids of ATF2 had decreased JNK binding in GST-pulldown assay, which suggests that the presence of intact Zn-finger contributes to the interaction [78]. Biochemical properties of C2H2-type zing-fingers were extensively studied by CD spectroscopy. The denatured form of the purified zinc-finger of TFIIIA was refolded by the addition of ZnCl_2 , while the EDTA (Ethylenediaminetetraacetic acid) treated or double mutant at zinc-coordinating cysteines had diminished alpha helical content compared to the folded form [94,95]. Therefore, the importance of the zinc-finger structure on the biological function can be easily observed using cysteine mutant constructs. Early experiments of Zu et al. (1991) showed that the C27S ATF2 mutant fused to c-Myb had inability to induce chloramphenicol acetyltransferase (CAT) expression from the appropriate reporter plasmid [96]. All these studies suggest that the C2H2 type zing-finger has a role in the activation of ATF2, maybe through the binding of the upstream activator, JNK.

Much less is known about how p38 recognizes the ATF2 TAD domain. Raingeaud et al. (1996) showed that ATF2 can be efficiently phosphorylated and regulated by the p38 MKK3/6 pathway *in vitro* and *in vivo* [79]. Many kinetic studies characterized the enzymatic activity of p38 on ATF2. Moreover, the GST-ATF2 (19-96) substrate is regularly used as p38 activity indicator in cell lysates

[97,98]. It cannot be ruled out, that p38 also interacts with the D-motif (and Zn-finger) of ATF2, as this site resembles to a MEF2A-type D-motif consensus, too.

1.6 A microtubule associated protein - DCX

Dynamic microtubule assembly and disassembly is an essential process in cell division, migration and differentiation. Microtubule-associated proteins (MAPs) mostly found in nerve cells are one of the regulators of this process by binding and stabilizing or destabilizing microtubules in a nucleotide-independent manner. Among the MAP kinases, the JNK family have a prominent role in the modulation of MAP-microtubule binding by phosphorylation, e.g. in the case of the intrinsically disordered MAP2 and Tau. As the majority of the MAP substrates do not have canonical D-motifs, the molecular details of their phospho-regulation is not fully understood [15,91,99]. Even so, the JNKs role in neuronal cell migration is unquestionable as double-knockout *JNK1^{-/-}JNK2^{-/-}* mice die early in embryogenesis, as they do not undergo neural tube closure [100]. Moreover, inhibition of JNK1/2 activity reduced the radial migration of neurons. Interestingly, a similar phenotype was described in rat embryos with *in utero* RNAi silenced DCX (Doublecortin, X-linked) MAP protein [101,102]. It has been demonstrated that DCX function can be regulated by the MKK7-JNK pathway [103].

The DCX protein expressed in neuronal precursor cells is essential for proper embryonic development of the layers of the cerebral cortex [104]. Inheritable mutations of *DCX* gene in the X chromosome cause abnormal migration of neurons during human brain development. In female carriers, this manifests as subcortical band heterotopia or “double cortex” syndrome, while in males as lissencephaly (smooth brain syndrome) together with severe cognitive disabilities and epilepsy in surviving patients [105]. The DCX protein consists of two similar, but not identical microtubule binding doublecortin (DC) domains - the N-DC (the N-terminal DC domain) and C-DC (the C-terminal DC domain) – flanked by N- and C-terminal IDP regions (Figure 9A). Interestingly only the C-DC domain is able to bind to dimeric tubulin and mediate microtubule nucleation, whereas the N-DC domain acts as a stabilizer for the microtubule lattice. The tandem and flexible linked N-DC+C-DC domains collaborate together to enhance tubulin polymerization, stabilize the 13 protofilament microtubules and bundle them as a crosslinking agent [106]. Cryo-EM structure of DCX bound microtubule (Figure 9B) confirms that hereditary pathogenic mutations are localized within the DC domains core or in the DC-tubulin interface and thus they negatively affect microtubule binding activity [107,108]. Numerous studies of the regulation of the DCX-MT interaction have been undertaken to improve understanding of the functions of DCX. The microtubule stabilization activity

can be modified on multiple phosphorylation sites in the long S/P-rich unstructured C-terminus and the N-terminus as well. The activity of those sites are balanced by different kinases and phosphatases (see (Figure 9A).

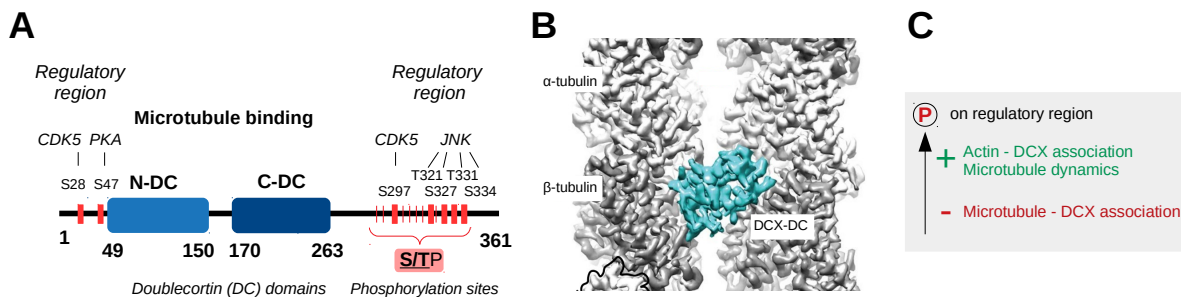


Figure 9 DCX, as a microtubule-associated protein. A) Schematic architecture of the human DCX with the main regulatory phosphorylation sites. The most characterized phosphorylation sites are labeled with thicker box and regulatory kinases are indicated. B) Cryo-EM map of the microtubule co-polymerized with DCX at 3.8 Å resolution (EMD-3964). One of the DC domain (cyan) is sitting between four tubulin units of the 13-protofilament microtubule (modified after Manka & Moores, 2018) C) Most of the known phosphorylation sites in the regulatory regions contribute to weaker binding to the microtubule, cause increased association to actin filaments, and enhancement in microtubule dynamics.

Gdalyahu et al. (2004) found that endogenous JNK in primary hippocampal neurons is responsible for maintaining the phosphorylation level of T321, T331 and S334 sites on the C-terminal IDP region, as in the presence of JNK specific inhibitor (SP600125) their phosphorylation was attenuated. Alanine mutants of these residues (T321A, T331A and S334A) negatively affected neurite outgrowth of nerve growth factor-stimulated PC12 cells, while their phosphomimicking mutants enhanced it [103]. The JNK dependent S328 also affected motility of primary cerebellar neurons suggesting the critical role of JNK-mediated DCX phosphorylation in neuronal migration [109]. Deletion of the DCX C-terminal region containing all the C-terminal phosphorylation sites leads to increased MT association, with diminished tubulin exchange rate resulting in a less dynamic behaviour of the microtubule [110]. In agreement with this, multiple studies focusing on different phosphorylation sites indicate that upon phosphorylation DCX has decreased association with microtubule, but at the same time associates with actin filaments possibly via spinophilin (or neurabin II) [111–114]. Altogether we can conclude, that phosphorylation of DCX affects microtubule dynamics and orchestrates the microtubule-actin interplay in the growth cone. The combinatorial phosphorylation of DCX by different kinases at multiple sites may be a regulatory switch in the transition of a migrating neuron through multiple phases of migration.

Currently, it is unknown how protein kinases interact with DCX and specifically phosphorylate sites in its N- or C-terminal region controlling the protein's binding to MTs. Gdalyahu et al. (2004) reported physical interaction between JNK and DCX by mapping the interaction region to N-DC and/or C-DC domains when using purified GST-tagged DCX constructs as bait and P7 mouse brain extracts as prey. This indicates that DCX might interact with JNK in a non-canonical way. With the lack of detailed *in vitro* binding studies, it would be gap filling to unravel the molecular interface between DCX and JNK, as it might provide us a new type of MAPK interaction. A more detailed description of the molecular mechanism underlying DCX phosphorylation by JNK could contribute to a better understanding of the role of JNK in neuronal migration.

2. Aims

My aim was to characterize MAPK-substrate interactions that utilize interaction surfaces on MAPKs in a different way from classical DRS+D-motif or FRS+F-motif type interactions. We selected two MAPK substrates, the Activating Transcription Factor 2 (ATF2) and the DCX microtubule binding protein for biochemical and structural studies in order to understand their likely non-canonical binding to MAPKs. My main questions were the following:

- ◆ ATF2 is known to mediate a transcriptional response from both the JNK and p38 pathways [90]. How can the ATF2 phosphoswitch be efficiently regulated by the two MAPKs? What is the structural basis of the molecular recognition?

To answer these questions, we first aimed to biochemically characterize the interaction between JNK, p38 and ATF2, and to obtain the high resolution structural models of their complexes. To further examine the MAPK based ATF2-TAD regulation, we aimed to quantitatively describe the phosphoswitch activation level depending on the strength of upstream signals from JNK and from p38 pathways.

- ◆ JNK kinase plays a role in neuronal migration by phosphorylating DCX [80]. How does JNK specifically recognize the DCX protein?

To answer this question, we wanted to locate and characterize the interface between the two proteins with biochemical and structural methods. We also aimed to validate our findings in cell-based assays.

3. Material and Methods

3.1 Protein expression and purification

All proteins were from human. Full-length ATF2 (1-505; Uniprot: P15336-1) was amplified from HEK293T cDNA and full-length DCX (1-366; Uniprot ID: A8K340) containing plasmid was a kind gift from Marie Bogoyevitch. All constructs were produced using standard molecular cloning protocols that are not detailed in the thesis (see primer list in Appendix Table 3). Mutant constructs were generated by two-step PCR mutagenesis. Various fragments of the ATF2-TAD and full length or shorter fragments of DCX were cloned into a modified pET-15 vector (Novagen) including N-terminal GST (glutathione S-transferase) or MBP (maltose binding protein) tag followed by a tobacco etch virus (TEV) cleavage site and a C-terminal hexa-histidine tag. For structural studies ATF2-TAD fragments were inserted into a modified pBH4 vector and proteins were expressed with an N-terminal hexa-histidine tag that was cleaved off by the TEV protease. These protein constructs had a tyrosine inserted at the ATF2 N-terminus to enable protein concentration determination by absorbance at 280 nm. Expression plasmids were transformed into *E. coli* BL21(DE3) cells and grown in LB (Luria Broth) until $OD_{600}=0.5$, protein expression was induced with 200 μ M isopropyl β -d-1-thiogalactopyranoside (IPTG) overnight at 18 °C. In the case of ATF2 expressions, the LB was supplemented with 200 μ M Zn-acetate for ATF2. The cell pellets were lysed and the recombinant protein was purified with standard protocol using Ni-NTA (Ni²⁺ loaded nitrilotriacetic acid) agarose beads (Macherey-Nagel). MBP-ATF2/DCX-His6 constructs that were expressed similarly as above and purified on maltose resin after Ni-NTA purification. Protein samples were concentrated to >10 mg/ml and stored in MBP elution buffer (20 mM Tris pH 8, 150 mM NaCl, 10% glycerol, 2 mM TCEP (tris(2-carboxyethyl)phosphine), 0.1% BOG (octyl-beta-glucoside), 2 mM BA (benzamidine), 30 mM maltose) for fluorescence polarization (FP) based measurements, kinase assays or analytical gel filtration. For ITC measurements the MBP tag was removed from MBP-ATF2(19-58)-HIS6 by TEV protease and the protein was further purified on a Resource S column (GE Healthcare) in buffer containing 20 mM MES (pH 6.3), 25 mM NaCl, 10 % glycerol and 2 mM β ME and eluted with NaCl gradient.

For crystallography His6-ATF2-(19-58)-WT or the Q34R/H47R mutant was captured on Ni-NTA agarose beads, the hexa-histidine tag was cleaved off by TEV protease, the protein was further

purified on a Resource S column (pH 6.3) and gel-filtrated into storage buffer (20 mM Tris, pH 8, 150 mM NaCl, 2 mM TCEP) using a Superdex75 10/30 size-exclusion column (GE Healthcare).

For NMR studies His6-ATF2-(19-78) or -(19-106) was transformed into BL21(DE3) and the culture (2 L) was grown in LB at 37 °C until $OD_{600}=0.6-0.8$, then the cells were pelleted and transferred to 0.5 L M9 media containing 1 g $^{15}NH_4Cl$, 200 μM Zn-acetate, 1x vitamin mix (Sigma, #B6891), 1x MOPS micronutrient mix and 2 g glucose, then induced with 1 mM IPTG at 37 °C for 4 hours. Labeled protein was captured on Ni-NTA resin; after cleaving the hexa-histidine tag by TEV, ^{15}N -ATF2 was purified on Resource S (19-78, pH 6.3) or Q column (19-106, pH 9) and gel-filtrated into storage buffer (20 mM Tris pH 8, 150 mM NaCl, 2 mM TCEP). For SAXS sample preparation the GST tag was removed by TEV protease from GST-DCX-His6 constructs and DCX-His6 was further purified on a Resource S column in buffer containing 20 mM HEPES (pH 7), 25 mM NaCl, 10 % glycerol and 2 mM β ME and eluted with NaCl gradient. The fractions with >95% purity were collected and concentrated to >10 mg/ml.

JNK1-dC20 (where the C-terminal 20 residues are truncated), p38 α and ERK2 were expressed in *E. coli* and purified using standard procedures including at least two purification steps. For structural studies the hexa-histidine capture step, TEV cleavage and subsequent anion exchange were followed by gel filtration. Phosphorylated MAPKs were produced by co-expressing them with constitutively active GST-tagged MAP2Ks [5]. Preparation of double-phosphorylated p38 for X-ray crystallography and for HSQC experiment (titration of ^{15}N -ATF2) was carried out by Péter Sok. The homogeneity of phosphorylation was verified by intact mass spectrometry and the activity was analyzed in kinase assay.

The purity of all the protein samples were monitored in SDS-PAGE stained with Coomassie. Aliquots of proteins were flash-frozen in liquid nitrogen in the presence of 10% glycerol and stored at -80 °C. For experiments involving ATF2, none of the purification, storage and assay buffers contained EDTA nor DTT, so that to maintain the structural integrity of the ATF2 zinc-finger domain, but samples contained 2 mM TCEP.

Synthesis and purification of peptides were carried out by Ádám L. Póti. SPFENEF peptide (ATF2: 83-102), its S90N or phospho-S90 versions and pepDCX25 peptide (DCX: 342-366) or its del348V version were chemically synthesized on an automated PSE Peptide Synthesizer (Protein Technologies, Tucson) with Fmoc strategy. The peptides were purified on reversed-phase HPLC and the appropriate fractions analyzed by mass spectrometry were lyophilized.

3.2 Protein-protein binding assays

GST/MBP pull-down experiments with GST-ATF2 and MBP-DCX constructs and GST or MBP control as baits and JNK1 as prey were performed as described earlier [5]. Briefly, the GST or MBP fusion proteins were immobilized on glutathion-sepharose or maltose resin in 20 mM Tris (pH 8.0), 100 mM NaCl, 0.1% IGEPAL, and 2 mM TCEP buffer. The loading of the resin by different bait proteins was checked by SDS-PAGE. The resins with equal amount of baits (typically 20 µg) were incubated with 100 µg of JNK1 for 30 min in the same buffer, washed 3 times and analyzed on SDS-PAGE. The buffer contained 2 mM EDTA during the entire process, where indicated. Preliminary experiment for mapping the ATF2 binding region to JNK was performed by András Zeke.

Fluorescence polarization (FP) based protein-protein binding experiments were carried out using 50 nM carboxyfluorescein(CF)-labeled CF-evJIP (CF-PPRRPKRPTSLDLPSTPSL) for JNK1 and CF-RHDF1 (CF-SLQRKKPPWLKLDIPS) for p38 α and ERK2. FP measurements were performed in 20 mM Tris (pH 8.0), 100 mM NaCl, 0.05% Brij35P, and 2 mM TCEP and measured using a Cytation™ 3 (BioTek Instruments) plate reader in 384-well black plates and the curves obtained through anisotropy detection were fitted with OriginPro8 as described before [5]. Proteins were pretreated with 2 mM EDTA for 30 min, where indicated.

Isothermal titration calorimetry (ITC) measurements were performed on MicroCal iTC200 (GE Healthcare) at 20 °C with 20 injection of 1.5 µl from ATF2(19-58) at every 180 s with a stirring speed of 750 rpm. Before the experiments JNK and ATF2 protein samples were dialyzed in the same buffer overnight (50 mM HEPES, pH 8.0, 150 mM NaCl, 10% glycerol, 0.5 mM TCEP) in the absence or presence of 2mM EDTA and subsequently concentrated. JNK concentration in the measuring cell was 100 µM.

For analytical gel filtration, purified MBP-DCX-His6 constructs (150 µM), JNK1 (150 µM) and their mixture (150 +150 µM, 1:1 stoichiometric ratio) were loaded into a Superdex200 10/30 size-exclusion column (GE Healthcare) in 20 mM Tris pH 8, 150 mM NaCl and 2 mM TCEP. Fractions were analyzed by running on SDS-PAGE.

3.3 Kinase assays

MBP-ATF2-His6 protein constructs were double affinity purified and used as MAPK substrates in various kinase assays. For the ATF2 substrate with a MEF2A docking motif, the ATF2 Zn-finger+docking motif region was replaced by the MEF2A peptide sequences (SRKPDLRVVIPPSS), which were followed by the ATF2-59-100 region.

For solid-phase phosphorylation assay, substrates (1 μ l from 1 mg/ml in MBP elution buffer) were dotted as triplicates on nitrocellulose membrane, then the membrane was dried for at least 1 hour. The membrane blocked with 3% BSA (bovin serum albumin) in TBS-T (20 mM Tris pH=7.4, 150 mM NaCl, 0.1% Tween-20). The kinase reaction performed by vigorous shaking of the membrane with picomolar concentration of active MAPK-s in kinase buffer (50 mM HEPES, pH 7.4 100 mM NaCl, 5% glycerol, 0.05% IGEPAL, 2mM TCEP, 2 mM $MgCl_2$, 1 mM ATP) for 5 min at room temperature (RT) with minor modification as described by Zeke et al. (2015) [30]. The reaction was stopped by the addition of 20 mM EDTA, and the membrane was subsequently immunoblotted.

Enzyme kinetics measurements on ATF2 phosphorylation were performed in solution, mixing 5 nM enzyme with MBP-ATF2(19-100) substrate at various concentration (100, 50, 25, 10, 5, 2.5, 1 and 0.5 μ M) in kinase buffer and the reaction was started by adding 5 mM ATP at RT. Reactions were stopped by adding kinase buffer containing 50 mM EDTA instead of $MgCl_2$ and the reaction mixture was diluted to 0.05 μ M MBP-ATF2 in the same buffer. 1 μ l of the diluted reaction mixture was spotted as triplicates and dried on a nitrocellulose membrane in the presence of a calibration series. Calibration series were made from fully phosphorylated MBP-ATF2 mixed with dephosphorylated MBP-ATF2 (0.05 μ M in total) to confirm the linear range of the detection, and the rate of product formation was calculated. The low epitope density at 0.05 μ M was optimized to have linear concentration-signal function for quantitative results.

For K_i measurements of synthetic SPFENEFF peptides, competitive kinetic assay were performed using 2 nM pp-p38, 2 μ M MBP-ATF2 substrates and 3-fold dilution series of peptides starting from 1 mM. The maximal velocity was determined from a reaction containing no peptide, and IC_{50} values were obtained by using the logistic dose-response equation in QtiPlot 0.9.8.9. K_i was calculated as $K_i = IC_{50} / (1+S/K_M)$ where the K_M (17.3 μ M) was previously determined for pp-p38 – MBP-ATF2(19-100)-WT.

For immunoblot, membranes were blocked with 3% BSA (Bovine serum albumin) in TBS-T for 1h, RT and incubated overnight at 4°C with primary antibody anti-phospho-T71 ATF2 antibody (Cell Signaling Technology, #9221) at 1:3,000 dilution or anti-phospho-T69/T71 ATF2 (Merck, #05-891) at 1:5000 dilution or anti-HIS (Sigma, #H1029) at 1:10000 dilution in the same blocking buffer. After washing the membranes 3 times with TBS-T, infrared dye conjugated secondary antibodies were applied: secondary anti-rabbit antibody (IRDye® 800CW Goat anti-Rabbit IgG, #926-32211), secondary anti-mouse antibody (IRDye® 800CW Goat anti-Mouse IgG, #926-32210) or secondary

anti-mouse antibody (IRDye® 680RD Goat anti-Mouse IgG, #926-68070), at 1:1,0000 dilution in blocking buffer. Membranes were developed after washing 3x with TBS-T with LI-COR Odyssey® Clx infrared imaging system.

Reactions with different concentrations of MBP-ATF2(19-100)-TATA and 5 nM pp-JNK were carried out by Anita Alexa in the presence of [γ - 32 P]ATP at the same conditions as above. Samples were run on SDS-PAGE in the presence of calibration series of fully phosphorylated ATF2-TATA on S90, then the gels were dried and analysed by phosphorimaging on a Typhoon Trio+ scanner (GE Healthcare).

3.4 NMR spectroscopy

For the JNK-ATF2 complex the ^1H - ^{15}N heteronuclear single-quantum coherence (HSQC) spectra were obtained from 50 μM uniformly ^{15}N -labeled ATF2-(19-78) in the absence or presence of JNK1 at molar ratios of 0.5:1 and 1:1 ([JNK1]:[ATF2]). Experiments were carried out in 20 mM potassium phosphate (pH 6.3), 200 mM NaCl, 2 mM TCEP containing 5% d-Glycerol and 10% (v/v) D_2O at 25 °C. Briefly, concentrated ^{15}N -ATF2 and JNK1 were dialyzed overnight against the same phosphate buffer, mixed with the appropriate ratios and supplemented with 5% d-Glycerol and 10% (v/v) D_2O . HSQC spectra were recorded on AVANCE II Bruker spectrometer (800MHz) equipped with a TCI-active HCN cooled z-gradient cryoprobe. For data analysis, published ^1H , ^{15}N resonance assignment of ATF2-(19-106) were used [92]. Spectra were processed using NMRPipe and analyzed using NMRFAM-SPARKY [115,116]. Peak heights were used to calculate intensity ratios of ATF2 in the presence versus in the absence of JNK1 and combined (^1HN , ^{15}N) chemical shift perturbations (CSP), were calculated using the equation of $\Delta\delta_{^1\text{HN},^{15}\text{N}} = \sqrt{[(\Delta\delta_{\text{HN}})^2 + (w1*\Delta\delta_{\text{N}})^2]}$, where $w1$ (=0.154) is a weight factor determined using the BioMagResBank chemical shift database [117]. Data recording and processing were carried out by Ashish Sethi (University of Melbourne).

p38 and ATF2 TAD binding experiments were carried out on a four-channel 600-MHz Varian NMR System™ spectrometer equipped with a 5-mm indirect detection triple resonance ($^1\text{H}^{13}\text{C}^{15}\text{N}$) z-axis gradient probe. ^1H - ^{15}N HSQC spectra were performed on 100 μM uniformly ^{15}N -labeled ATF2-(19-106) in the absence and presence of pp-p38 and np-p38 at molar ratios of 0.5:1 and 1:1 ([pp-p38]:[ATF2]) and 2:1 ([np-p38]:[ATF2]). Samples were measured in 20 mM potassium phosphate (pH 6.3), 200 mM NaCl, 2 mM TCEP containing 10% (v/v) D_2O at 27°C. Spectral processing and data analysis were carried out using Felix 2004 (Accelrys, Inc.) and CCPNMR with previously published ^1H , ^{15}N resonance assignment of ATF2-(19-106) [92]. Quantification of peak intensities and CSPs were

performed similarly as in the case of ATF2(19-78)-JNK experiment. Data recording and analysis were carried out by Orsolya Tóke.

Production of uniformly [^2H , ^{15}N]-labeled np-p38 and pp-p38 for NMR measurements was done similarly as described before [118]. The interaction between nonphosphorylated or phosphorylated p38 and the S/NPFENEf motif was studied by mixing the chemically synthesized ATF2(83-102) peptides with 0.1 mM [^2H , ^{15}N]-labeled np-/pp-p38 in 10 mM HEPES pH 7.4, 0.15 M NaCl, 5 mM DTT and 10% D₂O. The 2D [^1H , ^{15}N] TROSY spectra of free and peptide added samples were acquired on a Bruker Avance NEO 600 MHz NMR spectrometer equipped with a TCI-active HCN cooled z-gradient cryoprobe at 35 °C. The spectra were processed using Topspin 4.0.6 and analyzed with NMRfAM-SPARKY (Appendix Figure 2C). Protein expression, sample preparation, data recording and analysis were carried out by Ganeshan Senthil Kumar (University of Arizona).

Structural analysis of SPFENEf peptides (ATF2 83-102) by NMR was carried out by Orsolya Tóke. Experiments were recorded on a four-channel 600-MHz Varian NMR System™ spectrometer equipped with a 5-mm indirect detection triple resonance ($^1\text{H}^{13}\text{C}^{15}\text{N}$) z-axis gradient probe. Resonance assignment of the peptides was obtained using the combination of 2D TOCSY, 2D NOESY and natural abundance ^1H - ^{13}C HSQC experiments in 20 mM potassium phosphate (pH 6.3), 200 mM NaCl supplemented with 10% (v/v) D₂O at 27°C. ^1H chemical shifts were referenced to external 4,4-dimethyl-4-silapentane-1-sulfonate (DSS) and the ^{13}C chemical shifts were referenced indirectly to DSS. Secondary structure propensities (SSP) of the peptides were calculated on the basis of H_α , C_α and C_β chemical shifts using the SSP program [119]. The SSP score of a residue can be interpreted as the expected fraction of α -helical or β -strand/extended structure and dihedral angles derived from SSP scores were used as restraints in structure calculations with ARIA (Ambiguous Restraints for Iterative Assignment, version 2.2). The computational method in the structure calculation employed torsional angle simulated annealing followed by torsional angle and then Cartesian molecular dynamics cooling stages. Structural refinement was completed in a water shell resulting 10 structure for each peptide.

3.5 HADDOCK modeling

We used HADDOCK approach to create models of JNK-ATF2 and p38-ATF2 complexes with ambiguous and unambiguous distance restraints derived from experimental data to drive the docking of ATF2 to MAPKs [120].

For the JNK-ATF2 complex, the input model ensemble for ATF2 was created manually by using the ATF2 Zn-finger structure (PDB ID: 1BHI) and three different JNK-D-motif structures representing the hydrophobic region (φ_L , φ_A , and φ_B) (PDB ID: 2XS0, JNK1-pepNFAT4; 4H36, JNK3-pepATF2; 4UX9, JNK1-pepMKK7). After superimposition at Met51 C α , the two fragment – zing-finger and D-motif) were joined in Coot[121]. For docking input, we retained only 25 models that did not lead to extensive clashes with the surface of JNK1 (using the hydrophobic region as a pivot point). The conformational variability of the ensemble can be described with $RMSD_{max}(CA)=10.54 \text{ \AA}$ (Figure 10A). The input model for JNK derived JNK1-pepNFAT4 crystal structure (PDB ID: 2XS0) after deleting the NFAT4 peptide. Docking was performed in the Haddock2.2 webserver (expert interface). Unambiguous restraints for the hydrophobic motif were defined from evolutionarily conserved distances of 15 MAPK:D-motif crystal structures (unambiguous = always included in the calculation) (Figure 10B). To maintain the structural integrity of the C2H2 type zing finger during the docking procedure, unambiguous restraints were defined for the Zn²⁺ tetrahedron: 4 distances restraints between the Zn²⁺ atom and the coordinating atoms and 6 distance restraints pairwise between the four

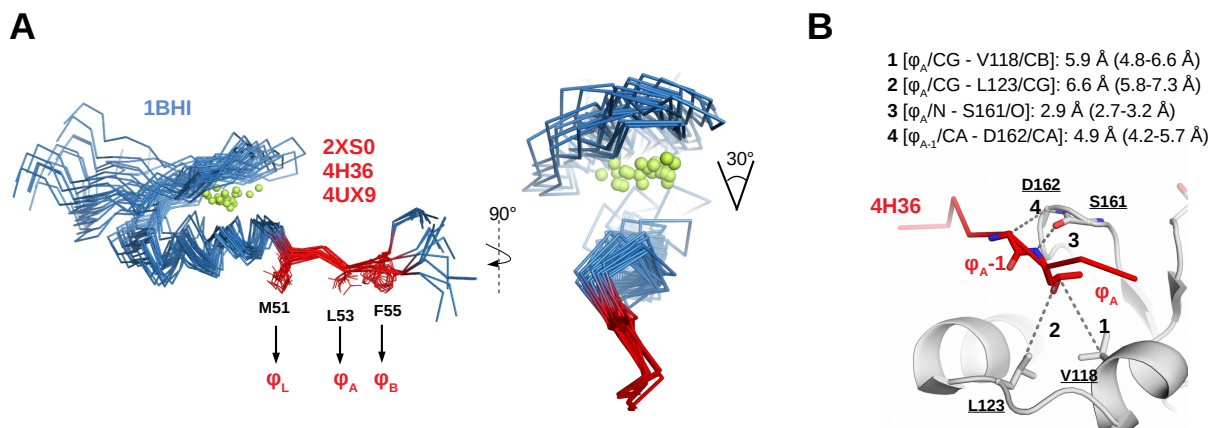


Figure 10 Input structure and restraints for HADDOCK modeling (A) The ensemble of ATF2(19-58) used for HADDOCK input were built from PDB ID: 1BHI and D-motif region of JNK+D-motif complexes. Zn²⁺ is shown as a green sphere. The relative orientation of Zn-finger from the axis set by the hydrophobic part of the D-motif is varied by $\sim 30^\circ$ between the different models. (B) Evolutionarily conserved unambiguous restraints were used to drive the docking algorithm is shown in the JNK-pepNFAT4 crystal structure (**PDB ID: 2XS0**).

coordinating atoms [122]. In the case of histidines in the tetrahedron (H45 and H49), the protonation state was defined as HISD for each. Other parameters in the Haddock2.2 webserver were default. The docking protocol consists of three stages and uses CNS (Crystallography and NMR system) as its

structure calculation engine [123]. The first step was the rigid-body energy minimization where 1,000 structures were generated. From rigid-body docking the lowest energy 200 structures were subjected to semi-flexible simulated annealing in torsion angle space followed by refinement in explicit water. After each stages the structures were ranked based on HADDOCK score, which is a weighted sum of van der Waals, electrostatic, desolvation and restraint violation energies together with buried surface area. After water refinement, the structures were clustered with the Fraction of Common Contacts method. The best structure from the lowest energy cluster were analyzed later.

The model of pp-p38+ATF2-WT(TAD) Michaelis-Menten complex generated with step-by-step docking of D-site, phosphotarget site and F-site. The pp-p38 and ATF2 SPFENEF (83-102) structure was extracted from the crystal structure of the pp-p38-ATF2(S90N) complex, and N90 were mutated to serine in Coot [121]. The wild-type version ATF2 Zn-finger+D-motif was taken from the JNK-ATF2(19-58) crystal structure and the substrate motif (67-DQTPTP-72) was generated from the DYRK1A-substrate peptide complex (PDB ID: 2WO6) by mutagenesis, where T69 was chosen to be the phosphoacceptor site [124]. First, Zn-finger+D-motif were docked to pp-38 driven by unambiguous distance restraints, similarly as described for the JNK-ATF2 complex (see Figure 10). For the docking of the substrate motif (DQTPTP) to pp-p38 at the active site, unambiguous distance restraints were derived from the DYRK1A-peptide complex (2WO6). SPFENEF docking was driven by intermolecular (ambiguous) restraints based on perturbations on the pp-p38 2D [¹H,¹⁵N] TROSY spectra after titration with SPFENEF peptide (at 1:4 protein:peptide ratio). Residues with > 50% intensity decrease and with > 10% solvent accessibility (RSA) calculated by NACCESS were defined as active [125]. Passive residues were chosen as contiguous to active residues and solvent exposed (RSA values of 10% or above). Active residues were limited to the MAPK FRS (or also called DEF pocket), since the pp-p38-ATF2(S90N) crystal structure indicated this MAPK region to be the major contact surface, moreover, mutagenesis of the FRS region had been shown to negatively affect p38-mediated ATF2 phosphorylation [126,127]. In the SPFENEF peptide F92 and F96 were selected to be active residues (based on mutational experiments), and its neighbors as passive residues. The docking parameters in the HADDOCK 2.2 webserver was the same as in the case of ATF2-JNK. The three ATF2 peptides were connected together with the appropriate linkers in MODELLER [128].

3.6 Protein crystallization and X-ray structure solution

Gel filtrated JNK1-dC20 and ATF2-Q34R/H47R(19-58) were mixed at 1:1.5 ratio (240 μM JNK1 + 360 μM ATF2) in the presence of 5 mM TCEP and 1 mM Adenosine-5'-[(β,γ)-imido]triphosphate

(AMP-PNP). Initial hits were found with the cooperation of iNEXT facilities in Morpheus screen (Molecular Dimensions) A9 condition (10% w/v PEG 20 000, 20% v/v PEG MME 550, 0.03 M MgCl₂, 0.03 M CaCl₂, 0.1 M bicine/Trizma base (pH=8.5)) in sitting drop plate with the same reservoir buffer in 4°C. To improve resolution we further optimized the crystallization conditions to gain larger crystal in-house by varying pH, PEG concentration and reservoir solution. Final crystal grew in 8% w/v PEG 20 000, 18% v/v PEG MME 550, 0.025 M MgCl₂, 0.025 M CaCl₂, 0.08 M bicine/Trizma base (pH=8.8) in hanging drops at 4°C and the reservoir solution was 1.25 M NaCl. Crystals were flash frozen in liquid nitrogen after adding 2 µl crystallization solution with increased PEG concentration (11% w/v PEG 20 000 and 22% v/v PEG MME 550) to the drop. The JNK1 search model for molecular replacement is derived from the JNK1-NFAT4 protein-peptide structure (PDB ID: 2XS0), while the ATF2 search model was from the solution structure of the zinc-finger domain (PDB ID: 1BHI, model 1). The MR solution contains two JNK-ATF2 complexes and the structure was refined at 2.7 Å resolution. The ATF2 C-terminal docking motif region, the ATF2 N-terminal amino acids, the JNK activation loop (chain B) and AMP-PNP were manually built in Coot.

For the p38-ATF2 complex, gel filtrated pp-p38 and pepATF2_S90N(83-102) were mixed together at 1:5 ratio (250 µM pp-p38 + 1250 µM peptide) and supplemented with 5 mM TCEP and an ATP competitive inhibitor (375 µM, Skepinone-L). Crystals were found in in-house grid screen comprised of various molecular weight PEGs in two concentration and in different pH-s. Crystals were grown after 1 day in 12-16% PEG3350, 0.1 M cacodylate pH 6.5 in hanging drops at room temperature, but growing in 4°C produced less nucleation, but bigger and single crystals after 3-4 days. Final crystals grew in 14% PEG3350, 0.1 M cacodylate pH 6.5 in hanging drops at 4°C and the reservoir solution was 1.375 M NaCl. Crystals were flash frozen in liquid nitrogen in the same crystallization solution supplemented with 30% glycerol. The search model for molecular replacement was double-phosphorylated p38 from the crystal structure of the pp-p38-MK2 complex (PDB ID: 6TCA). The refined crystallographic model contains one pp-p38+ATF2(83-102)+Skepinone-L complex where ATF2 residues 88-101 could be traced in the electron density map (1.95 Å resolution).

For the JNK-DCX complex gel filtrated JNK1-dC20 and pepDCX were mixed at 1:1.5 ratio (280 µM JNK1 + 420 µM pepDCX) in the presence of 10 mM TCEP, 1 mM AMP-PNP and 5 mM MgCl₂. Crystals grew in 7.5-9% PEG 20000 in 0.1 M Tris pH 8.5 in hanging drops at RT and the reservoir solution was 1-1.25 M NaCl. Crystals were flash cooled in liquid nitrogen after adding 2 µl crystallization solution supplemented with 40% glycerol to the drop. For molecular replacement, the

JNK1 search model contained the full polypeptide chain of the MAPK from the JNK1-NFAT4 protein-peptide structure (PDB ID: 2XS0). The MR solution contains three JNK-pepDCX complexes and the structure was refined at 3.5 Å resolution. The DCX docking motif, the JNK activation loop and AMP-PNP were manually built in Coot.

All of the crystals data were collected at PETRA III P13 or P14 beamlines, Hamburg (Germany) and data collection were carried out by Isabel Bento. All data were processed with XDS and the phase problem was solved by molecular replacement using PHASER [129,130]. Structure refinement was done using PHENIX, for JNK-ATF2 and JNK-DCX with NCS restraints for corresponding polypeptides. Cycles of manual refinement/building were carried out in Coot [121,131]. Details of the data collection and refinement statistics are found in Appendix Table 1.

3.7 Protein sample preparation for SAXS and modeling

Purified DCX constructs and JNK1-dC20 were mixed in a 1:1.5 stoichiometric ratio and gel-filtrated on a Superdex 200 Hiloal 16/600 (GE Healthcare) column in 20 mM Tris pH 8.0, 150 mM NaCl and 1 mM DTT. Fractions with 1:1 molar ratio were pooled together and supplemented with 10% glycerol and 2 mM TCEP. Samples were concentrated to 6-10 mg/ml and dialysed in 20 mM Tris pH=8, 150 mM NaCl, 2 mM TCEP, 10% glycerol using small volume dialysis buttons. In order to preclude buffer scattering subtraction problems, the equilibrated dialysis buffers were used for the blank and for the preparation of dilution series for the SAXS measurement.

SAXS measurements were performed at the P12 beamline at EMBL-HAMBURG (PETRA). Data were analyzed using ATSAS program package [132]. To minimize inter-particle effect on the scattering curve, a dilution series on concentrated stoichiometric complexes from ~10 to ~0.3 mg/ml were measured. Only minor concentration effect was observed during measurement that was excluded by manual merging. The radius of gyration (Rg), maximum particle dimension (Dmax) and molecular mass were estimated for each sample the data using PRIMUS [133] and GNOM package [134]. *Ab initio* shape determination was performed with DAMMIN [135], DAMCLUST [136] and the DAMAVER suite [137]. Rigid body modeling was done by CORAL to fit the scattering curve[136]. During the CORAL run, the N-DC and C-DC domains and NFAT4 type D-motif were treated as rigid bodies, taken from crystal structures PDB ID: 2BQQ (DC domains) and 2XRW (NFAT4). The unstructured linker regions were modeled by the software. In the case of JNK-DCX complexes, the position of D-motif and JNK were fixed as a docked complex (from 2XRW), but the DC domains were allowed to move free during the CORAL run. 10 models were generated for each sample. Center of

mass distances (COM) were calculated between N-DC – docking motif and C-DC - docking motif in the case of DCX-s only, and in complex with JNK. The final structures were fit to the experimental data using CRY SOL [138]

3.8 Cell culture

HEK293T cells were maintained by subculturing two times per week in Dulbecco's modified Eagle's medium (DMEM, Gibco) containing 10% fetal bovine serum (FBS) and 50 µg/ml gentamicin at 37°C in an atmosphere of 5% CO₂. For preparing the HT-M Tet-on (HT) stable cell lines, HEK293T cells were transfected Lipofectamine 3000 reagent (Invitrogen) in Opti-MEM (Gibco) with pEBDTet vectors containing a MAP2K-MAP3K kinase domain fusion (MKK7-MLK3) or constitutively activated versions of full-length MAP2K (MKK6EE) that turn on JNK and p38, respectively [139]. To achieve double activation of JNK and p38, HT-MKK7-MLK3 vector with puromycin resistance cassette and HT-MKK6EE with hygromycin resistance were co-transfected. After transfection, the cells were selected with 5 µg/ml puromycin or 100 µg/ml hygromycin or both for at least one week. The expression of the FLAG-tagged transgene and concomitant specific MAPK activation were verified by Western-blot after doxycycline (DOX) treatment (2 µg/mL) in DMEM without FBS.

For analyzing the activation of full-length ATF2 constructs by endogenous JNK, HT-MLK3-MKK7 cells were seeded in 24-well plate and were transfected the next day with 250 ng F1 (YFP fragment) tagged ATF2 (1-505) constructs with Lipofectamine 3000 in Optimem. The medium was changed to DMEM after 4 hours of transfection and cells were induced for 0, 8 or 24 hours with 2 µg/ml doxycycline (DOX). Cells were washed gently in PBS, harvested in SDS loading buffer, subjected to SDS-PAGE and blotted to nitrocellulose or PVDF membrane. The membranes were blocked by Odyssey Blocking Buffer (TBS) (LI-COR) for 1h, RT and incubated overnight at 4 °C with primary antibodies diluted in the blocking buffer: Anti-phospho-ATF2-T69/T71 (Merck, #05-891, 1:2000 (endogenous) or 1:10000 (transfected)) and anti-phospho-p38 (Cell Signaling, #9215, 1:3000) in nitrocellulose membrane, while anti-phospho-JNK (Cell Signaling, #9251, 1:2000), anti-FLAG (Sigma, #F1804, 1:10000) and anti-tubulin (Sigma, #T6199, 1:10000) on PVDF membrane. Membranes were developed after washing the membranes with TBS-T and incubating for 1h, RT with appropriate IRDye® secondary antibodies at 1:10000 dilution in blocking buffer.

3.9 Cell-based protein-protein interaction assays

Enhanced Yellow Fluorescence Protein (eYFP) based BiFC assay was implemented to monitor interaction and localization of the JNK-ATF2 complex in HEK293T cells as described before [30]. ATF2(1-505) constructs was expressed as N-terminal F1 (YFP fragment: 1-158) fusion and JNK1 was expressed as N-terminal F2 (YFP fragment: 159-239) fusion with a C-terminal FLAG-tag for both. Full-length c-JUN (1-331, UniProt ID: P05412-1) was cloned into pcDNA 3.1 vector containing C-terminal FLAG-tag or as N-terminal F1 fusion. Cells were assayed 24 h after transfection from three different wells for each pair of constructs. After suspending and washing the cells in PBS, $\sim 2 \times 10^4$ cells were transferred into 384-well black plate and fluorescence intensity was measured using Cytation™ 3 (BioTek Instruments) with excitation/emission wavelength of 505/535 nm. The same aliquots of cells were subsequently subjected to Western-blot. For imaging, cells were cultured in a 8-Well Glass Bottom μ -Slide plate (#80827, Ibidi), transfected and fixed with 4% paraformaldehyde solution 24 hours post-transfection, stained with 0.1 μ g/ml DAPI and imaged with EVOS M7000 Imaging System (Thermo Fischer Scientific). Images were processed using ImageJ software and nuclear localization of the fluorescent signal was calculated as a percentage of the total fluorescence intensity.

Yellow Fluorescence Protein (YFP) based BiFC assay was performed as described before to monitor interaction and localization of the JNK-DCX complex in HEK293T and COS1 cells [30]. JNK1 was expressed as N-terminal F2 fusions and DCX-WT(1-366) as C-terminal F1 fusion. For imaging, cells were seeded to onto uncoated glass cover slips placed in 12-well tissue culture plates. 24 hours after transfection, the cells were washed twice with PBS and fixed with 4% paraformaldehyde solution, then permeabilised with 0.2 % Triton X-100 and blocked with 1 % BSA. Cells were then incubated with primary antibody (anti-FLAG) 1:200 (Sigma, #F1804), anti- α -tubulin 1:200 (Sigma #T6074) (room temperature, 1 hour), washed with ice-cold PBS, then incubated with appropriate secondary antibody tagged with fluorescent probes (Alexa 488, Alexa 633) on RT, 1 h. Finally, cell nuclei were stained with DAPI (0.1 μ g/ml) for 5 minutes, washed with ice-cold PBS and mounted onto glass microscopy slides with BioMeda™ Gel Mount mounting media. Images were acquired on a ZEISS LSM 800 confocal laser scanning microscope equipped with a 63×1.4 NA objective (Biological Optical Microscopy Platform, University of Melbourne).

For luciferase complementation NanoBiT (Promega) assays [140], cDNAs were sub-cloned into LgBiT and SmBiT expression vectors: MAP kinases (JNK1 or p38 α) were expressed as N-terminal LgBiT fusions, while ATF2 and DCX constructs as N-terminal and C-terminal SmBiT fusion proteins,

respectively. 2×10^4 cells per well were seeded onto a white 96-well plate (Greiner, 657160) 24 hours prior to transfection and co-transfected with 50 ng of LgBiT and 50 ng of SmBiT constructs using Lipofectamine 3000 reagent in Opti-MEM. 4 hours after transfection and cells were starved for 20 hours before assayed using the Nano-Glo reagent (Promega) according to the manufacturer's instructions in a Cytation 3 plate reader and thermostated at 37°C with maintained 5% CO₂ level. MAPK stimulation was initiated by adding 10 µg/mL anisomycin (#A9789, Sigma-Aldrich). Transfected and treated cells were subjected to Western-blot. In the case of HTM-6 cell line, 2 µg/ml doxycycline was added 20 hours prior the measurement to induce MKK6-EE expression and the luciferase activity was measured (for 10-15 minutes) in living cells after addition of 10 µM luciferase substrate (Coelenterazine h).

3.10 Transcription activation assays

ATF2-TAD (19-100) constructs were subcloned into pBIND vector as N-terminal fusion with GAL4 DNA binding domain (1-147). The pBIND vector also expresses *Renilla* luciferase from a constitutive promoter as a transfection control. 2×10^4 HEK293T cells per well were seeded onto a white 96-well plate 24 hours prior to transfection and co-transfected with 50 ng GAL4-ATF2 and 50 ng pGL4.31 reporter vector using Lipofectamine 3000 in DMEM. The pGL4.31 contains the Firefly luciferase expression cassette driven by 5×GAL4 promoter, which consists of five consensus binding sequences for the GAL4 DNA binding domain. After 4 hours of transfection the medium was changed to DMEM, and cells were serum starved for 20 hours and assayed with Dual-Glo® Luciferase reagents (Promega, #E2920) according to manufacturers instruction using Cytation 3 plate reader with luminescence filter. RLU (Relative Luminescence Unit) were calculated as Firefly Luciferase activity/Renilla Luciferase activity. 10 ng Cerulean-JNK1-FLAG, Cerulean-p38α-FLAG or Cerulean-empty-FLAG, were co-transfected with 50+50 ng GAL4-ATF2 and reporter vector where indicated. Inhibitor treatments were performed adding 1 µM JNK-IN-8 (Selleckchem, #S4901), 1 µM SB202190 (Sigma-Aldrich, #S7067) , 1+1 µM JNK-IN-8 + SB202190 or 0.1% DMSO (for control) 8 hours before measurement. HT-MLK3-MKK7 (Puromycin), HT-MKK6EE (Hygromycin) or HT-MLK3-MKK7/MKK6EE (Puromycin+Hygromycin) cell lines were induced by adding 2 µg/ml doxycycline 16 hours before the measurement. Samples were subjected to Western-blot analysis as well and GAL4-ATF2 expression was detected using anti-GAL4 antibody (Santa-Cruz, #sc-510) or phospho-specific antibodies mentioned above. All experiments were performed independently (on different days) at least 3 times and tested with paired, two-sided Student's t-test.

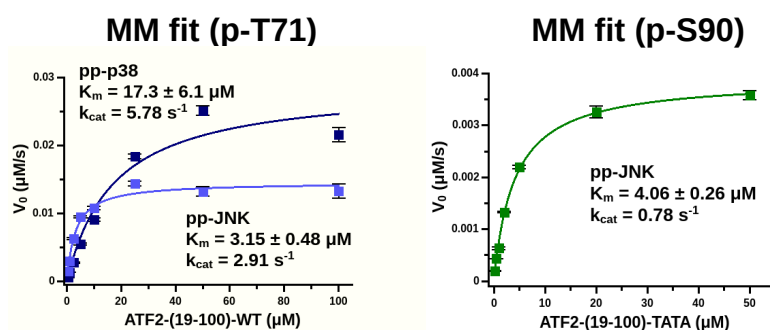
3.11 Simulation of TAD phosphorylation

Simplified rule-based modeling of JNK-p38-ATF2 cellular network was carried out with the software package BioNetGen with the ordinary differential equation solver running on a desktop PC [141]. This system is capable of handling various binding and reaction rules and can be tempered to experimental datasets.

First kinetic parameters for ATF2-JNK (k_{on1} , k_{off1}) and ATF2-p38 (k_{on2} , k_{off2}) binding and rate

A

Standards (halving dilution):



B

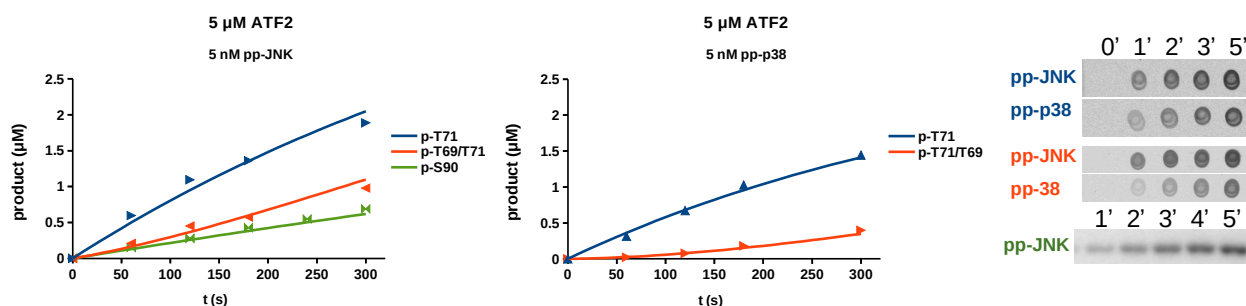


Figure 11 Phosphorylation of ATF2 phosphoswitches by pp-p38 and pp-JNK1. (A) 2X dilution series of fully phosphorylated ATF2 were used to confirm the linear range of detection by quantitative immunoblot for p-T71 and pp-T69/T71 or by radioactive phosphorimaging for pS90 and to determine the regression line for concentration versus signal. Michaelis-Menten (MM) fit of T71 phosphorylation of ATF2-WT by pp-JNK and pp-p38 based on immuno-dot-blot are shown in the left graph and S90 phosphorylation by pp-JNK1 based on phosphorimaging data of ATF2-TATA construct are shown in the right. Error bars show uncertainty of linear fit for particular concentrations. (B) Reaction rates and binding rates were fitted simultaneously to p-T71 and p-T69/T71 phosphorylation of different concentration of ATF2 in *in vitro* kinase assay. Phosphorylation was detected by quantitative Western-blot (WB) using different phospho-specific antibodies, or by radioactive phosphorimaging for pS90 (in green; see panel c). Graphs show one concentration examples of the kinetic data (points: dot-blot data, lines: BioNetGen model after fitting). constants for ATF2 T69, T71 and S90 phosphorylation (k_1 , k_2 , k_3 , k_4) were determined based on *in*

in vitro kinase assay with quantitative detection of T71, T69/T71 and S90 phosphorylation. The phosphorylation reaction roles were defined based on the literature, where the T69 and T71 phosphorylation are a two-step event which can happen distributively or processively depending on $k_{\text{off}}/k_{\text{cat}}$ ratio [67]. Reaction rate for $\text{T69/T71} \rightarrow \text{pT69/T71}$, $\text{T69/T71} \rightarrow \text{T69/pT71}$, $\text{pT69/T71} \rightarrow \text{pT69/pT71}$ and $\text{T69/pT71} \rightarrow \text{pT69/pT71}$ by JNK was set to be equal (k_1) as we have no detailed information about its preference. In the case of p38 mediated phosphorylation events, the T71 phosphorylation rate of T69 phosphorylated ($\text{pT69/T71} \rightarrow \text{pT69/pT71}$) was set to be slower (k_4), compared to the other three possible p38-mediated phosphorylation events, which were set to be equal (k_3) [66]. Parameters were adjusted simultaneously to the anti-p-T71 and anti-pp-T69/T71 data from *in vitro* kinase assay for pp-38 or pp-JNK with various concentration (0.5-100 μM) of ATF2 substrates. The differential evolution algorithm of PyBioNetFit were used for the fitting of 3 parameters to 60 data points for JNK, and 4 parameters to 72 data points for p38, where the chi squared objective function value was minimized [142]. Fitting gave reaction and binding rates for JNK (k_1 : 3.52/s, $k_{\text{on}1}$: 5.6/ $\mu\text{M/s}$, $k_{\text{off}1}$: 19.6/s) and for p38 (k_3 : 8.02/s, k_4 : 1.67/s (for $\text{pT69} \rightarrow \text{pT69/pT71}$), $k_{\text{on}2}$: 17.2/ $\mu\text{M/s}$, $k_{\text{off}2}$: 429/s). See one ATF2 concentration example on Figure 11B with the fitted curves. The derived binding affinities ($k_{\text{off}}/k_{\text{on}}$) are $\sim 3.5 \mu\text{M}$ and $25 \sim \mu\text{M}$ for JNK and p38, respectively and are in a good agreement with K_M from the MM-fit of the same dataset (Figure 11A). As expected the double phosphorylation of ATF2 were fitted with $k_{\text{off}} \gg k_{\text{cat}}$ for both MAPKs, but more prominently in the case of p38 which indicates the distributive model proposed by Waas et al. (2001) [66]. The rate of S90 phosphorylation by JNK (k_2) was derived from the MM-fit from $[\gamma\text{-}^{32}\text{P}]\text{ATP}$ based *in vitro* kinase assay data using the ATF2-TATA substrate (Figure 11) and the kinetics of S90 phosphorylation can be modeled using $k_{\text{on}1}$ and $k_{\text{off}1}$ (green lines on Figure 11B).

To simulate the cellular network of ATF2-p38-JNK, we included additional binding rules in the BioNetGen model based on our biochemical experiments (Figure 30A). JNK-ATF2 binding is not affected by the phosphorylation state of proteins and ATF2 binds to the DRS of JNK. ATF2 binds to the DRS and FRS of pp-p38 in a bipartite manner ($k_{\text{on}2}$, $k_{\text{off}2}$), but only when p38 is phosphorylated and ATF2 is not phosphorylated on S90. p38 binds to the DRS with only low affinity ($k_{\text{on}3}$, $k_{\text{off}3}$, $K_D \sim 1 \text{ mM}$) when bipartite binding is not possible. To mimic the in-cell environment, activity of upstream kinases (k_7 for JNK activation and k_6 for p38 activation) and different phosphatases were incorporated to the system as a first order reaction. Pathway activation was initiated from a pre-equilibrated state with baseline k_7 ($k_{\text{eq}7}$) and k_6 ($k_{\text{eq}6}$) activity. To imitate anisomycin stimulation, signaling was started

with increased k_7 (k_{stim7}) and k_6 (k_{stim6}) activity. For the determination of k_7 , k_6 and dephosphorylation rates, in-cell NanoBit measurements with ATF2 and p38 probes and related western blot data were used upon anisomycin treatment (Figure 30B). The NanoBiT assay data were simulated with of ATF2, JNK and p38 (1 μ M), and additional exogenous p38 (1.65 μ M). Using PyBiNetFit, we determined kinase (k_{stim7}) and phosphatase (dp1) rates acting on JNK to fit the pp-JNK western-blot data, where the maximum activity at 40 min of anisomycin treatment was set to be 10 % of the total JNK pool. Basal activity of JNK was introduced with the k_{eq7} rate constant. Next, two sets of NanoBiT data on the ATF2-p38 complex - CTR and JNK-IN-8 treated - were used in PyBioNetFit for the fitting of k_{stim6} , dp2 and dp4 (phosphatase activity on p-S90). Basal activity of p38 was introduced with the k_{eq6} rate constant. These model parameters predicted that 5% of the p38 pool gets activated after 40 minutes of anisomycin treatment. The phosphatase activity on T69 and T71 (dp3) was determined using the CTR and JNK-IN-8 treated pT69/pT71 Western-blot signal, assuming that 80% of ATF2 are phosphorylated after 40 minutes in the control experiment (CTR). To test our fitted parameters we simulated the system with S90N and MUT4 mutant ATF2 as well. In the case of JNK-IN-8 treatment, k_1 and k_2 were set to 0, in the case of the S90N mutant, k_{on2} was set 4.5x fold higher compared to WT, and k_2 was set to 0 and in the case of MUT4 k_{on2} was set 0.07x less than WT. Parameter scanning with various k_{stim6} and k_{stim7} rates equally distributed in logarithmic space was performed using the final model and endogenous protein phosphorylation levels were calculated for 40 minutes after stimulation. The level of pT69/pT71 for S90N and WT ATF2 were plotted in a 3D surface plot as a function of the simulated pp-JNK and pp-p38 levels. In the contour plots the black line indicates points with 45° gradient function, where the partial derivative for pp-JNK and pp-p38 is equal.

Final model is provided in the Appendix Code written in BNGL language and detailed definition of parameters is found in Appendix Table 2.

4. Results

4.1 Characterization of the JNK-ATF2 interaction

The two well-known JNK substrates, ATF2 and c-Jun, are members of the AP-1 transcription factor family and both contain a C-terminal bZIP domain (basic region + leucine zipper domain) responsible for dimerization and DNA-binding. Although their N-terminal transactivation domain (TAD) has slightly different composition regarding MAPK dependent phosphoswitches, it is known that they both utilize a JNK binding D-motif [77, 78] (Figure 12A).

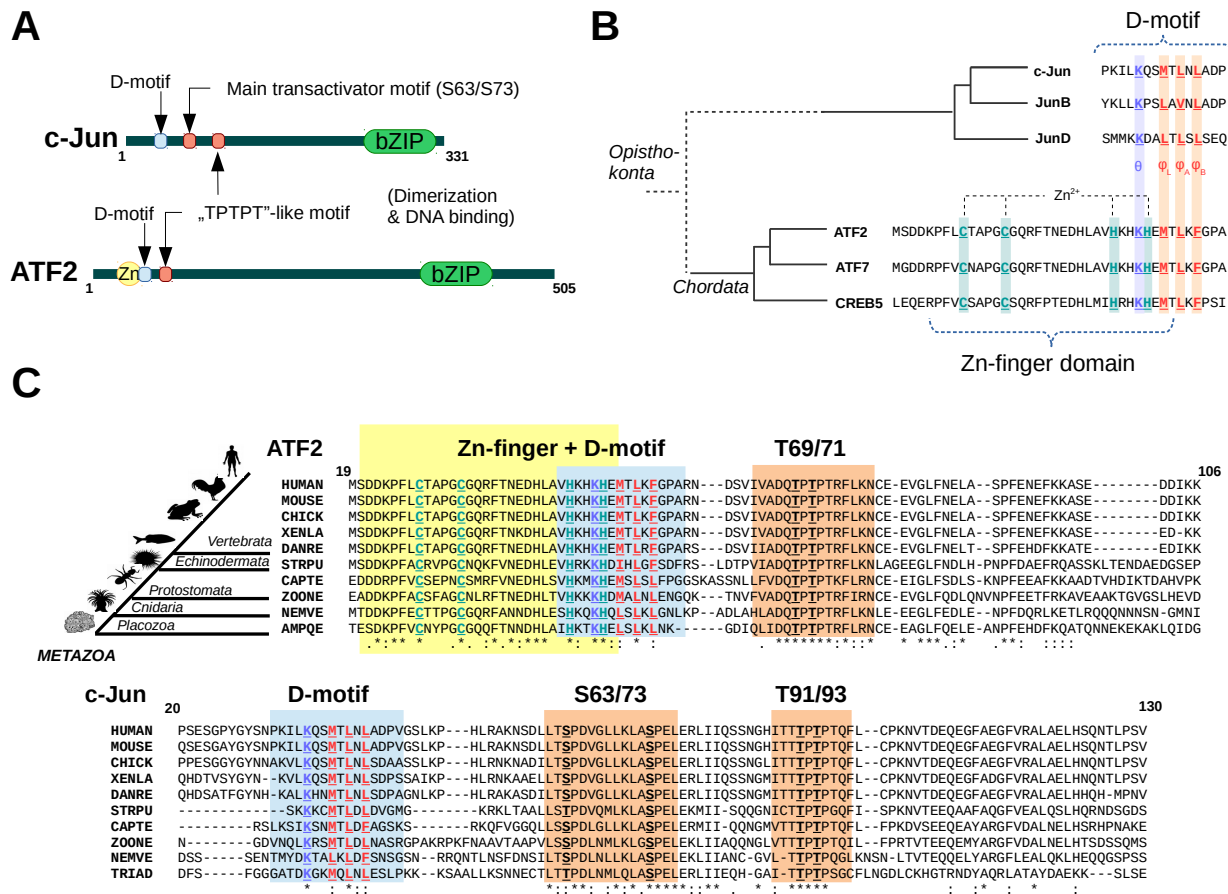


Figure 12. Evolutionary conservation of AP-1 transcription factors (Jun and ATF). (A) Schematic representation of the full length human c-Jun and ATF2. (B) Phylogenetic tree of JUN and ATF paralogs. (C) Sequence conservation of the transactivation region in ATF2 and c-Jun orthologs. (HUMAN: *Homo sapiens*, MOUSE: *Mus musculus*, CHICK: *Gallus gallus* – bird, XENLA: *Xenopus laevis* – frog, DANRE: *Danio rerio* – fish, STRPU: *Strongylocentrotus purpuratus* - sea urchin, CAPTE: *Capitella teleta* – worm, ZOONE: *Zootermopsis nevadensis* – termite, NEMVE: *Nematostella vectensis* - sea anemone, AMPQE: *Amphimedon queenslandica* – sponge, TRIAD: *Trichoplax adhaerens* - Placozoa).

4.1.1 Evolutionary sequence analysis of ATFs and JUNs

In order to examine the ATF and c-JUN TAD architecture, we searched for paralogs and orthologs using blastp in all non-redundant protein sequence database in vertebrates and non-vertebrates. Interestingly, we found that in contrast to JUN paralogs, all ATF transcription factors in human (ATF2, ATF7 and CREB5) contain an N-terminal C2H2-type Zn-finger domain that overlaps with the basic region (θ) of the D-motif (Figure 12B). Although the structure of a short ATF2 D-motif peptide (46-KHKHEMTLKFG-56) in complex with JNK3 was earlier determined by X-ray crystallography, the IC_{50} value of this peptide in a kinase assay where JNK mediated phosphorylation of ATF2(2-115) was monitored in vitro was high ($>100 \mu\text{M}$) compared to other JNK binding motifs (0.3-8 μM) [93]. According to our sequence analysis, the proximal arrangement between the structured Zn-finger domain and the D-motif sequence seems to be evolutionarily conserved in ATFs in *Metazoa* (Figure 12C), suggesting that the binding needs to be studied using protein constructs including both regions.

4.1.2 Zn-finger dependent interaction of ATF2 with JNK

To identify the JNK-binding region in ATF2, we performed interaction mapping with segments of the transactivation region (ATF2(19-100)) by GST pull-down assays using purified JNK1 (Figure 13). According to our result, neither the Zn-finger (19-50) nor the D-motif (42-55) alone was potent for JNK binding. The minimal binding region (19-58) contained both the Zn-finger and the D-motif. The purified ATF2 (19-58) bound JNK with micromolar affinity ($\sim 5 \mu\text{M}$) (Figure 14A).



Figure 13. Mapping of ATF2-TAD region responsible for JNK1 binding. GST-pulldown experiment was performed with recombinantly expressed GST-ATF2 baits and JNK1 prey. GST control was used as negative control to detect unspecific binding of the prey (GST; M – Molecular weight marker, JNK – load)

In order to study the role of the Zn-finger, we treated the GST-ATF2(19-58) bound glutathion-beads with EDTA (2 mM for 30 min). This chelating agent diminished binding indicating that the intact

structure of the Zn-finger is required for the interaction. The charge reversal mutation of the basic region of the D-motif (K48E) also impaired binding (Figure 14A). Next we compared the AP-1 TAD constructs, MBP-ATF2(19-100) and MBP-c-Jun(1-78). They both showed similar affinities towards JNK (~4 μ M) but only the JNK-ATF2 interaction was sensitive to the presence of EDTA. A charge reversal mutation in ATF2 or in c-Jun (K48E or K35E, respectively) impaired binding similarly. Not surprisingly, ATF2(19-100) and c-Jun(1-78) showed only weak binding towards p38 α and ERK2 as their D-motif sequence confers to the JNK-binding NFAT4-type class (Figure 14B, raw data included in Appendix Figure 1).

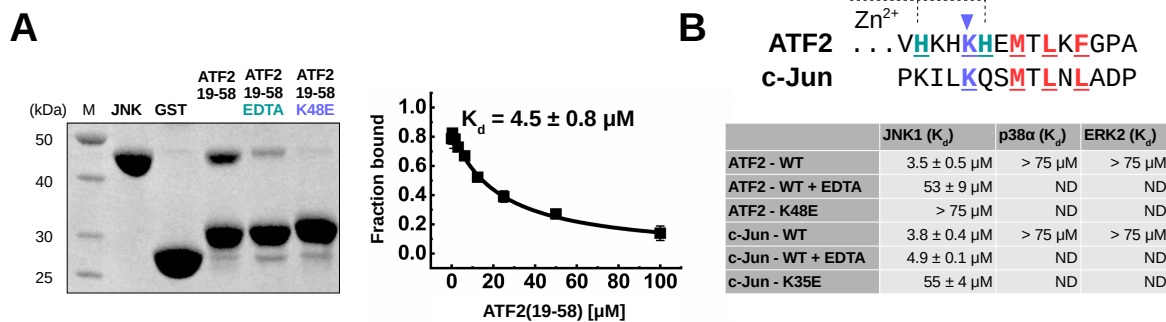


Figure 14. ATF2-JNK interaction is sensitive to the elimination of Zn²⁺. (A) GST-pulldown experiments in the presence of 2 mM EDTA or K48E mutation. The competitive fluorescence polarization experiment shows the binding of the purified minimal ATF2(19-58) to JNK1. (B) Fluorescence polarization assays were performed with longer MBP tagged ATF2 and c-JUN constructs (19-100 and 1-78, respectively) with or without EDTA treatment or with a charge reversal mutant. Binding affinities are shown in the table. In the case of very weak interactions, the binding curve could not be fitted (the K_d is above the limit of quantification of this assay, approximately ~ 75 μ M). ND means not determined.

We further assessed the contribution of Zn-finger on binding by isothermal titration calorimetry (ITC). As in the case of fluorescent polarization assay, the presence of EDTA caused a ~10 fold weaker interaction of JNK and ATF2. While the enthalpic contribution (Δ H) was nearly the same in the untreated and treated sample, the entropic cost ($-T\Delta$ S) of the binding was higher in the presence of EDTA. This suggests that an intact Zn-finger is necessary for binding by decreasing the flexibility of critical D-motif residues.

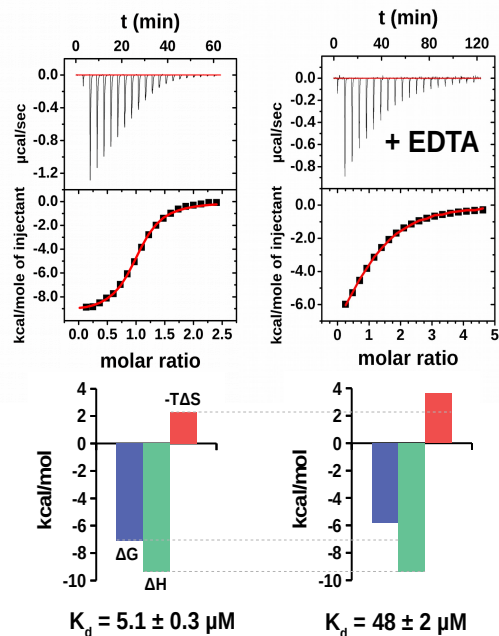


Figure 15 ITC measurements of JNK1 and ATF2(19-58) binding in the absence or presence of 2 mM EDTA. ITC data are shown with raw injection heats and the corresponding specific binding isotherms. Lower panels show the enthalpic (ΔH) and entropic ($-T\Delta S$) contributions to binding free energy (ΔG).

4.1.3 Structure determination of the JNK-ATF2 complex

Next our goal was to determine the high-resolution structure of the Zn-finger+D-motif module bound to JNK. Unfortunately the crystallization trials for WT ATF2(19-58) and JNK1 failed, therefore we decided to examine the interaction with NMR spectroscopy and use *in silico* modeling.

4.1.3.1 NMR spectroscopy

The ATF2 TAD (19-106) was previously assigned and its structure was determined by NMR spectroscopy [92]. We used Heteronuclear Single Quantum Coherence Spectroscopy (HSQC) to map the residues involved in JNK interaction. After titration of 50 μM ^{15}N -labeled ATF2(19-78) with JNK at 1:0.5 and 1:1 stoichiometric ratio, we monitored the intensity of HN cross-peaks in the 2D [^1H , ^{15}N] HSQC spectra. Compared to the spectra of apo ^{15}N -ATF2, we detected decrease in the peak intensity covering the D-motif residues and most of the Zn-finger residues as well (Figure 16). Less changes were observed in the N-terminal unstructured part of Zn-finger and around the TPTP phosphorylation motif.

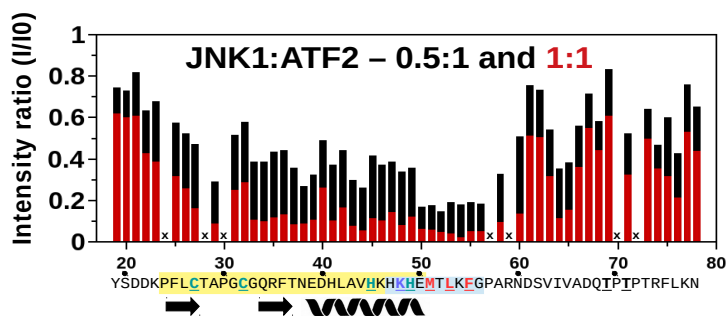


Figure 16 Interaction region mapping by HSQC spectroscopy. ¹⁵N-labeled ATF2(19-78) was mixed with JNK1 in two different molar ratio, and intensity changes for ATF2 ¹H-¹⁵N HSQC peaks for the 0.5:1 (black) or 1:1 (red) JNK1:ATF2 experiment were plotted. ‘x’ indicates resonances of prolines or residues which are not resolved in the spectra.

Combined dNH and N chemical shift perturbations appeared only at low level in the presence of JNK. In the case of 1:1 ratio the CSP-s were more prominent at the D-motif and its preceding region, although the analysis of the shifts was not straightforward because of the largely broadened peaks (see Appendix Figure 2A).

The low chemical shift perturbations and extensive intensity decrease could refer to two properties to the interaction: 1) the exchange rate between the free and bound form is slow to intermediate on the chemical shift time scale and 2) the peak intensity decreased because a large molecular weight complex is formed upon JNK1 binding (~55 kDa) where the higher relaxation rates cause the peaks to broaden beyond detection. Similar phenomenon was observed in the case of MKK4 peptide (74 AA) titrated with p38 (41 kDa). This complex has similar dissociation constant ($K_d = 4.1 \mu\text{M}$) as the ATF2-JNK interaction and binding dynamics were characterized by various NMR methods [56]

HSQC titration showed, that in addition to the expected changes in the ATF2 D-motif, the intensity of Zn-finger residues also decreased suggesting that this small domain contributes to binding. Because several ATF2 residues lost their intensity in the bound form, we were not able to determine the structure of the JNK1 bound form of ATF2 with NMR based methods.

4.1.3.2 *In silico* modeling and model validation of the ATF2-JNK complex

In order to gain more insights into how Zn-finger contributes in JNK binding, we used a High Ambiguity Driven protein Docking (HADDOCK) approach [120]. This software is able to handle coordinated metal ions and ensemble input structures which is not possible in the Rosetta based FlexPepDock protocol. Moreover, after its general rigid body minimization protocol, it is capable of performing flexible refinement of both peptide and protein side chains at the interface by varying dihedral angle and side chain conformation.

We built our input ensemble based on the previously determined ATF2-Zn-finger NMR structure (PDBID: 1BHI) and D-motif-JNK X-ray structures. In the starting ensemble the bound form of D-motifs was stitched together with the Zn-finger in multiple conformations, which are compatible with the JNK surface. We used evolutionarily conserved unambiguous distance restraints only for the hydrophobic motif-DRS to drive the docking procedure (see Figure 10 in Materials and methods). The C2H2 tetrahedron structure were also maintained by unambiguous restraints during the docking process. After rigid body docking, the software performed multiple round of semi-flexible refinement on residues in the interaction surface which was then followed by explicit water refinement.

To validate our model we mutated residues in the Zn-finger playing a role in the interaction with JNK. The lowest energy structure shows that K48 interacts with the charged groove of the JNK (Figure 17). Both the alanine and glutamate mutant of this residue disrupted the binding (see Fluorescence polarization measurements in Figure 17), which indicates the importance of this electrostatic contact. The V44 could take part making hydrophobic contact with JNK, as its alanine mutants slightly increased, and its glutamate mutant increased the K_d by ~ 10 fold (thus decreasing the binding affinity). According to the model the Q34 and H47 side chains are not in the range of hydrogen bonding distance but within 6 Å from D326, 4.5 Å from the E126 side chains in JNK, respectively. In order to test the orientation of the zinc finger in the model, these two amino acids seemed to be a good choice for mutagenesis. The H47E caused weaker binding but the H47R bound more than ~ 10 x stronger than WT, possibly because of new salt bridge formation with E126. Similarly, the Q34R mutant had stronger binding. The double mutant bearing both arginines (Q34R/H47R) further enhanced binding. The Q34R/H47R had 100x higher binding affinity compared to wild-type (Figure 17), therefore we decided to set up crystallization trials with this mutant.

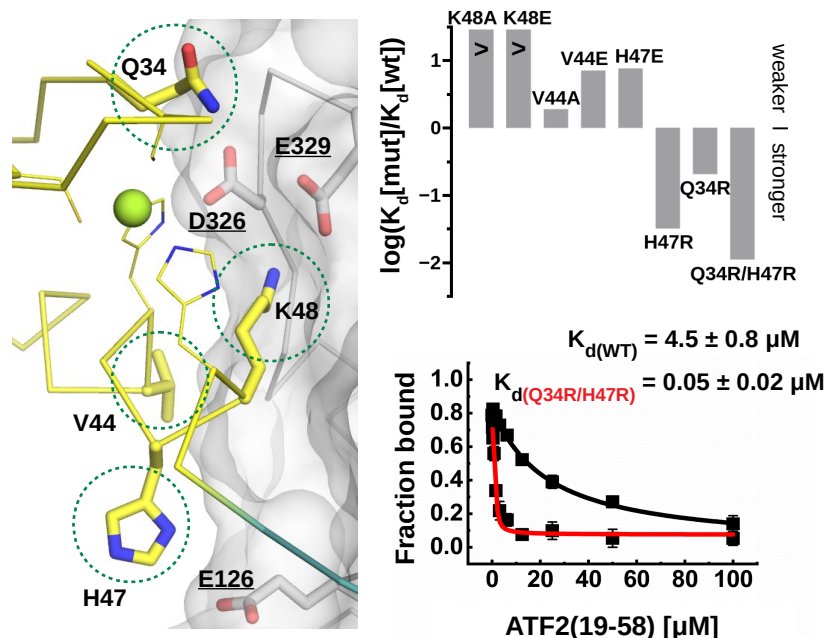


Figure 17 HADDOCK model of the ATF2(19-58)-JNK1 complex. Lowest energy structure calculated by HADDOCK2.2 (left). Binding affinity of the MBP-ATF2(19-100) interface mutants were compared to wild type (WT) by competitive fluorescence polarization based binding assay (see raw data in Appendix Figure 1). The double mutant ATF2(19-58) binds JNK 100x stronger than the wild-type as shown the in competitive binding curves.

4.1.3.3 Crystal structure of the ATF2-JNK complex

We successfully crystallized and solved the structure of the minimal ATF2 (19-58) _Q34R/H47R in complex with JNK at 2.7 Å resolution (PDB ID: 6ZR5). Crystallographic data and refinements statistics are summarized in Appendix Table 1. The crystal structure showed that hydrophobic amino acids from ATF2 D-motif - M51, L53 and F55 - bind in the hydrophobic pockets, similarly to other NFAT4 types D-motif-JNK structures. The K48 binds in the negatively charged CD groove and its ε-amino group is within hydrogen bonding distance with the carboxyl group of E126 and the carbonyl oxygen of W324 (Figure 18A). The engineered Q34R and H47R amino acids form salt bridges with D326 and E126 respectively, explaining the stronger binding affinity (Figure 18C). Apart from those contacts, the F36 and V44 side chain is within 4 Å from JNK in the zinc-finger, but only V44 seems to take part in hydrophobic interaction, as shown in the HADDOCK model above. No other elements from the α-helix nor from the β-sheet are involved in direct contact with the JNK surface. Our crystallographic model is in good agreement with the HADDOCK model of the wild-type ATF2-JNK

complex (RMSD=0.9 Å, Figure 18B), and provide the first biologically relevant structure of JNK1-ATF2.

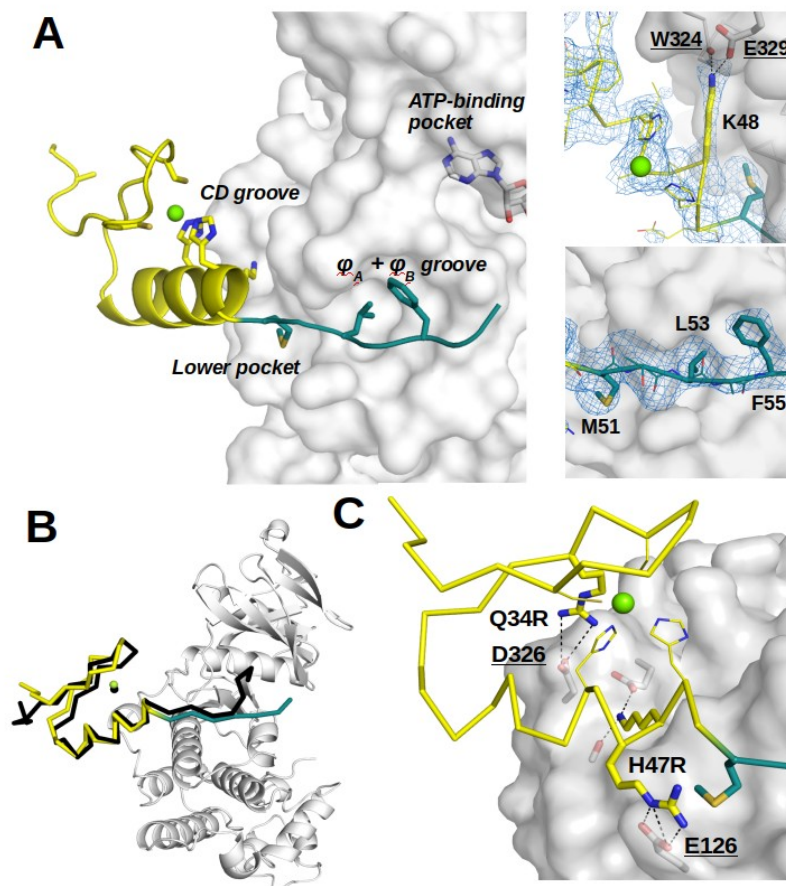


Figure 18 Crystal structure of the JNK1-ATF2(Q34R/H47R) complex. (A) Panels show the JNK1-ATF2 structure determined by X-ray crystallography. Zoomed-in views of the CD-groove highlight the basic K48 (top) and the hydrophobic groove with M51, L53 and F55 (bottom) from the ATF2 D-motif. The simulated annealing Fo-Fc omit map of ATF2 is contoured at 1.5σ . (B) Superposition of the HADDOCK model (black) and the crystal structure (yellow+cyan; the RMSD for ATF2 C α atoms, using JNK as the reference, was 0.9 Å) (C) Zoomed-in view of the Q34R and H47R region from the JNK1-ATF2 crystal structure. Both arginines are involved in forming new salt-bridges that increased the binding affinity.

4.1.4 Activation of ATF2 by JNK in living cell

To highlight the importance of the Zn-finger+D-motif module in JNK binding we examined the full-length ATF2 (1-505) in HEK293T cells. We tested the K48E charge reversal mutant and CACA (C27A/C32A) zinc-finger disrupting mutant in Yellow Fluorescent Protein (YFP) fragment complementation experiment. ATF2 was tagged on the N-terminus with the F1 YFP fragment and

JNK1 had an N-terminal F2 YFP fragment. The presence of K48E and CACA mutations decreased the fluorescence signal compared to wild-type ATF2. Similarly, L53E (ϕ A pocket mutant) disrupted binding, whereas the TATA (T69A/T71A) phosphorylation site mutant only had minor effect. The YFP fragment complementation assay also shows the localization of the complemented protein-protein complex. While the c-Jun-JNK complex was nuclear, the YFP signal of the ATF2-JNK complex had mostly cytosolic localization. Co-expression of ATF2-JNK BiFC reporters with full-length c-Jun shifted the fluorescent signal from the cytosol to the nucleus. This is in agreement with earlier findings that had demonstrated that nuclear translocation of ATF2 is controlled by cJUN/ATF2 heterodimerization [89].

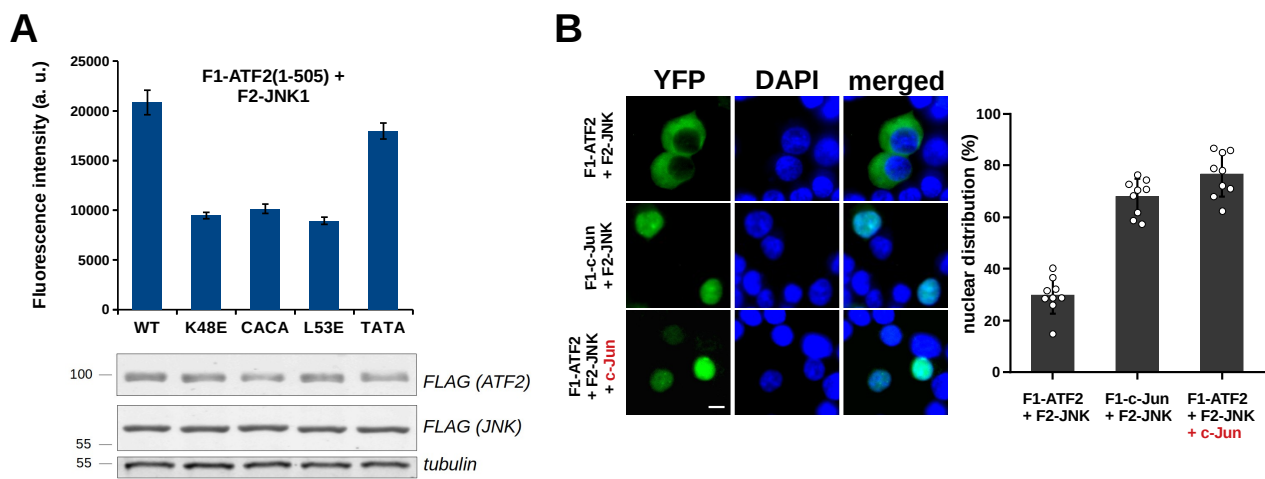


Figure 19 Interaction of JNK + ATF2 in HEK293T cells. (A) Bimolecular fluorescence complementation (BiFC) assay results with YFP fragment (F1+F2) tagged full-length ATF2 constructs and JNK. Fluorescence signal of the transfected cells were measured at 500/535 nm. The panel below shows comparable expression of the YFP fragment tagged constructs (anti-Flag blots). Anti-tubulin was used as loading control. (B) Cellular localization of ATF2-JNK1 and c-Jun-JNK1 complexes. The bottom panels show ATF2-JNK1 interaction when these probes were co-transfected with pcDNA-c-Jun. Scale bar is 10 μ m. Nuclear distribution was quantified as the percentage of nuclear/total fluorescence from n=9 cells from each sample.

In order to examine the JNK-specific phosphorylation of full-length ATF2 we generated an engineered HEK293T cell line, HT-MKK7-MLK3. Here the specific upstream activator of JNK, MKK7 (MAP2K) was fused together with the constitutively activated form of MLK3 (MAP3K, kinase domain) and cloned into a Tetracycline-on based expression vector [139]. In the stable episomal cell line the JNK activity was turned on by doxycycline (DOX) inducible expression of the specific upstream activator. The increased phosphorylation of JNK isoforms was detected by anti-pp-

JNK(T183/Y185) antibody at endogenous level, while the phosphorylation level of p38 was unchanged. After 8 hours of DOX treatment, endogenous ATF2 had elevated phosphorylation level, which was blocked in the presence of JNK-IN-8, a specific covalent ATP-binding site inhibitor of JNK1/2/3 [143] (Figure 20A). The phosphorylation of the transfected full-length F1-ATF2 also increased after DOX treatment, and the TATA mutant had no detectable signal, which proves the high specificity of the anti-pp-ATF2-T69/T71 antibody even in this overexpressed system. Electromobility shift of at the ATF2-FLAG signal (upper band) indicates the presence of the phosphorylated form of ATF2, which was absent in the case of TATA mutant (Figure 20B). Experiments with K48E and CACA mutants showed that the intact zing-finger and the basic residue are important for the efficient phosphorylation of the ATF2 TAD phosphoswitch in the context of full-length ATF2 as well (Figure 20C).

Overall we demonstrated that the zinc-finger+D-motif module is crucial for the JNK mediated phosphorylation of ATF2 in cell-based assays.

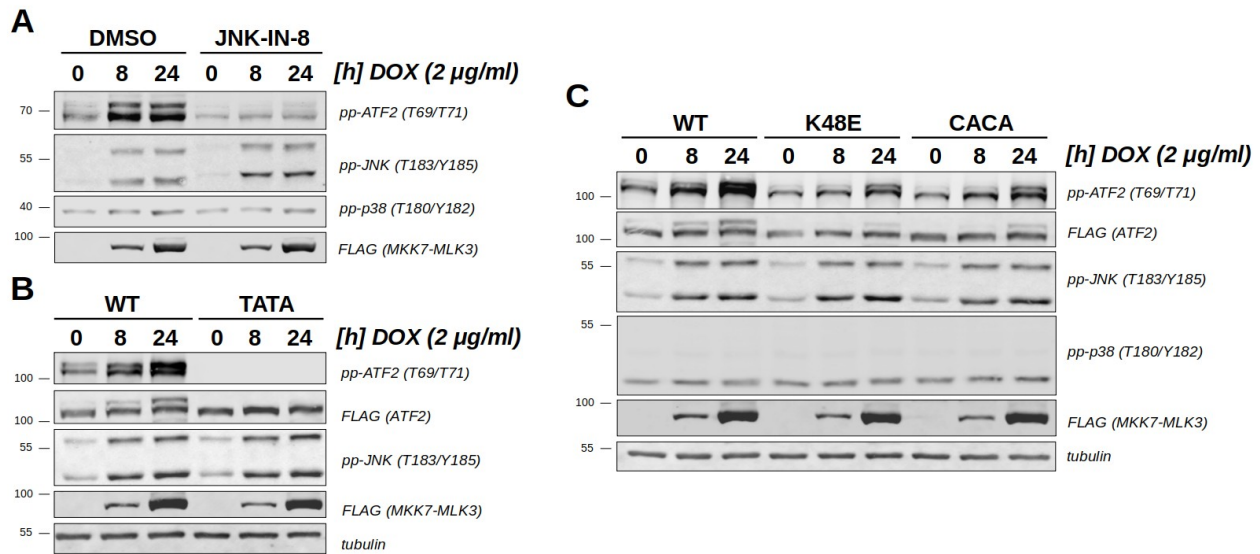


Figure 20 Phosphorylation of ATF2 in HT-MKK7-MLK3 cell line. (A) Expression of MKK7-MLK3 was induced by 2 µg/ml for 0, 8 or 24 hours, and treated with 0.1% DMSO or 1 µM JNK inhibitor (JNK-IN-8) for 1 h before harvest. The samples were subjected to western-blot and developed with the indicated antibodies. (B) HT-MKK7-MLK3 cells were transfected with full length F1-ATF2-WT and TATA constructs and treated with DOX for the indicated time. (C) Phosphorylation of F1-ATF2-WT, -K48E and CACA was compared after the expression of MKK7-MLK3 induced by DOX. Anti-FLAG signal shows similar levels of the transfected ATF2 constructs. Anti-tubulin antibody was used as loading control.

4.2 p38 as an activator of ATF2

As shown in many cellular systems and disease models, ATF2 is not only regulated by JNK but p38 as well [79]. Therefore we wanted to unravel how ATF2 is activated by p38 and what the molecular interface is for their binding. We have already shown that the ATF2-TAD module has no detectable binding toward p38 in the fluorescent polarization assay, where a labeled D-motif was used as the competitor. In contrast, a similar construct, ATF2(19-96) is often used as a reporter substrate for detecting p38 activity from cell lysates. These suggest that the two MAPK - p38 and JNK - might interact with ATF2 in a different manner.

4.2.1 Phosphorylation dependent interaction of p38 and ATF2

Although ATF2 was studied as a p38 substrate in *in vitro* studies as well, the binding affinity has not been measured directly and only the K_M was calculated for ATF2(1-115) (39 μ M) in an enzyme kinetic assay [144]. This suggested a relatively weak interaction compared to classical MAPK substrates.

Luciferase complementation based NanoBiT assay provides high sensitivity to detect protein-protein interactions in the cell. The major advantage of this system compared to other protein-fragment complementation methods is that the reversible complementation of its two fragments (LgBiT and SmBiT) allows monitoring transient protein-protein association events in live cells. The interaction of fusion partners leads to generating a luminescent signal that correlates with the binding strength [140]. We fused WT and the lysine mutant (K48E) ATF2-TAD to SmBiT, p38 α and JNK1 to LgBiT fragments and monitored their interaction in HEK293T cells. After the addition of anisomycin to activate both JNK and p38, the signal from both p38-ATF2-WT and -K48E reporters increased. In contrast, this treatment had no effect on JNK-ATF2 reporters (Figure 21A). These suggest that the p38-ATF2 interaction depends on the phosphorylation state of the kinase and it may not be mediated by the D-motif. For example, for ERK it is known that after activation a new interaction surface is formed that is recognized by phenylalanine containing FxFP motifs [27]. In the ATF2-TAD there is no corresponding sequence to FxFP. Even so, an evolutionarily conserved region of hydrophobic residues (with phenylalanines and leucine) can be found C-terminal to the phosphoswitch. Therefore we mutated these residues and tested the mutants interaction with p38 in the HT-MKK6EE cell line. In this cell line the specific activation of p38 (but not that of other MAPKs) is achieved by inducible expression of the constitutively active MKK6, a p38-specific MAPKK [139]. Using the NanoBiT assay, we observed that the mutation or deletion of two phenylalanine residues (92-FENE~~F~~-96) eliminated the phosphorylation

dependent interaction with p38 (see MUT2, MUT3, MUT4 and 19-90 on Figure 21B). This FENEF motif showed an independent role in this interaction, as the alanine mutant or deletion of the preceding hydrophobic (85-FNEL-88) motif had no effect on binding (MUT1 and MUTΔ) compared to wild-type (19-100).

Next, we wanted to confirm the importance of the newly identified FENEF region using purified proteins. We monitored the phosphorylation of various regions from the ATF2-TAD and its

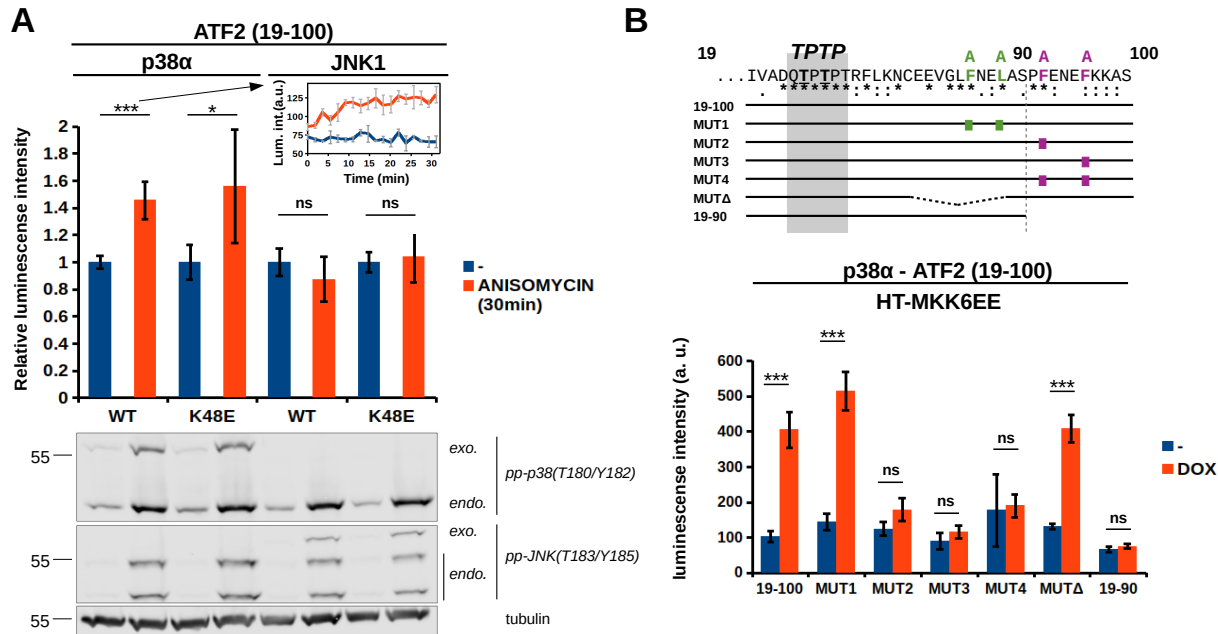


Figure 21 Characterization of p38-ATF2 interaction in living cells. (A) Luciferase complementation assay (NanoBit) on p38-ATF2 and JNK1-ATF2 binding in HEK293T cells. Complex formation between p38α or JNK1 and ATF2(19-100) was monitored after addition of 10 μg/ml anisomycin for 30 min (see inset for p38:ATF2-WT binding) and luminescence values measured in the presence of anisomycin (red) were normalized to control (-; blue). Activation of transfected (exo.) or endogenous (endo.) MAPK was confirmed by anti-pp-p38 and anti-pp-JNK Western-blot. Anti-tubulin antibody was used to demonstrate equal sample load. (B) Mapping critical amino acid residues for pp-p38-ATF2 TAD binding in HT-MKK6EE cells with NanoBit assay. Selective activation of p38 was achieved by DOX treatment for 16 h. (A, B) Error bars show SD (n=3). Statistical significance was calculated by two-sided, unpaired Student's t-test (NS: not significant; *: $p \leq 0.05$, ***: $p \leq 0.001$). Experiments were repeated at least two times with similar results.

mutated constructs (K48E and MUT4) by pp-JNK1 and pp-p38 *in vitro*. The results clearly show that the JNK mediated phosphorylation of ATF2 only depends on the presence of the intact Zn-finger+D-motif module, as the activation was greatly impaired by K48E but was unaffected by the MUT4 (FENEF->AENEA) mutation. In contrary, FENEF motif mutation (MUT4) or the deletion of the C-

terminal region (19-90, 19-83) diminished p38 mediated TAD phosphorylation. Surprisingly, K48E mutation or deletion of the Zn-finger+D-motif (59-100) module had also decreased phosphorylation by p38. This experiment demonstrated that both the Zn-finger+D-motif module and the FENEF motif are indispensable for p38 mediated TAD phosphorylation, whereas JNK mediated phosphorylation only relies on the former region.

In order to gain more insights into the new binding interaction, p38 interaction with ATF2 TAD was explored using NMR spectroscopy. ¹⁵N-labeled ATF2 (19-106) was mixed with double-phosphorylated p38 (pp-p38, T180/Y182) or non-phosphorylated p38, and chemical shift perturbations (CSP) and intensity of HN cross-peaks in 2D [¹H,¹⁵N] HSQC spectra were compared to the apo state. In the case of pp-p38 residues displaying line broadening or large CSPs mapped to the FENEF motif and also to the D-motif, while np-p38 binding affected only the D-motif region. This analysis showed that the major interaction site for pp-p38 is at the FENEF motif but involvement of the D-motif region was also detected.

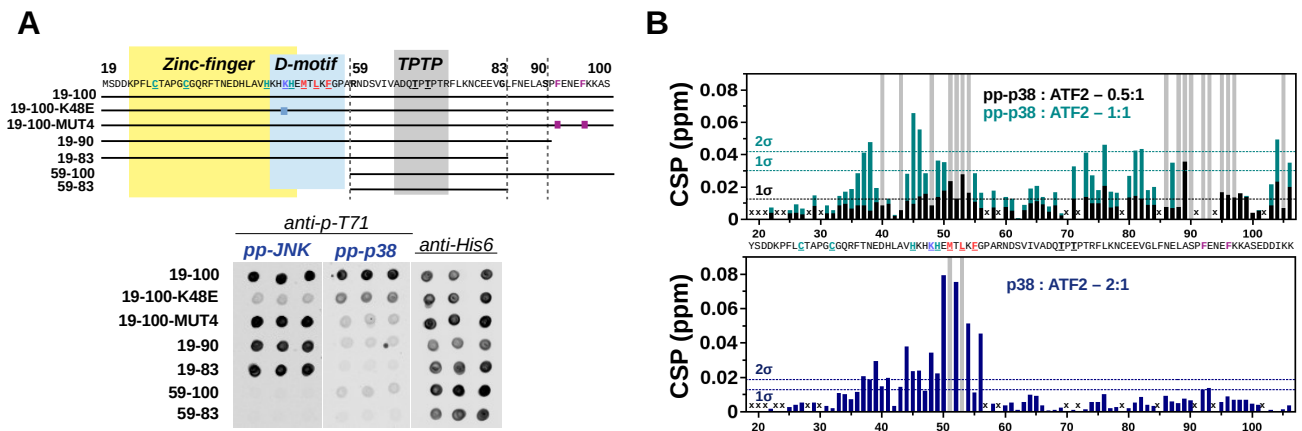


Figure 22 *In vitro* interaction region mapping for ATF2-p38 binding. (A) JNK1 or p38 α mediated phosphorylation of different ATF2-TAD constructs. Purified MBP-ATF2-TAD-His6 fusion proteins were dotted on a membrane (three spots) and then incubated with activated MAPKs. Equal load of the dots was checked by anti-His6 antibody, while target site phosphorylation was probed with anti-phospho-T71 antibody. (B) ¹⁵N-labelled ATF2(19-106; 100 μ M) was mixed with pp-p38 (upper panel) or non-phosphorylated p38 (lower panel) in the indicated molar ratios. Histograms show the ¹H/¹⁵N chemical shift perturbations (CSPs) in the HSQC spectra compared to apo¹⁵N-ATF2 sample. Dashed lines indicate CSPs corresponding to 1 σ or 2 σ changes. Residues displaying line broadening are presented as gray bars. ‘x’ indicates prolines or resonances of residues that were not resolved in the spectra. (See raw spectra and intensity changes upon binding in Appendix Figure 2B.)

Together with the NanoBiT studies, these experiments confirmed the pivotal role of the FENEF motif underlying the phosphorylation state dependent ATF2 TAD interaction with p38.

4.2.2 JNK phosphorylation attenuates p38-SPFENE motif binding

The region adjacent to FENE motif in ATF2 contains a putative S/TP phosphorylation site (S90). This SP site is only conserved in vertebrates, but the serine is replaced by asparagine in all invertebrate ATF2 orthologs (see Figure 23A). Ser90 was shown to be phosphorylated by JNK, but not by p38

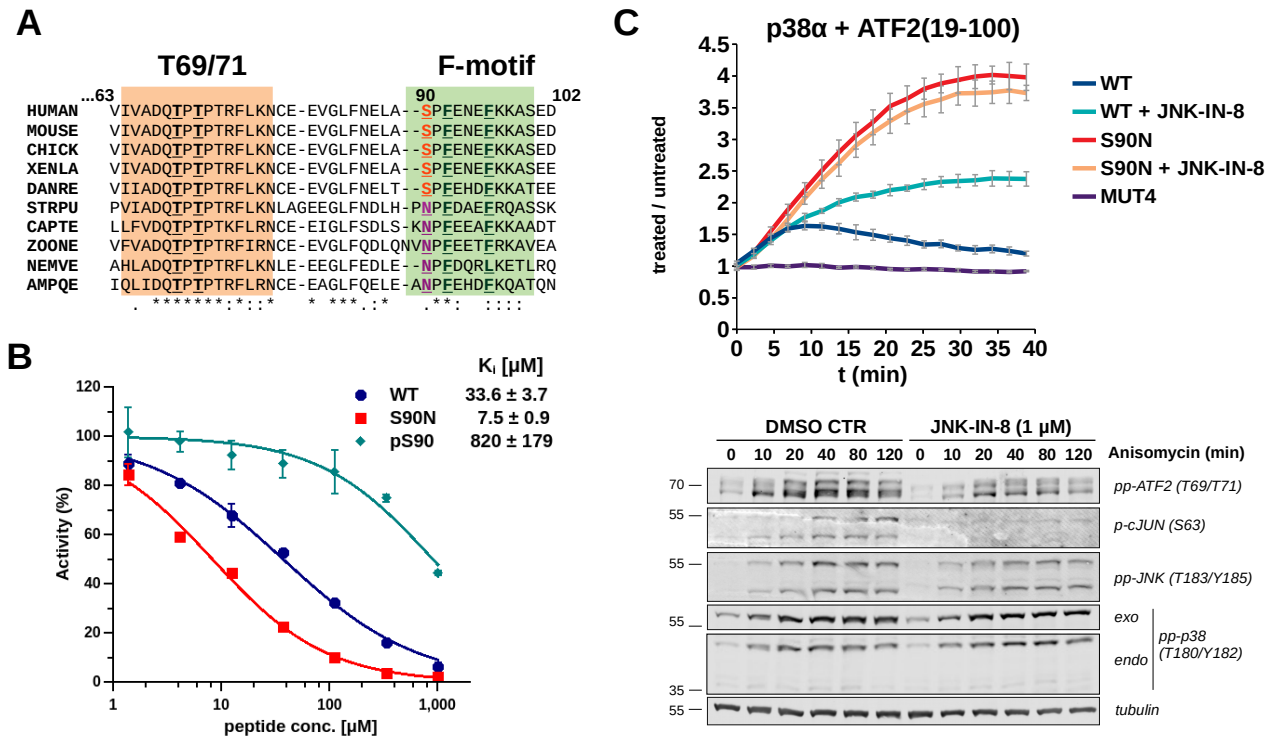


Figure 23 S90 as a regulatory site for p38-ATF2 interaction. (A) Evolutionary sequence conservation analysis of the ATF2-TAD C-terminus. S90 in vertebrates and N90 in invertebrates are highlighted. (B) Inhibition of pp-p38 mediated TAD phosphorylation by SPFENE peptides (83-102) *in vitro*. WT, S90N and S90 phosphorylated (pS90) peptides were added to an *in vitro* pp-p38 → TAD(19-100) phosphorylation reaction. Error bars indicate the uncertainty of the linear fit of initial velocities. The K_i values for the three peptides are highlighted. (C) p38-ATF2 TAD binary interaction was monitored for 40 minutes after addition of anisomycin (10 μ g/ml) using split-luciferase protein-protein binding assay (NanoBit) in live cells. Luminescence signal was normalized to cells not treated by anisomycin (treated/untreated). Elevated phosphorylation of endogenous proteins and the transfected p38 reporter were detected by Western-blot with the indicated phospho-specific antibodies. Anti-tubulin antibody was used as the load control.

[145]. Intrigued by these observations, we synthesized peptides (83-GLFNELASPFENEFKKASED-102, referred to as SPFENE peptide henceforth) with serine, asparagine or phospho-serine at position 90 and tested their inhibitory effect on pp-p38 mediated ATF2 phosphorylation *in vitro*. The three peptides (WT, S90N and pS90) inhibited the phosphoswitch phosphorylation differently (K_i = 33.6 μ M,

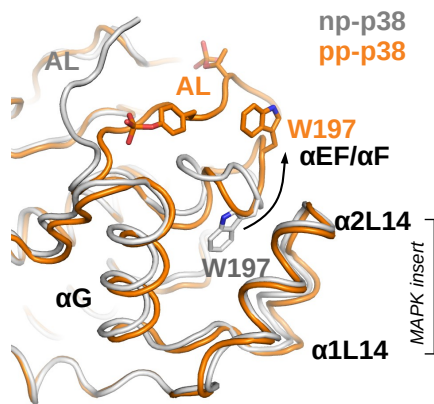
7.5 μM and 820 μM , respectively), which was detected by anti-p-T71 antibody based dot-blots (Figure 23B).

To confirm this observation, we then tested the WT and S90N ATF2-TAD constructs and followed their complex formation with p38 in the NanoBiT assay after anisomycin treatment in HEK293T cells. The WT-ATF2-TAD displayed elevated binding with pp-p38 in the presence of JNK-specific inhibitor (JNK-IN-8, 1 μM) compared to control, presumably because JNK activity - on S90 - decreased the binding of ATF2 to pp-p38 (Figure 23C). As expected, ATF2 S90N showed increased binding over WT-ATF2 to pp-p38 and, in contrast to WT, it was not affected by the presence of JNK-IN-8.

These results showed that N90 promotes p38+ATF2-TAD binding, while Ser90 phosphorylation by JNK in vertebrate orthologs attenuates it.

4.2.3 Structural basis of p38-ATF2 binding

4.2.3.1 X-ray structure of the p38-SPFENEFF motif complex



Available crystal structures show that non-phosphorylated (np-p38) and phosphorylated p38 (pp-p38) have a major difference in their activation loop (AL) (Figure 24). In addition, in non-phosphorylated p38 the FRS pocket is blocked by W197, while in pp-p38 the orientation of the $\alpha\text{EF}/\alpha\text{F}$ loop is altered and the flipped-out W197 residue together with the phosphorylated AL forms the upper rim of the FRS.

Figure 24 Structural alignment of non-phosphorylated (PDB ID: 2OZA) and double-phosphorylated p38 (PDB ID: 6TCA) at the FRS.

We crystallized and solved the structure of pp-p38 in complex with the S90N mutant SPFENEFF peptide (ATF2 83-102) (Figure 25A and Appendix Table 1). As expected, the peptide bound in the FRS pocket of the double-phosphorylated p38. Region 88-101 including the FENEFF motif is visible in the crystal structure. This motif adopts an α -helical structure which is wedged in-between the N-terminal half of αG helix and α2L14 α -helix from the MAPK insert (α2L14). The bulky hydrophobic side-chains of F92 and F96 are buried at the FRS, where F92 is bound by the upper part of the pocket that forms when the activation loop is double-phosphorylated and W197 is flipped out from its original position (**Fig. 5c**). F96 is surrounded by A255 and Y258 from α2L14 helix, I229 and L232 from αG helix, and L195 of αEF helix from the bottom (Figure 25B). The side chain of the N90 residue is lying parallel to the indole ring of

the tryptophan 197, and its oxygen atom from the amide group is within hydrogen bonding distance to the F92 amide nitrogen that provides an N-terminal cap for the FENEF alpha helix (Figure 25C).

The effect of mutations in the p38 FRS pocket on WT-ATF2 phosphorylation were examined in

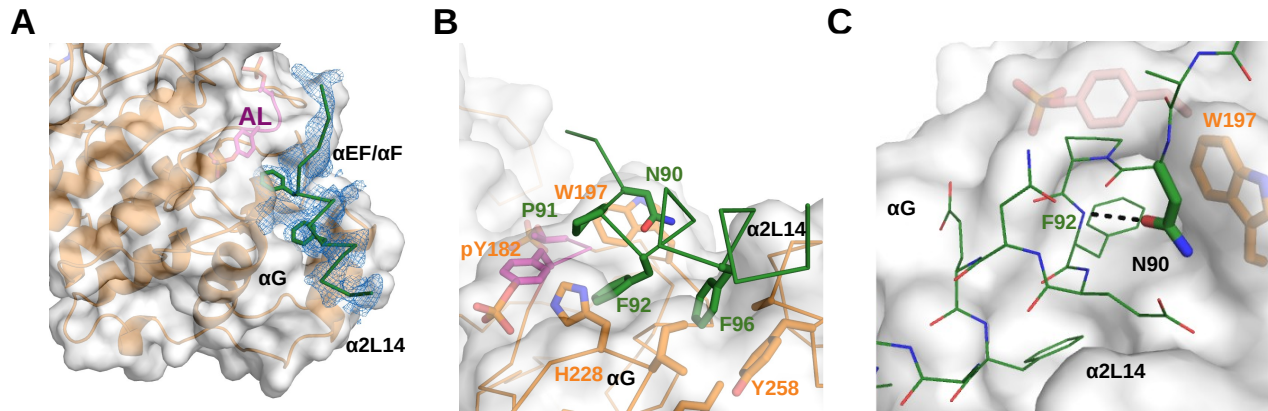


Figure 25 Crystal structure of the pp-p38+ATF2(83-102)_S90N complex. (A) Residues between 88-101 are visible in the crystal structure as shown in the simulated annealing Fo-Fc omit map at 2σ. (B) The helical ATF2 peptide is wedged in-between the N-terminal parts of the αG and α2L14 helices. This FRS pocket (accommodating two phenylalanines, F92 and F96) is lined by pY182 and W197. (C) Structural basis of N90, non-regulatable binding for the invertebrate NPFENEF motif.

previous studies. In consistent with our findings, the W197A mutant p38 had a decreased activity (6%) relative to the wild type, while the alanine mutations of M198 or H199 had only minor affect [146]. Y258A mutation of α2L14 helix reduced the phosphorylation of ATF2 (but not that of MK2, another p38 substrate) and attenuated p38 mediated activation of the AP-1 promoter, but the H228A/I229A mutation from the αG helix had no effect [127].

Our structure provides the first high resolution model for F-type motif – FRS interaction, and explains why ATF2 binding to p38 depends on the activation state of the kinase.

4.2.3.2 Analysis of the N-terminal cap of the FENEF helix in ATF2

While the NMR analysis of wild-type apo ATF2(19-106) by Nagadoi et. Al (1999) [92] showed that the overall structure of the C-terminal part of the TAD is disordered, the N90 mutant SPFENEF peptide bound the pp-p38 in an alpha-helical conformation in the crystal structure. Therefore we wanted to compare the behavior of S90N, WT an p-S90 peptides (83-102) in aqueous buffer by NMR. The secondary structure propensities (SSP) of peptides - calculated on the basis of Hα, Cα and Cβ chemical shifts – showed that the peptides are mostly disordered but have some α-helical propensity in solution. The WT peptide had up to 10% α-helical propensity, whereas the S90N and p-S90 showed slightly

higher, ~20% propensity. Predicted structures based on SSP scores show helix formation covering the 92-FENEFF-96 region in all the three peptides, but depending on the residue at 90, the conformation of the structural ensembles varied in other regions (e.g. N/SP motif (yellow) on Figure 26A).

To further examine the role of the residue at position 90, we tested the binding of phosphomimetic mutants to p38 upon specific activation of p38 in HEK293T cells (Figure 26B). The

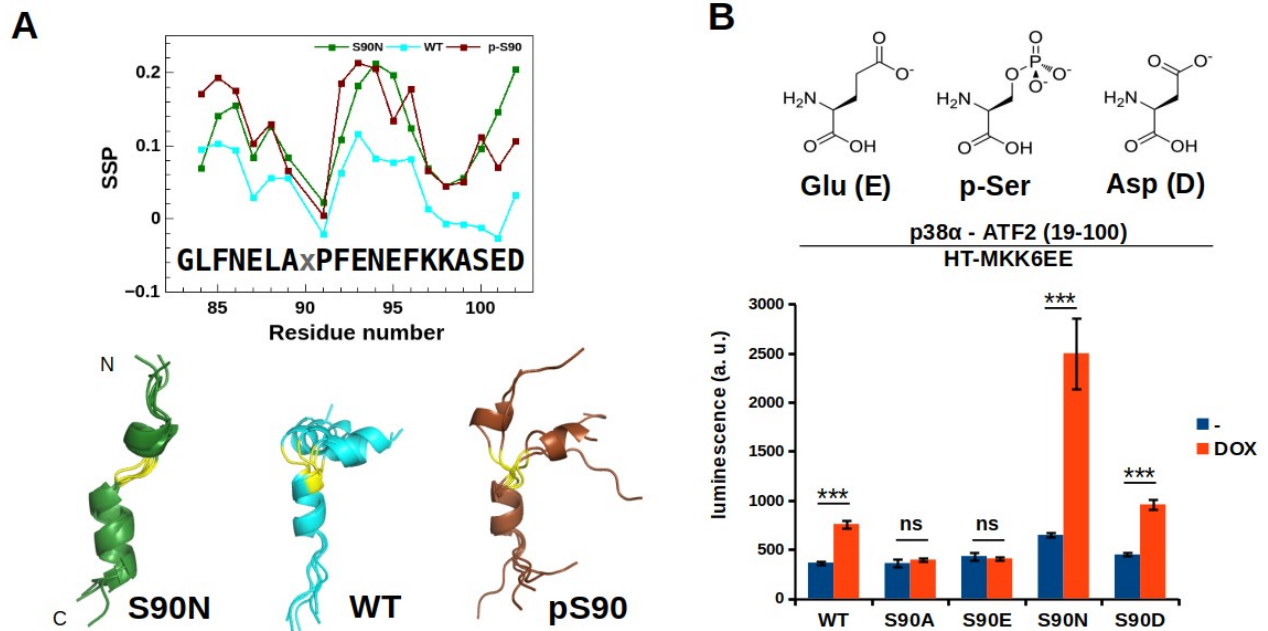


Figure 26 Effect of mutations in the 90. position of ATF2. (A) Secondary structure propensities (SSP) of ATF2(83-102) SPFENEFF peptides (S90N, WT and pS90) in solution. The lower panels display representatives of the 10 lowest-energy NMR structures calculated for the different SPFENEFF peptides. The region corresponding to the N/SP motif is colored yellow. (B) Analysis of phosphomimetic mutations in NanoBit protein-protein interaction assay with tagged ATF2-TAD and p38 α in HT-MKK6EE cell line. Error bars show SD (n=3). Statistical significance was calculated by two-sided, unpaired Student's t-test (NS: not significant; ***: $p \leq 0.001$). Experiments were repeated at least two times with similar results.

glutamate mutant with similar length side chain to phospho-serine had no binding to pp-p38, but the shorter S90D (the most similar to asparagine) showed phosphorylation dependent binding. The S90A mutant was not capable of interacting with pp-p38. These findings are in good agreement with the N-cap preference in alpha-helices analyzed from protein structures, where the most favorable was found to be the 'NP' motif [147]. The switch-like behavior of phosphorylation on the S/TP motif was examined in several studies, but the structural consequences depend on many factors and thus the effect cannot be bioinformatically predicted. For instance, a presence of a charged group in the surrounding sequence can alter the phospho-cap behaviour for helices, moreover the Ser/Thr phosphorylation -

independent of adjacent amino acids - was suggested to modulate the preferred backbone dihedral angles [148].

Our analysis shows that the proper positioning of the two phenylalanine residues in the tight FRS groove edged by W197 highly depends on the chemical nature of the 90. amino acid. These results indicate that the determining factors for binding is not only the charge but also the helix capping capability and conformation by N-terminal region of the helix.

4.2.3.3 HADDOCK model of the bipartite interaction of ATF2 and pp-p38

To model the full ATF2 transactivation domain (WT-ATF2-TAD) binding to pp-p38 we used HADDOCK driven by NMR spectroscopy based titration data and mutational data from biochemical experiments. First we compared the 2D [1H,15N] TROSY spectra of (2H,15N)-labeled pp-p38 when titrated with WT or the S90N SPFENEFF peptides (ATF2 83-102). We found that a great number of pp-p38 resonances showed significant intensity changes and these were similar for WT and S90N peptides, but peak intensities decreased more in the presence of S90N peptide, quantified at 1:4 pp-p38:ATF2 ratio (data not shown). As expected np-p38 did not show any major changes (Appendix Figure 2C). Based on previously determined sequence-specific backbone assignment of pp-p38 we were able to show that residues at FRS of pp-p38 displayed intensity changes in the presence of S/NPFENEFF peptides [118]

Those resonances with more than 50% of intensity loss at 1:4 (pp-p38:ATF2) ratio were used as ambiguous restraints for pp-38 in HADDOCK docking. The input structure for SPFENEFF peptide was derived from the NPFENEFF-pp-p38 crystal structure, and F92 and F96 were used as ambiguous restraints to drive the docking. The Zn-finger+D-motif region was docked into the DRS of pp-p38 using unambiguous distance restraints for the hydrophobic motif. To model the potential formation of a Michealis-Menten complex, we docked the TPTP phosphoswitch region at the MAPK active site with unambiguous restraints based on DYRK1A-substrate complex. After docking, the three interacting ATF2 region were stitched together by MODELLER.

The HADDOCK model of the pp-p38:ATF2(TAD) showed that phosphoswitch (69-TPTP-72) binding at the active site is compatible with the bipartite binding of the TAD at the DRS and the FRS (Error: Reference source not found). According to the model, the wild-type SPFENEFF peptide binds the FRS in a similar manner as the asparagine mutant in the crystal structure. Apart from direct contacts between pp-p38 and the SPFENEFF motif, the model suggests helix capping interactions that stabilize the α -helical conformation of α 2L14, α G, and the ATF2 helix itself by involving E93, E95 or the S90 side-chains. Moreover, the HADDOCK model confirms that phosphorylation at S90 sterically blocks the binding interface, which may not be compatible with the bound conformation of the negatively

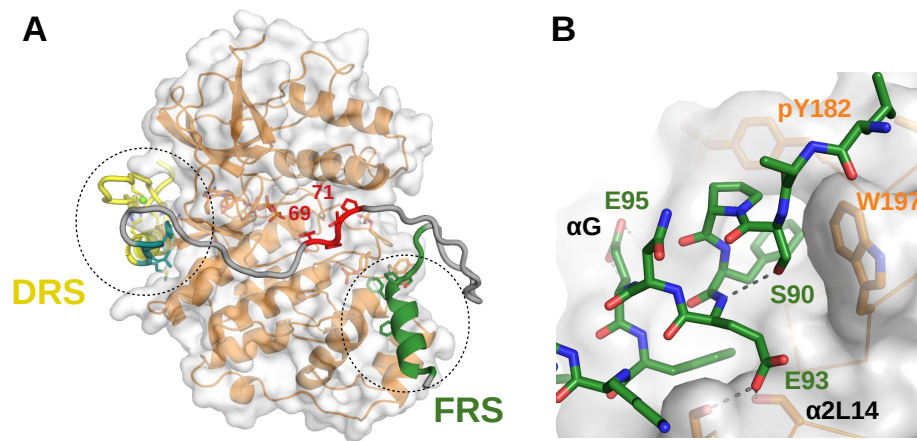


Figure 27 Structural model of the pp-p38+WT-ATF2(TAD) complex. (A) The HADDOCK model was generated by using restraints derived from NMR titration data or crystal structures to drive the docking of Zinc-finger+D-motif (yellow+cyan) and substrate peptide (T69 as the target site, red) and SPFENEFF motif (green) to pp-p38. The missing regions (grey) were modelled by MODELLER. (B) S90 caps the ATF2 helix and the two glutamate side-chains (E93 and E95) cap α 2L14 and α G (hydrogen bonds are shown with dashed lines.)

charged E93, in addition to affecting the conformation of the unbound peptide, as shown before.

4.2.4 Specificity determining factors of ATF2 phosphorylation among MAPK-s

The HADDOCK model of pp-38+ATF2 explained why mutations at either of these regions (e.g. K48E and MUT4 constructs, see Figure 22A) decreased phosphorylation.

To further assess the role of SPFENEFF motif and the Zinc-finger on the phosphorylation by MAPKs regarding specificity in particular, we tested S90N and CACA (Zn-coordinating cysteines) mutants with in solution enzyme kinetic assays using the anti-pp-T69/T71 antibody (Figure 28A). The

S90N mutant did not have effect on ATF2 phosphorylation by pp-JNK, but the CACA mutation negatively effected it. As expected from our earlier experiments, S90N mutation in the FENEF helix cap promotes ATF2 activation by pp-p38, but unexpectedly the CACA zing-finger mutations also increased it. This latter suggests that p38 may prefer a different, possibly an extended conformation of the ATF2 D-motif (45-HKHKHEMTLKF-55), where, in addition to K48, another lysine (K46) could bind to the CD groove of p38. Although K46 lysine is facing towards the solution in the JNK-ATF2 crystal structure and is not involved in JNK binding but its role in p38 binding may explain why ATF2 can be effectively used as a pp-p38 substrate even in the presence of EDTA or DTT in the storage or reaction buffer in vitro (for example, as in the case of commercially available ATF2-protein from Cell Signaling #9224). Albeit this also questions the accuracy of several kinetic studies from the literature.

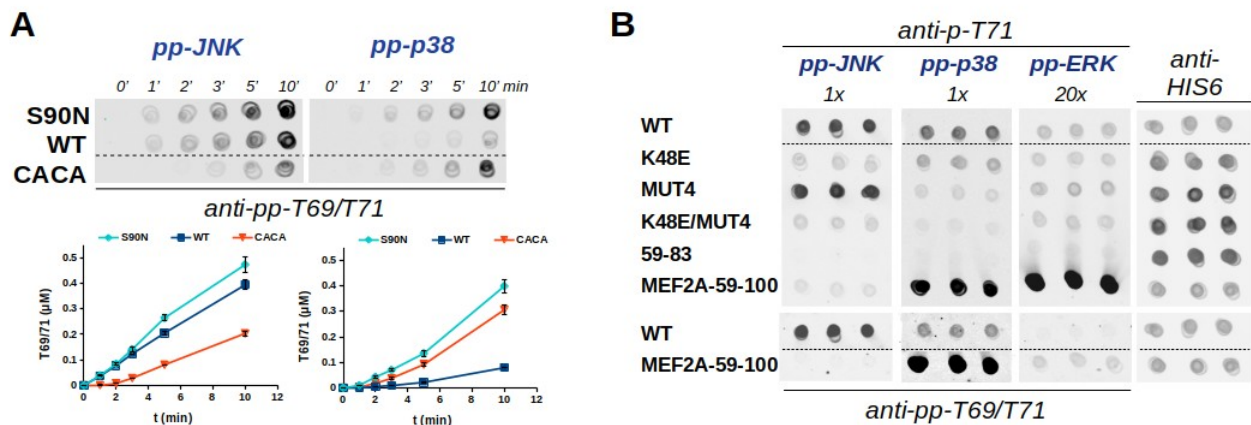


Figure 28 ATF2 phosphoswith phosphorylation with in vitro kinase assays. (A) In vitro characterization of ATF2 TAD S90N and CACA mutants. Kinase assays were performed with 2 nM pp-JNK1 or 2 nM pp-p38 and 2 μM MBP-ATF2(19-100) constructs. ATF2 TAD phosphorylation was detected by using anti-phosphoT69/71 antibody. Error bars indicate SD form (n=3). (B) Equal amount of MBP-ATF2(19-100) mutants were dried on nitrocellulose membrane, then incubated with ~1 pM of pp-JNK, pp-p38 and ~20 pM pp-ERK2 in kinase buffer for 5 min. The immuno-blots were developed with the indicated antibodies.

ERK2 MAPK had also been described as an ATF2 activator [149]. We tested pp-ERK2, pp-p38 and pp-JNK in phosphorylation assays with different ATF2 mutants (Figure 28B). To get acceptable signal to noise ratio with the phopho-specific antibodies in our experimental set-up, we had to use 20x pp-ERK2 in the reaction compared to pp-JNK or pp-p38. Interestingly, ATF2 phosphorylation by ERK2 was not affected by K48E or MUT4 mutations. Using the MEF2A-59-100 construct - where the ATF2 Zn-finger + D-motif module was replaced by an ERK and p38 selective D-motif, strong T71 phosphorylation was detected by pp-ERK2. Intriguingly, in contrast to p38, the enhanced

phosphorylation of this construct could not be detected using the anti-pp-T69/T71 antibody. In agreement with other studies, our results suggest that ERK2 can only phosphorylate T71, but not T69, but the underlying biochemical explanation is unsolved [145]. Altogether we can state that because of the lack of an ERK2 specific binding motif in ATF2, ERK2 is a very weak activator of ATF2, and it is not able to phosphorylate both sites needed for transcriptional activity.

4.3 Co-regulation of ATF2 activity by JNK and p38.

4.3.1 Transcriptional activation by two MAPKs

We showed that JNK and p38 bind to the ATF2 TAD through specific regions. To specifically address the role of these two MAPKs in a biologically relevant function of ATF2, we examined the ATF2-TAD mediated transcription with a luciferase reporter assay. The wild-type TAD and different binding site mutants were expressed as fusion proteins with the GAL4 DNA binding domain and the capacity to activate GAL4 DNA binding based transcription were tested in HEK293T cells. In agreement to the results of *in vitro* or cell-based binding experiments, all mutant with reduced binding capacity (both in the Zn-finger+D-motif or in the SPFENE motif) showed decreased basal transcription from a luciferase expression based reporter vector (Figure 29A). Furthermore, the S90N variant from invertebrates showed significantly elevated level of luciferase activity. In agreement with previous studies, we found that the phosphorylation site mutant S90A decreased the basal activity of GAL4-ATF2 on GAL4 promoter, but the essential contributor for the ATF2 transcriptional activity is the phosphoswitch comprised of the two threonine residue, T69 and T71 (see TATA mutant) [73]. To this day, we do not know the exact molecular mechanism underlying the recognition of pp-TPTP by transcriptional effector molecules, so we cannot exclude the possibility that mutations in other regions of ATF2-TAD also effects the binding to effector molecules - besides of MAPK binding.

We also examined the effect of increased or decreased level of JNK or p38 activity on ATF2 TAD mediated transcription. Basal transcription from the reporter vector was increased by heterologous

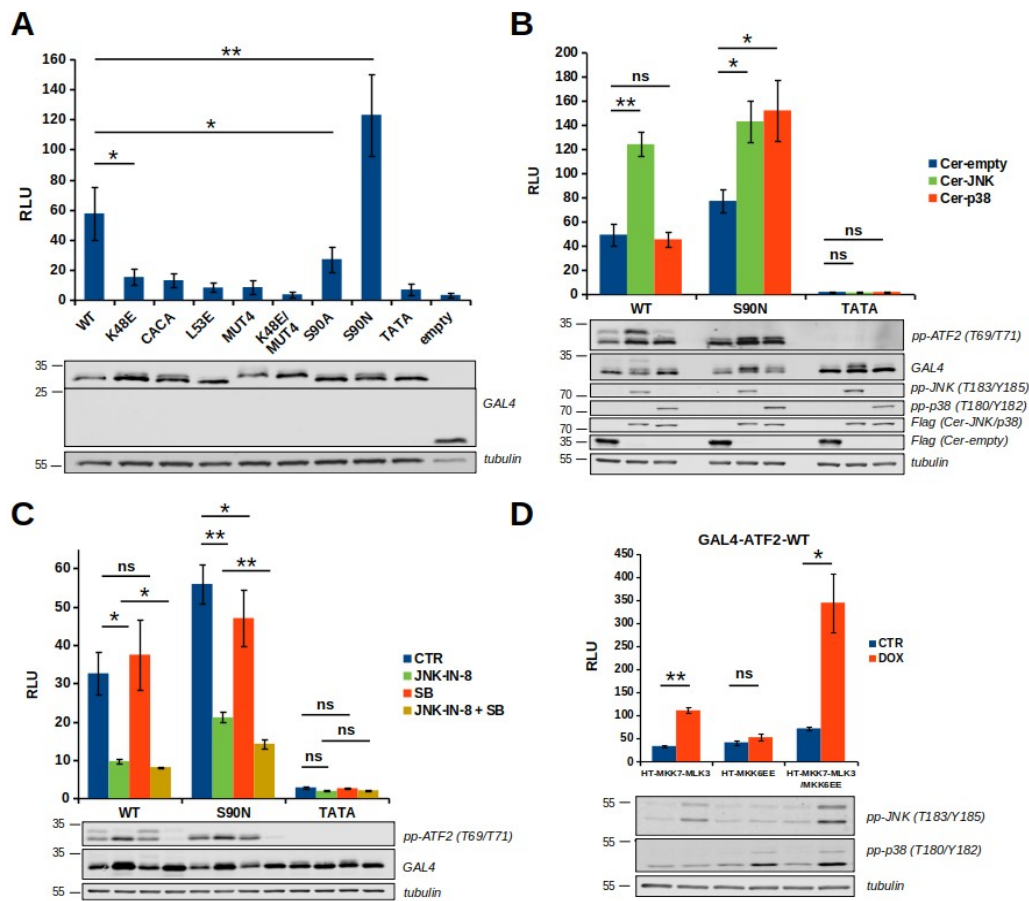


Figure 29 Regulation of ATF2 TAD mediated transcription by JNK and p38 α . (A) Luciferase activity in HEK293T cells were measured after transfection with a GAL4-luciferase reporter plasmid and GAL4-ATF2-(19-100) fusion expression constructs or empty GAL4 construct. (B) GAL4-ATF2-(19-100)-WT, -S90N and -TATA constructs were co-transfected with Cerulean-empty-FLAG (Cer-empty), Cerulean-JNK1-FLAG (Cer-JNK) or Cerulean-p38 α -FLAG (Cer-p38) expression plasmids and luciferase activity was determined. (C) Relative luminescence was measured after treating cells with 1 μ M JNK inhibitor (JNK-IN-8), 1 μ M p38 inhibitor (SB, SB202190) or both inhibitors (JNK-IN-8 + SB), while 0.1% DMSO solvent was used as control (CTR) (D) HEK293T Tet-on (HT) cell lines for inducible expression of MKK7-MLK3, MKK6-EE or both (MKK7-MLK3/MKK6-EE) were transfected with GAL4-ATF2-(19-100)-WT. Endogenous MAPKs (JNK, p38 or both) were switched on by adding doxycycline (DOX). CTR - control, no DOX treatment. (A-D) RLU = Relative Luminescence Unit. Error bars show SD calculated based on 3 biological replicates. NS: not significant; *: $p \leq 0.05$, **: $p \leq 0.01$; paired t-test, two-sided. Western-blot results: phosphorylation level of ATF2, JNK and p38 were detected by phospho-specific antibodies, similar expression of different constructs were confirmed by using anti-GAL4 or anti-FLAG antibodies and anti-tubulin antibody was used as load control.

expression of JNK1 or p38 α and decreased in the presence of JNK- or p38-specific inhibitors (JNK-IN-8 or SB202190, respectively), but the impact of p38 was only apparent in the case of the S90N construct (Figure 29B and C). To support our findings, we also followed the phosphorylation level of transfected ATF2 on T69/T71 with western blot. The results indicate that the upper band on the pp-ATF2(T69/71) blot is also phosphorylated on S90, since it was not visible in the case of JNK-IN-8 treatment or for the S90N mutant. GAL4 reporter assay together with the western blot data suggest that Ser90 phosphorylation by JNK on WT-ATF2-TAD limits p38-mediated transcriptional activation. Nevertheless, the pp-ATF2(T69/71) signal only disappeared upon co-treatment with JNK and p38 inhibitors, therefore we hypothesize that JNK and p38 have a complementary role in the maintenance of basal ATF2 activity.

Next, we examined the ATF2 TAD in the HT-MLK3-MKK7 cell line after turning on JNK activity, or in HT-MKK6EE after inducing p38, or in the HT-MKK7-MLK3/MKK6EE cell line allowing double activation of JNK and p38 at the same time. These engineered HEK293T cell lines allowed us a controlled and highly specific induction of endogenous MAPKs (Figure 29D). While the activation of JNK significantly increased the trans-activation activity of ATF2-TAD, p38 induction did not cause a significant change from the basal activity in this experimental setup. However, measurements in the double cell line (HT-MKK7-MLK3/MKK6EE) indicated that under these conditions JNK and p38 mediated activation of the ATF2 TAD can be synergistic.

In summary, in these experiments, which lacked the drawback of cross-activation of both MAPK pathways by unspecific stimuli (e.g. anisomycin or UV radiation), we demonstrated the both JNK and p38 contribute to the activation of the ATF2 phosphoswitch, and our data also suggest that the invertebrate S90N ATF2 trans-activation activity is more responsive to p38 activity than the vertebrate one.

4.3.2 Quantitative modeling of MAPK mediated ATF2 TAD phosphorylation

To better understand the importance of the co-regulation of ATF2 phosphorylation by two kinases, we performed *in silico* modeling to compare the activation pattern of the vertebrate and invertebrate ATF2.

To simulate the level of phosphorylated ATF2 in response to different upstream fluxes of JNK/p38 pathways, we created a rule-based mechanistic model in the BioNetGen framework (Figure 30A, Appendix Code and Appendix Table 2). JNK and p38 bound to their respective TAD regions, their activated form phosphorylated the T69/T71 phosphoswitch, and pp-JNK also phosphorylated S90. Binding and phosphorylation rates were determined in enzymatic kinetic assays *in vitro* (Figure 11).

The model also included binding rules for D-motif-DRS and F-motif-FRS interaction (e.g. F-motif can only bind the double-phosphorylated form of p38 and when the S90 site is non-phosphorylated). Proteins are dynamically phosphorylated by protein kinases and dephosphorylated by phosphatases in the cell, and this reversible modification plays a key role in biological regulation. Therefore, the model also included upstream kinases for MAPKs and deactivating phosphatases for MAPKs and ATF2 and their action were modeled as first order reaction. In order to keep the number of parameters low, we used a simplified model to implement MAPK activation and dephosphorylation where MAPKs had only two states: an un-phosphorylated inactive and a double-phosphorylated “active”. MAPKs were activated by upstream kinases (k6 or k7) and deactivated by phosphatases (dp1 and dp2) when its binding surface are free, because these enzymes are known to bind to the same surface on MAPKs as the substrates (e.g. ATF2), therefore their binding is mutually exclusive [44]. ATF2 phosphorylation was counteracted by phosphatases, acted on T69/T71 or S90 phosphorylation sites (dp3 and dp4). Upstream kinase and phosphatase reaction rates were adjusted based on the response of HEK293T cells to anisomycin treatment (Figure 30B). Anisomycin stimulation was imitated by increasing k6 and k7 activity ($k_{eq6} \rightarrow k_{stim6}$, $k_{eq7} \rightarrow k_{stim7}$) in the model. Anisomycin stimulation experiments were carried out with wild-type, S90N, and MUT4 ATF2 constructs in the absence or presence of a JNK-IN-8 inhibitor and the p38-ATF2 dynamic interaction reporter (i.e. NanoBiT signal in live cells), MAPK and ATF2 phosphorylation (by Western-blot) were concomitantly monitored in time for 40 minutes.

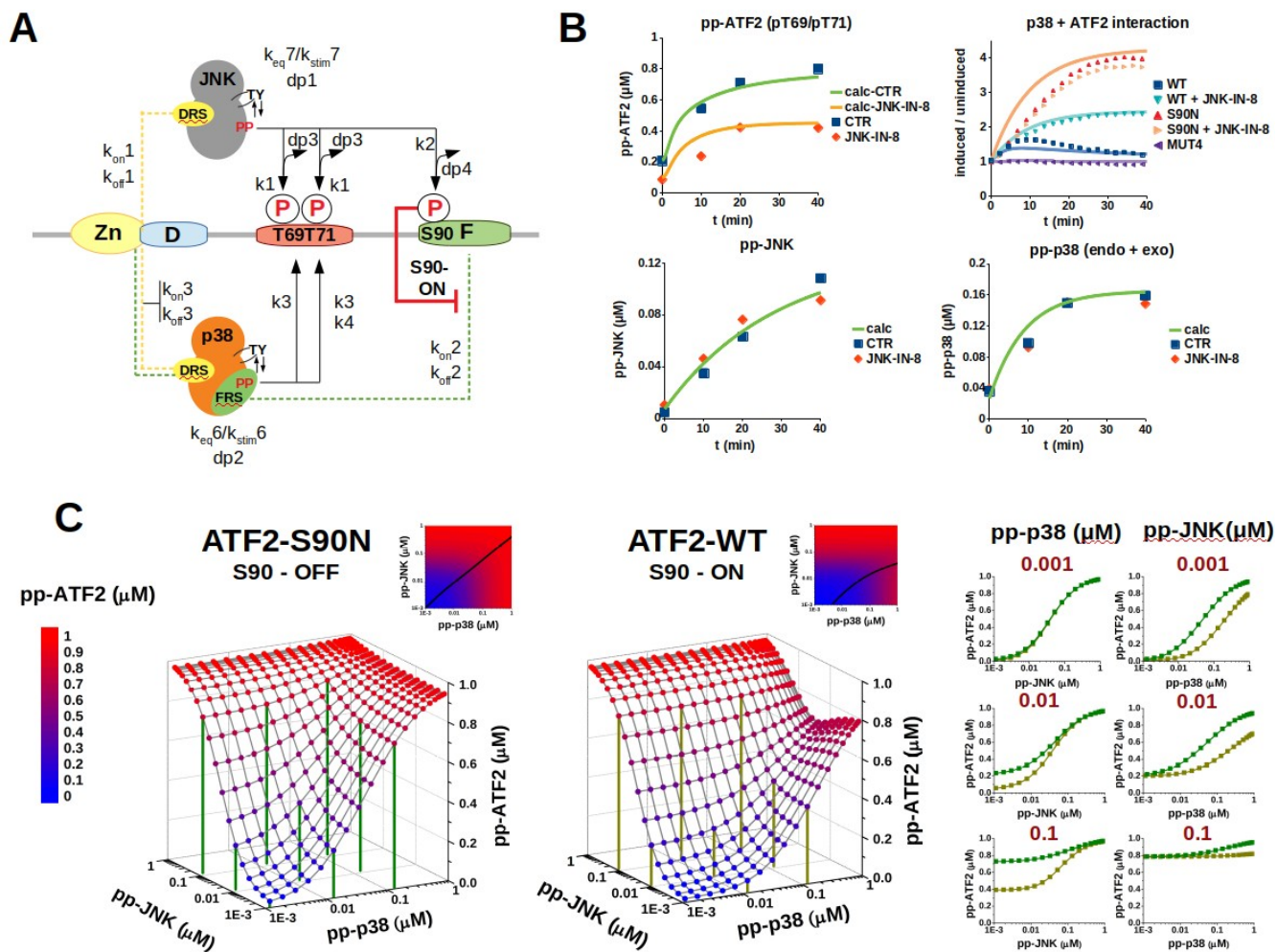


Figure 30 Mechanistic modeling ATF2 TAD phosphorylation under various JNK/p38 MAPK fluxes. (A) Mechanistic scheme of MAPK mediated ATF2 TAD phosphorylation. The panel shows the architecture of the rule-based BioNetGen model. Dashed lines represent binding rules (k_{on} , k_{off}) and arrows indicate enzymatic reactions of kinases (k) and phosphatases (dp). Phosphorylation in S90 inhibit bipartite pp-p38 binding. (B) Parameters for phosphatases and k_6 and k_7 kinases were determined by anisomycin stimulation of HEK293T cells and pp-JNK, pp-p38 and pp-ATF2-T69/T71 was monitored in Western-blot. The parallel p38-ATF2 NanoBiT assay signal was also used to adjust the parameters (dots: measured data points, contiguous line: simulated data after fitting). (C) Simulated ATF2 TAD phosphorylation levels 40 minutes after stimulation by k_{stim6} and k_{stim7} (evenly distributed from 10^{-6} to 10^{-2} in the logarithmic scale). 3D plots show ATF2 TAD phosphorylation as the function of different amounts of pp-p38 and pp-JNK where the total in-cell MAPK and ATF2 concentrations were set to $1 \mu\text{M}$ for each protein. 2D panels show projections of the corresponding 3D plots. Black line indicates where pp-ATF2 level is equally sensitive to the activation of both MAPKs. Graphs on the left correspond to slices from the 3D graphs at given pp-MAPK concentration (green: S90N, gold: WT).

The mechanistic model was then used to calculate the in-cell phosphorylation level of the WT and S90N ATF2 T69/T71 phosphoswitch (pp-ATF2) under varying amounts of activated p38 and JNK

levels (Figure 30C). For ATF2-S90N, the S90 regulation is OFF as this site cannot be modified by JNK and MAPK effects are additive towards building up high levels of pp-ATF2. The inflection point is $\sim 5\%$ of the total flux for both MAPKs, which is more visible in the contour plot (left panel next to S90N 3D plot) Figure 30C). In contrast, the 3D response surface is more complex with the ATF2 WT protein (where S90 is ON and can be phosphorylated by JNK), and the difference is also visible in the contour plot with a black characteristic curve (Figure 30C, middle panels). The region above this line corresponds to the area where pp-ATF2 is more sensitive to JNK activity, while the region below the line is more sensitive to changes in p38 pathway flux. In general pp-ATF2 levels are more sensitive to JNK activity compared to p38 pathway flux. Graphs indicate that WT pp-ATF2 level stays low in response to low-to-medium p38 flux even under small amounts of JNK pathway flux, and has increased 2D dynamic range (the inflection point is $\sim 25\%$). Increasing JNK flux under high pp-p38 levels can bring about maximum pp-ATF2 output only after going through a local minimum or threshold, which is a unique feature for WT-ATF2. The two systems (S90N vs. WT) can also be compared in 2D graphs which are the projections of the 3D response surface at indicated MAPK concentrations (Figure 30C left panels). At low pp-p38 concentration, the two systems are similarly responsive to pp-JNK, but the sensitivity to JNK at 10% of p38 activity is apparent only in the case of WT ATF2. Compared the vertebrate WT system, the invertebrate S90N is more sensitive to pp-38 at different pp-JNK levels.

Together with the evolutionary analysis, mechanistic modeling suggests that the system may have been evolving from pp-38 responsiveness towards pp-JNK responsiveness.

To further examine the system, we were curious about how these ATF2 binding parameters affect ATF2 phosphorylation. The parameters for WT ATF2(TAD)-JNK(DRS), -p38(FRS), and -p38(DRS) binding were changed to simulate three distinct scenarios (Figure 31). 1) JNK binds to Zn-finger+D-motif module 100-fold stronger (which could be achieved by increasing the k_{on} or decreasing the k_{off} of the interaction). 2) p38 binds to the SPFENEF motif 100-fold stronger. 3) p38 binds with 10-fold stronger to the Zn-finger+D-motif (k_{on3}), thus affecting the bipartite interaction also (k_{on2}), and JNK binds with 10-fold weaker affinity. The third case would be analogous to the MEF2A-ATF2-(59-100) construct where the ATF2 Zn-finger+D-motif was changed to a p38 specific docking motif (see Figure 28B). In the first and second case, pp-ATF2 levels were less responsive or oversensitive to p38 activity, respectively, and in the third case, pp-ATF2 was more specific to p38 and less responsive to JNK activation. Changing the k_{off} -s to have the same binding affinities gave similar results. Altogether

the three modified model show that arbitrarily changing the binding affinities may result in a less complex response to various JNK and p38 fluxes compared to WT ATF2 at the given catalytic rates.

In conclusion, our model showed that the MAPK binding affinity and the specificity of ATF2 TAD regions are set in vertebrates so that to allow graded phosphoswitch activation under broad p38/JNK pathway activity in the cell.

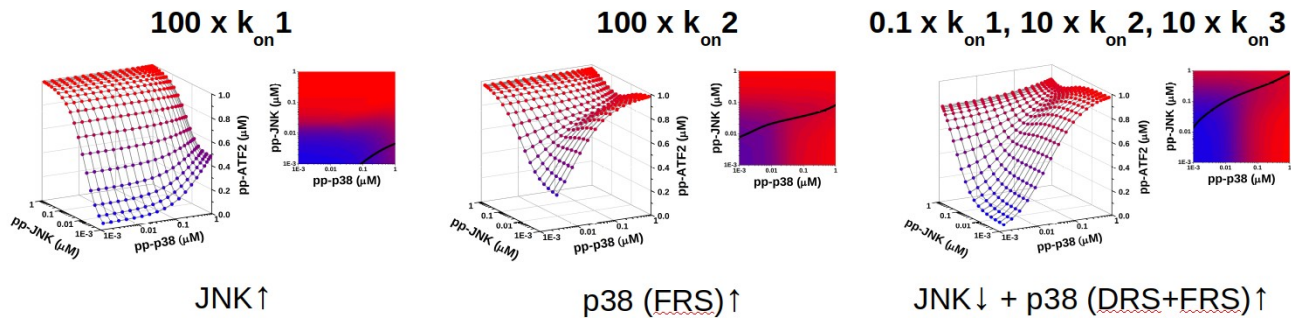


Figure 31 The impact of MAPK binding affinity and specificity of ATF2 on pp-ATF2 levels. JNK-ATF2 or p38-ATF2 binding affinities were arbitrarily changed in the model and pp-ATF2 level was simulated.

4.4 D-motif mediated interaction of JNK and DCX

DCX is a known mediator of JNK pathway in neural cells, and the molecular interaction between the two protein is not well-understood. With the bioinformatics pipeline of Zeke et al. (2015), we predicted a D-motif in the DCX-C-terminus satisfying the NFAT4-type and MEF2A-type class. According to genomic and proteomic databases, DCX expresses as multiple isoforms in the brain affecting the C-terminal region of the protein. In human, 4 different main isoforms are described (1-366, del348V, del311-315 and del311-315/del348V). The del348V - the canonical isoform in Uniprot database - has mutation in crucial position in the D-motif consensus. Several research groups work with the longer 366 amino acid isoform, and we also obtained this splice variant from our collaborator (Bogoyevitch group, University of Melbourne). DCX with tandem DC domains is only represented in vertebrates and alignment of different species from human to fish showed conservation covering the JNK dependent phosphorylation sites, together with the essential residues of the docking motif [108]. Interestingly, the aspartate rich C-terminus is also highly conserved. (Figure 32A, lower panel).

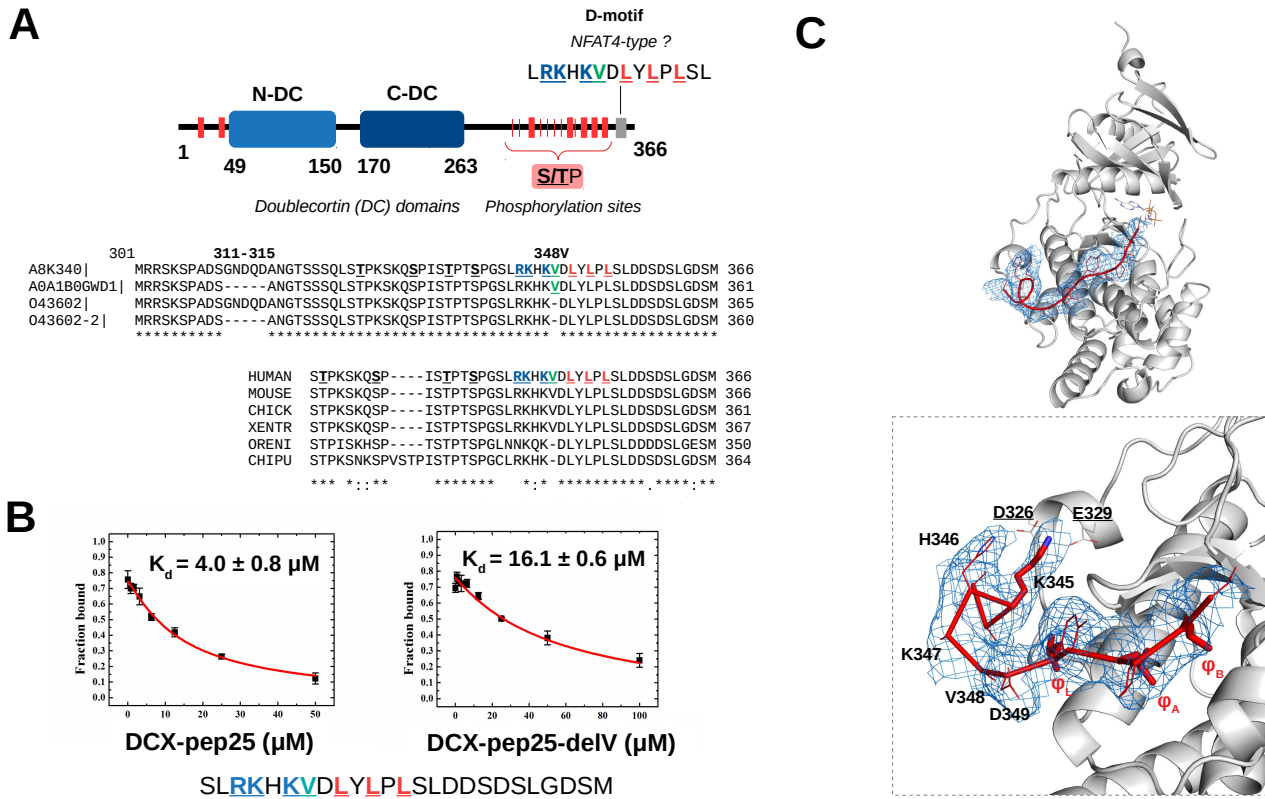


Figure 32 Docking motif in the DCX C-terminus. A) A sequence resembles to NFAT4-type D-motif is located between the phosphorylation sites and C-terminus. Human DCX isoforms are aligned in the middle. JNK dependent phosphorylation sites are shown in bold, while basic and hydrophobic residues are colored with blue and red. Note, that V348 (in green) is not present in all isoform. Evolutionary conservation of DCX C-terminus were examined in *Homo sapiens* (HUMAN), *Mus musculus* (MOUSE), *Gallus gallus* (CHICK), *Xenopus tropicalis* (XENTR), *Oreochromis niloticus* (ORENI), *Chyloscyllium punctatum* (CHIPU). B) Fluorescence polarization assay were performed with JNK1 and CF-evJIP, and chemically synthesized DCX peptides (pep25 and V348 deletion mutant pep25delV) were used as competitor. C) Crystal structure of DCX-pep25 bound to JNK1 at 3.5 Å. The simulated annealing Fo-Fc OMIT map contoured at 1.5 σ shows that the DCX peptide occupies the JNK DRS.

To experimentally verify the C-terminal docking sequence, we synthesized a short peptide (SLRKHKVDLYLPLSL) and examined its binding to MAPK kinases. Fluorescence polarization measurements indicated JNK specificity (JNK1: $K_d = 16.7 \mu\text{M}$, p38 α : $K_d = 29.5 \mu\text{M}$, ERK2: $K_d = 59 \mu\text{M}$, included in Zeke et al (2015)). Next we included the C-terminal negatively charged region to the sequence (DCX-pep25), because of the limited water solubility of the short peptide. Additionally, we wanted to know the effect of the V348 deletion on the JNK binding affinity. The wild type DCX-pep25 bound to JNK with $K_d \sim 4 \mu\text{M}$, 4x stronger than the delV variant (Figure 32B).

To address the role of V348 and the possible contribution of the conserved C-terminal acidic sequence on the binding, we attempted to crystallize the JNK-DCX_{pep25} complex. We were able to crystallize and solve the structure at 3.5 Å resolution. In this structure, the asymmetric unit consists of 3 JNK-DCX_{pep25} complexes, and the peptide binds to the JNK DRS similarly in all cases (Figure 32C). The hydrophobic leucines occupy the hydrophobic pockets as in the NFAT4-JNK structure. The clear backbone electron density suggests that the region covering 344-348 forms a short helix. Simulated annealing Fo-Fc OMIT map shows density of K345 side chain in 2 cases from the 3 complex at 1.5 σ . K345 makes contact with the CD groove. K347 would be in the analogous position for the important NFAT4-type basic residue. However, in the JNK-DCX crystal structure this residue is facing the solution because of the different helix formation compared to JNK-NFAT4 structure. The acidic C-terminal region of the peptide is not visible in the new structure, indicating that this region does not undergo disorder-to-order conversion and might not be directly involved in binding.

To further elucidate how JNK1 recognizes DCX, we performed experiments with full-length DCX including the doublecortin domains that were proposed to be important for binding ([103]). MBP-pulldown experiments with WT and truncated forms of DCX showed that the JNK binding is highly depends on the D-motif (Figure 33A and B). Complex formation of DCX with JNK only required the C-terminal docking sequence examined by analytical size-exclusion chromatography (Figure 33C). Nonetheless, it cannot be ruled out that a weak interaction of DC domain-JNK exists.

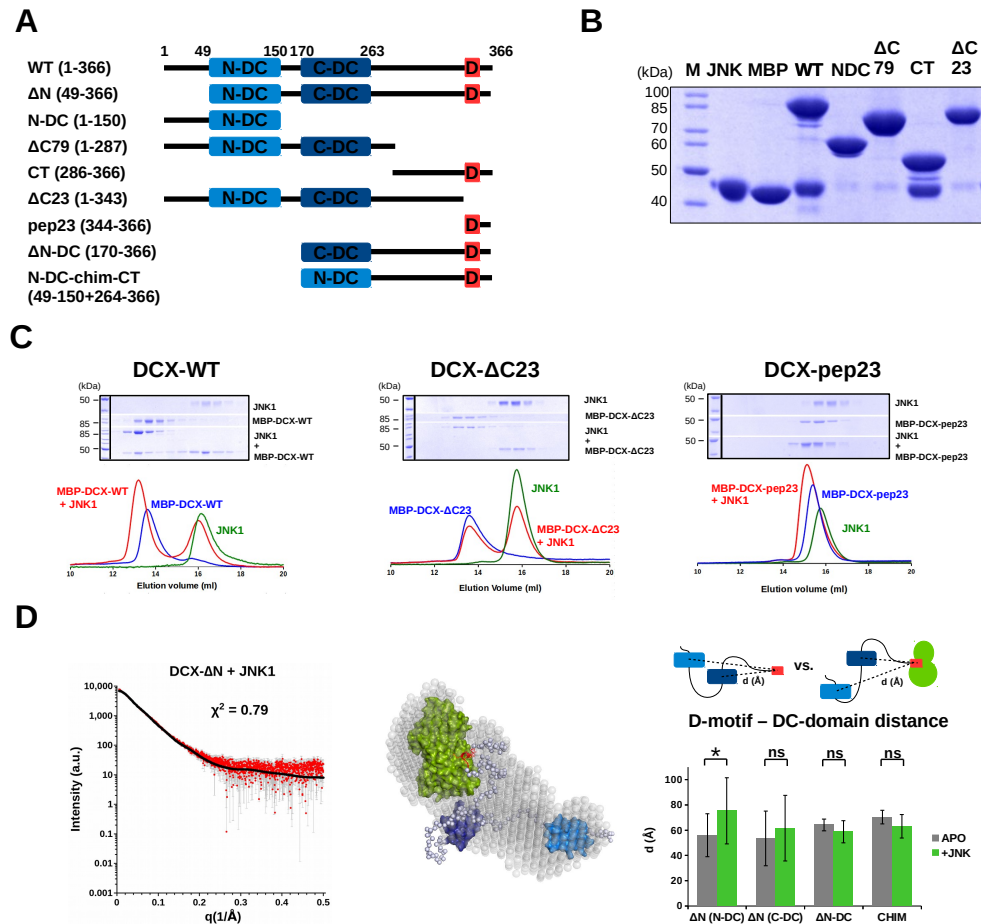


Figure 33 JNK1-DCX interaction is D-motif dependent. (A) MBP or GST tagged DCX constructs used in the study.

(B) MBP pull-down experiment with JNK1 (prey) and various MBP-DCX constructs as bait. Interaction of recombinantly expressed and purified bait and prey was detected on Coomassie stained SDS-PAGE. MBP control was used as negative control to assess unspecific binding of the prey (MBP; M – Molecular weight marker, JNK – load). (C) Analytical gel filtration experiments of MBP tagged DCX-WT and DCX-ΔC23 and MBP-pep23 constructs with JNK1. Coomassie stained SDS-PAGE gels were run from the corresponding fractions from the chromatogram (Y axis: absorbance at 280 nm (a.u.)) (D) SAXS analysis were performed with DCX-ΔN + JNK1 complex and 10 independent CORAL model were generated using previously determined crystal structures and appropriate linker length. Ensemble of CORAL models generated by GAJOE and its theoretical scattering curve is shown in the scattering graph. Dummy atom model was generated by DAMMIN and the best fitted CORAL model ($\chi^2=0.81$) was superposed against the DAMMIN model. SAXS analysis were performed with apo-DCX constructs (ΔN , ΔN -DC and N-DC-chim-CT (CHIM) and in complex with JNK, then D-motif - NDC and D-motif-CDC distances were compared of the apo and complex CORAL models (n=10, Student's *t*-test, unpaired, two-tailed).

As we were not able to crystallize the full-length DCX with JNK, we utilized SAXS measurements to characterize the behavior of the complex. We collected scattering data from apo DCX

and JNK-DCX samples (here the DCX (Δ N) construct did not include the N-terminal unstructured region to facilitate modeling). We generated 10 independent CORAL model to fit the scattering data for each measurement. We wanted to know if the presence of JNK changes the distance between the docking motif and the individual DC domains in the CORAL models. If there were interaction between JNK and one of DC-domain, the distance should be less in the complex models compared to the apo state. We repeated the measurement with constructs including only the N- or C-DC doublecortin domains to simplify modeling. Overall, the shape of the CORAL models and the measured distances indicated that the presence of JNK does not influence the in-solution behavior of DCX. These results suggest that apart from the D-motif no other elements contribute to the binding of JNK1.

To examine the cellular behaviour of the JNK1-DCX complex, we utilized bimolecular fragment complementation assay (BiFC). While the YFP-fragment (F2) tagged JNK1 localized evenly in the cytosol, the YFP fragment (F1) tagged DCX localized to a fibrous structure in HEK293T. It has been described, that DCX co-localizes with microtubules and its overexpression causes microtubule bundling [150]. The BiFC complex of DCX and JNK also localized in a bundled structure. Additionally, we performed experiments in COS-1 cells because of its larger well-spread cytoskeleton. Colocalization of the JNK-DCX BiFC complex with α -tubulin confirmed that the fibrous structures are indeed microtubules (Figure 34B). In the work of Zeke et al (2015) a similar BiFC assay was performed by Alexa Anita with WT and Δ C23 DCX in HEK293T cells. While the expression levels of the two constructs were similar, the YFP signal detected with the mutant DCX-JNK1 complex was significantly lower compared to WT [30]. We performed a parallel experiment with split-luciferase NanoBit reporters that responds dynamically to the interaction and allows detection at much lower expression levels of the tagged proteins. In this experiment the deletion of the D-motif dramatically decreased the luminescence signal (Figure 34C). In the future we are planning to use the dynamic NanoBit system to follow the JNK1-DCX interaction in the SH-SY5Y neural cell line upon different stimuli so that to extend the relevance of these findings in a better biological model.

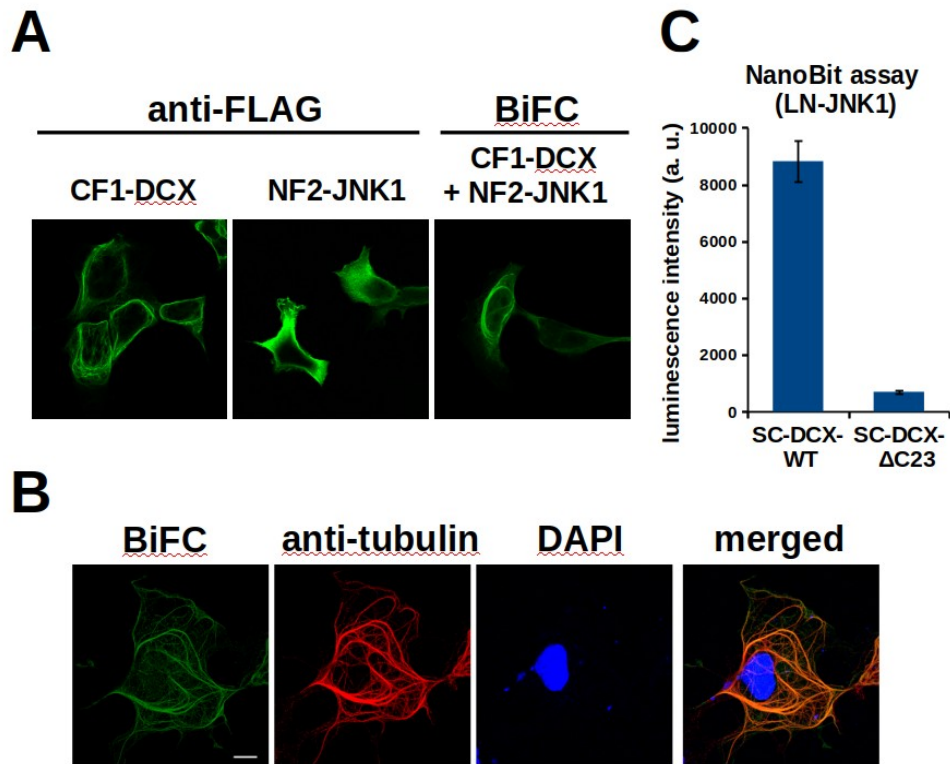


Figure 34 Interaction of DCX with JNK1 in cells. A) HEK293T cells were transfected with FLAG-tagged CF1-DCX, NF2-JNK1 or both and visualised by confocal microscopy. Localization of individual proteins were detected by immunostaining with anti-FLAG antibody and the BiFC signal for the co-transfected cells were detected as YFP fluorescence. B) Co-localization of tubulin and the BiFC complex of CF1-DCX and NF2-JNK1 were examined in COS1 cells. The cells were immunostained with anti-tubulin antibody and the nucleus was stained with DAPI dye (scale bar: 10 μ m). C) NanoBit assay was performed in HEK293T cells to examine the effect of docking motif deletion from DCX on the interaction with JNK1. SD from 3 technical replicates are indicated on the graph. The experiment were repeated independently 3 times with similar result.

Interestingly, the JNK regulated phosphorylation sites are located N-terminally from the D-motif. To address the effect of the D-motif on the phosphorylation of DCX by JNK1, we utilized *in vitro* 32 P incorporation assay (performed by Anita Alexa) and the findings were included in the paper of Zeke et al, (2015). Deletion of 23 amino acids (including D-motif) from the DCX C-terminus caused diminished DCX phosphorylation compared to the wild-type protein. Similarly, addition of a DRS competitor D-motif peptide into the reaction of DCX-WT led to decreased phosphorylation [30]. These results suggest that the overall phosphorylation of DCX by JNK1 depends on the D-motif, but how the unusually placed docking motif facilitates the phosphorylation of the cognate JNK sites is not yet understood.

5. Discussion

5.1 Non-canonical interactions of MAPKs at the DRS and FRS

In our work we unraveled and characterized the interaction of ATF2 transcription factor TAD domain with its upstream activators, the JNK1 and p38 MAP kinases, and studied the interaction of the microtubule binding DCX protein with JNK1.

DCX engages JNK DRS with a D-motif

Our non-canonical interaction candidate, the neuronal migration protein DCX had earlier been predicted to be bound to JNK with one of its microtubule-binding domain [103]. However, we found that the interaction is mediated with its D-motif [30], and we are able to determine the crystal structure of JNK1-DCX D-motif complex. Our cell-based studies also confirmed that JNK-DCX interaction relies on the C-terminal docking motif. Moreover, our data suggest that the presence of JNK does not interfere with DCX's microtubule binding activity, and the DCX-JNK complex is mostly localized on to the microtubules. Based on previous studies, it cannot be ruled out that a third molecule (e.g. JIP-1) is participating in the interaction with the DCX-JNK1 complex in neuronal cells [103]. In addition to its own JNK-dependent phosphorylation sites, DCX might cooperate in the activation of indirect JNK substrates in the cytoskeleton. Neuronal cell line or a mouse model with deletion of the D-motif from the C-terminus (e.g. with CRISPR/CAS9 technology) would give us better understanding of the JNK-dependent role of DCX and also would hint on the importance of JNK recruitment to the microtubules.

Zn-finger dependent interaction of ATF2 with JNK

In the case of ATF2, we presented non-canonical interactions towards both JNK and p38 [151]. We proved that an intact Zn-finger partially overlapping with the D-motif is the minimal JNK binding domain in the ATF2 transactivation domain. Interestingly, similar synergism between a small structured domain (PB1) and D-motif from MKK5 had been described in the unrelated MKK5-ERK5 complex [33]. The MKK5 PB1 domain and D-motif are structurally separated by a short, 2-3 AA linker, with individual binding affinities in the 0.5-5 μ M range. In contrast, in ATF2 the two slightly overlapping regions are indispensable for biologically relevant binding. In addition to making some extra contacts, our ITC analysis suggests that the Zn-finger in ATF2 contributes to the binding energy by decreasing the entropic cost of binding into the JNK DRS. Sterical constraints of a peptide in a bioactive conformation is indeed considered to improve target binding affinity by entropic pre-organization

[152]. Therefore, peptide stapling is an intriguing strategy for alpha-helix mimetic inhibitor design. As an example, the N-terminal linear peptide from the p53 tumor suppressor binds the MDM2 oncoprotein in an α -helical structure. The interaction can be inhibited by a p53 motif mimicking, chemically stapled helical peptide that binds MDM2 $\sim 100\times$ stronger than the original peptide which only had 7% helical propensity in the apo state [153,154].

D-motif-MAPK crystal structures show that various intra-peptide hydrogen bonds contribute to the proper positioning of the charged residues in the CD groove and therefore to their MAPK binding specificity [5]. In the case of ATF2, the alpha-helix of the Zn-finger provides the hydrogen bond staples for the basic residue, similarly as observed in the short helical segment of the JNK-bound NFAT4 peptide (Figure 35B). Even though the ATF2-D-motif confers to a canonical NFAT4-type MAPK binding consensus, it has weak affinity ($\sim 100 \mu\text{M}$) without the Zinc-finger. A large number of known NFAT4-type motifs contains leucine at the ϕ_L and ϕ_B positions but ATF2 has – probable less favorable – M and F at those sites, respectively. Despite of weak binding, the structure of this short ATF2 D-motif (46-56) lacking the Zn-finger bound to JNK was determined by Laughlin et al. (2012) [93]. Although the position of hydrophobic residues are almost identical with our structures, instead of lysine 48, a shorter and less charged histidine faces the CD groove (Figure 35A). This difference further highlights the importance of intra-peptide H-bonds to direct the basic moiety into the negatively charged groove.

Interestingly, the ATF2-CACA construct (in which the Zn-finger structure is disrupted) was phosphorylated by p38 better compared to wild-type while JNK binding decreased (Figure 28). This suggests that the Zn-finger limits the capacity of the partially overlapping D-motif to bind to p38 and favors JNK binding. The ATF2 Zn-finger D-motif module is more JNK-specific compared to D-motif only, and specificity may be achieved through both positive and negative factors that promote JNK- and limit p38-binding, respectively.

In DCX we found a D-motif, which matches the NFAT4 consensus sequence, but surprisingly it binds JNK in a different backbone conformation based on our crystal structure (Figure 35C). Despite that the hydrophobic part of the peptide is identical to NFAT4 (see alignment on Figure 35), DCX has different H-bond staples in the charged region. The basic residue (K345) bound to the CD groove is at a different relative position compared to motifs classified as NFAT4-type. Although we do not have structural data on the del384V peptide, we suspect that this weak binder mutant may adopt a different secondary structure in this region which is energetically less favorable. Our JNK1-pepDCX crystal structure demonstrates that DCX binds to JNK in a new conformation that has not been observed in any

deposited D-motif+DRS structures. However, a higher resolution structure will be needed for the precise demonstration of this particular binding mode.

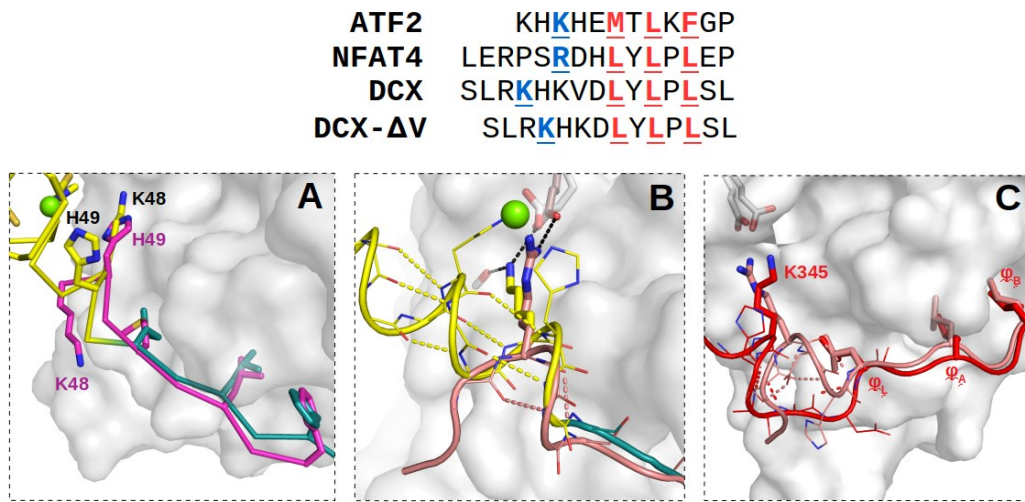


Figure 35 Different binding modes of D-motifs in JNK-DRS. A) Structural comparison of the JNK1-ATF2(19-58) crystal structure with the JNK3-pepATF2 (PDB ID: 4H36, in magenta). Note the incorrect position of K48 and H49 if only a truncated ATF2 D-motif is used for crystallization. B) JNK1 -ATF2(19-58) aligned with the JNK1-pepNFAT4 (PDB ID: 2XRW, in salmon) crystal structure. The panel shows the similarity between the NFAT4 peptide backbone and the alpha-helical region of the Zn-finger domain that holds and orients the positively charged residue towards the CD groove. C) JNK1-pepDCX25 crystal structure (in red) occupies the charged region of DRS differently than the NFAT4 peptide. Intramolecular hydrogen bonds are shown with dashed lines.

S/NPFENEF, a p38 specific F-type motif in ATF2

We described and characterized an F-motif that specifically binds to the FRS of p38, but not to ERK2 or JNK1, for the first time. We found that double-phosphorylated p38 binds ATF2 stronger than non-phosphorylated p38. This observation is similar to how ERK2 binds F-motif peptides (e.g. the FxFP motif from ELK1) [34]. Although ATF2 does not have an FxFP motif, an SPFENEF motif in the TAD found to be critical for pp-p38 binding and also has two phenylalanine residues. Therefore, we posited that the SPFENEF region binds to the FRS, and this was then indeed confirmed by NMR based interface mapping and X-ray crystallography.

The structural basis of FRS binding specificity can be explained by examining the amino acid composition of the particular MAP kinases. From the crystal structure of the pp-p38:ATF2(83-102) complex we could identify the pivotal residues for FRS binding, and evolutionary sequence analysis

suggests that these are highly conserved among p38 α orthologs in *Metazoa* and *Fungi* (see Appendix Figure 3C). Out of the 12 important positions only 3 are identical in other human p38, ERK and JNK sequences (see alignment in Figure 36).

NMR studies and the HADDOCK model of the Elk-1-pp-ERK complex revealed the binding mode of two phenylalanine residues from the linear FxFP motif to the FRS. The position of those phenylalanines seem to be similar to that we described in the S/NPFENEF-pp-p38 interaction, although additional contacts are also engaged in the binding. E184 specific to ERK2 in the activation lip may interact with K392 from the Elk-1 peptide and L393 side chain can make hydrophobic contact with Y231 from α G helix [34]. Importantly, the α EF/ α F loop with Ser 200 (equivalent to W197 in p38) does not appear to make contacts with Elk-1. Moreover, the superimposition of pp-ERK2 and pp-p38 structure suggests that E184 in the ERK2 activation loop could sterically inhibit the binding of the S/NPFENEF peptide (Figure 36).

Due to the lack of a known crystal structure of double-phosphorylated JNK, the orientation of the α EF/ α F loop in the active kinase is not known, but glycine or methionine amino acids at W197 position are unlikely suitable substitutions for stacking the S/N90 in the ATF2 peptide. Crystal structure of JNK in complex with the catalytic domain from MKP7 phosphatase presents an unusual mode of FRS binding. Here, the first phenylalanine from a structured domain is not bound to ϕ 1, but held by the main chain of G199 and M200 of JNK, and hydrogen bond is formed between Q253 side chain and the phenylalanine main chain. A second phenylalanine analogous to F96 sits slightly lower in ϕ 2 than in ATF2 because of the deeper FRS supported from the bottom by a tryptophan at the L232 position (PDB ID:4YR8) [44].

Although mutations on the top of α G helix (H228/I229 to alanine) did not affect ATF2 phosphorylation by pp-p38 according to Tzarum et al. (2013) [127], various rotamers of H/Y are observable in this position in MAPK crystal structures, giving the opportunity to make new contacts with the interaction partner or even to sterically inhibit binding. Apart from 90, 91, 92 and 96 positions, the S/NPFENEF motif shows conservation of an acidic residue at position 93 (Figure 23A, Appendix Figure 3A and B). Crystal structure and HADDOCK model suggest that E93 might interact with S252 which may increase the specificity of ATF2 towards p38.

In summary, MAPK FRS pockets are overall similar, but additional contacts from non-identical residues influence the interaction of FRS with linear motifs or structured domains from MAPK substrates or phosphatases. Clearly, the unique W197 provides the specificity for the ATF2-pp-38

interaction as it supports ATF2 helix stabilization by S/N90. Therefore the phenylalanines of the non-canonical FENEF motif can occupy the FRS as proposed at canonical FxFP motifs. The presented new and specific S/NPFENEF motif gives us the opportunity to find new p38 binding motifs in the proteome and also provides the structural basis for p38-FRS specific small molecule design.

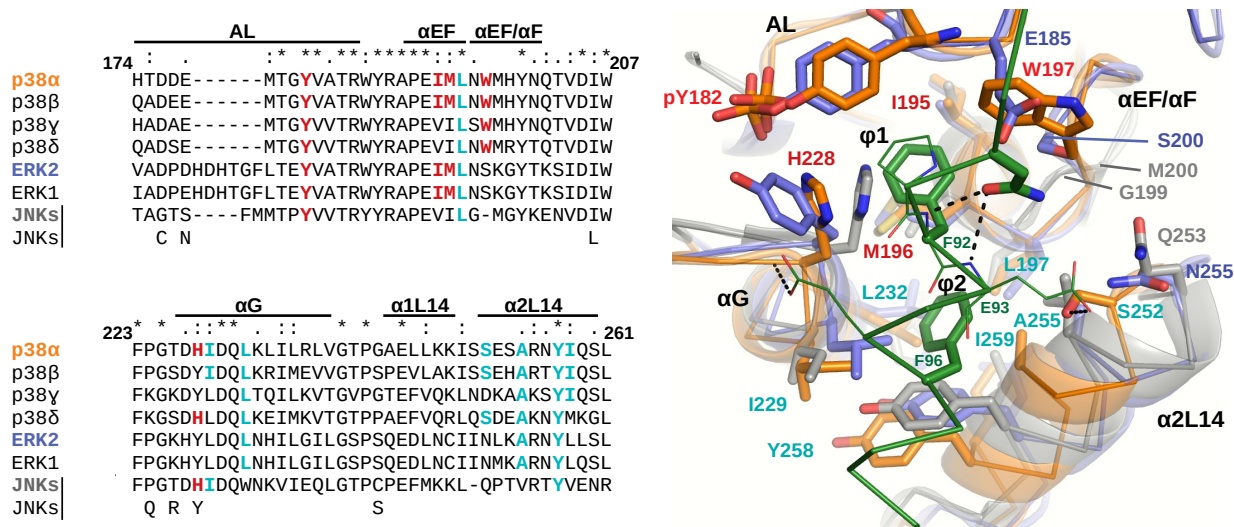


Figure 36 Comparison of the FRS site of p38s, ERKs and JNKs. Human MAP kinase sequences were aligned by Clustal ω . Note that the last row shows sequence variations found in 15 isoforms of JNK1, 2 and 3. Structure of apo pp-ERK2 (blue, PDB ID:2ERK) and JNK extracted from JNK-MKP7 complex (gray, PDB ID:4YR8) were superimposed to pp-p38-NPFENEF structure (orange+green). pp-p38 residues involved in the formation of the upper and lower pocket of the FRS are highlighted with red and cyan, respectively. Residues for ERK and JNK are shown in the structure with blue or gray.

Bioinformatics prediction of non-canonical interaction of MAP-kinases are extremely difficult. As presented in the introduction, the interaction partner may utilize more than one docking region without using a canonical sequence to bind the MAPK. Even in the case of bipartite binding, the affinity can be weaker than a canonical DRS-D-motif binding ($K_d=1-10 \mu\text{M}$). In our work we demonstrated that ATF2 does not only engage the p38 FRS, but the DRS as well, as the deletion of the Zn-finger+D-motif module lowered the phosphorylation efficiency. To show an other bipartite binding example from the literature, the Ets transcription factor engages both DRS and FRS of ERK2 in a non-canonical way, where the two sub-optimal Ets regions bind to ERK with a low $K_d \sim 30 \mu\text{M}$ affinity [42]. Even so, the phosphoswitch (T38) located between the two binding regions of Ets is responsive to the upstream stimulus from the MEK/ERK pathway. Therefore, it is important to further investigate the

weak non-canonical partners of the MAPKs, as they could provide biologically relevant contribution to the molecular network.

5.2 Non-canonical interactions enable fine-tuned activation of phosphoswitch motifs in MAPK substrates

Most of the MAPK controlled phosphoswitches in transcription factors regulate immediate early (IE) genes (e.g. Fos) as a first round of response to stimuli. Therefore the rate of IE transcription is continuously variable and coupled directly to the strength of intracellular signaling events [155]. Instead of stable binary on/off switches, their induction can be more described as a quantitative rheostat behaviour switch. This allows the system to respond to the intracellular signaling in a more graded manner. Therefore, the multiple levels of complexity in MAPK signaling pathways needs to be taken into account in understanding the transcriptional response. 1) MAPKs can be activated by multiple upstream cascades (e.g. the overlapping p38 and JNK cascade). Additionally, the same stimulus produces different MAPK activation profiles in different cell types. 2) myriad of *in vitro* and cell-based studies indicate that most transcription factors can be phosphorylated by more than one kinase (e.g. ELK-1, ATF2), which provides opportunities for signals arriving from different cascades [156]. 3) Multiple transcription factors may be involved in controlling the same gene. For example, in the regulation of *c-jun* gene expression, substrates of different MAPKs are implicated, such as ATF-2, c-Jun and MEF2 in the long *c-jun* promoter harboring multiple binding sites for these regulators [157]. Moreover, Ap-1 transcription factors occupy their DNA-binding site mainly as heterodimers that can be complemented with a third transcription factor (e.g. ATF2/c-Jun + IRF-3, or c-JUN/Fos + NFAT4) [158,159]. This combinatorial association of transcription factors further complicates the regulation.

In our study we examined one segment of the MAPK signaling pathway and focused on the biochemical behavior of a transcription regulating phosphoswitch in the ATF2 TAD domain. We also examined ATF2 TAD transactivation activity in a simplified artificial system fused to GAL4 DNA binding domain. We found that both JNK and p38 affect transcriptional activity through distinct binding sites in the ATF2 TAD. It is intriguing how the modularly built ATF2-TAD looks like in more ancient organisms.

Evolution of MAPK binding motifs in ATF2

We showed, that the JNK specific Zn-finger+D-motif module and the pp-p38 binding FENEF motif-like regions are both present in most extant organisms even in sponges (Appendix Figure 3A). Interestingly, exceptions can be found in *Protostomata*, where the JNK-binding module is absent while the p38-binding linear motif is clearly present, e.g. in *D. melanogaster* and *C. elegans* (Appendix Figure 3B). In agreement with this observation, the *Drosophila* homologue of ATF2 (dATF-2) is found to be phosphorylated and regulated by only p38 and not by JNK in this organism [160]. This phenomenon allowed the researchers to study ATF2 mediated stress response in a simplified system. Seong et al. (2011) showed in *Drosophila* that heat or osmotic shock induced phosphorylation of dATF-2 via Mekk1-p38 disrupts heterochromatin. Moreover, osmotic stress reduced the level of H3K9 di-methylation at dATF-2 bound heterochromatic sites [161]. In the *Fungi* kingdom, the NPFENEF motif is found, but the Zn-finger+D-motif completely is missing from the TAD of ATF orthologs. Transcriptional activity of the fission yeast (*Schizosaccharomyces pombe*) ATF2 homologue (Atf1) is described to be regulated by the mammalian p38 homologue (Spc1/Hog1) and involved in meiosis and stress response [162].

Our evolutionary sequence conservation analysis showed that in invertebrates an asparagine is found instead of serine at position 90 of the SPFENEF motif. We described that residues at position 90 strongly affects pp-p38 binding. The asparagine at this position mediates tighter binding (by about 5-fold) compared to a serine, while phosphorylation at Ser90 by JNK abolishes binding. Our crystal structure suggests that the residue at 90 is placed into a key position where the chemical nature of its side chain affects the conformation of the SPFENEF motif by influencing intra-motif and intermolecular H-bond formation. The higher affinity of the S90N may be explained by a more optimal side-chain at a critical position of the protein-protein binding interface. This mutant showed higher pre-formed alpha-helical content compared to the wild-type peptide. Conversely, a far less favorable chemical group for this position, the negatively charged and bulky phosphate, caused diminished binding.

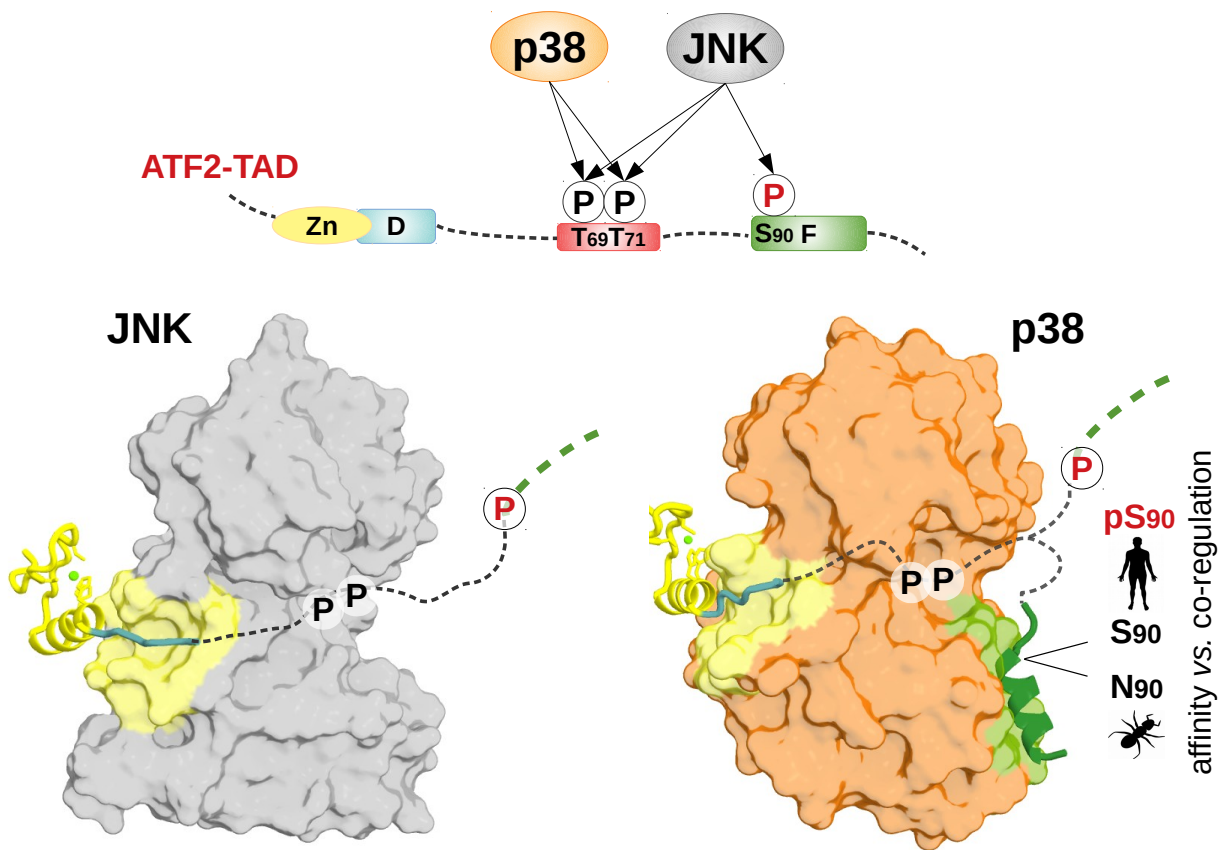


Figure 37 Co-regulation of ATF2 phosphoswitch by JNK and p38. JNK binds to the Zn-finger+D-motif module and phosphorylates T69, T71 and S90 sites. p38 is able to phosphorylate T69 and T71 sites only and binds to ATF2 in a bipartite manner if the 90th amino acid is not phosphorylated. In invertebrate ATF2, the asparagine at position 90 cannot be regulated by JNK, but it also binds p38 with higher affinity.

In conclusion, comparative sequence analysis of ATF2 homologues together with the biochemical studies suggests that the modular architecture of ATF2-TAD with distinct MAPK binding sites has gone through important evolutionary changes (Figure 37). From single regulation by p38 co-regulation with JNK seems to have evolved in *Invertebrates* first, which further evolved into a more complex phosphoregulation by S90 in *Vertebrates*.

Evolutionarily relevant phenotypic variations do not only appear in *cis*-regulatory elements in non-coding DNA (e.g. promoters) but also in the transcription factor protein sequence. These latter mutations often affect protein-protein interactions of TFs, which is important for the recruitment of other TFs, coactivators, corepressors and finally the transcriptional machinery. Ultimately, these changes may lead to an altered response to signaling pathways [163]. For example, the protein sequence outside of the DNA-binding homeodomains of Hox orthologues diverge significantly in

insects. The appearance of a poly-alanine motif C-terminally to the homeodomains increased the repression potency of Ubx protein and facilitated the greater morphological diversification of modern insects [164]. In placental mammals, a single amino-acid change in the CCAAT/enhancer binding protein- β (CEBPB) modified its response to cyclic AMP/protein kinase A/GSK-3 β signaling, which in turn changed the expression of prolactin hormone. The novel function came about because of the mutation reorganizing the location of key phosphorylation sites. These simple changes in the architecture of the transcription controlling regulatory domain of CEBPB was sufficient to cause a fundamental change, from repression to activation, in how the TF responded to phosphorylation [165]. Short linear motifs (SLiMs) in disordered regions are particularly evolvable due their small size and the lack of structural constraints: a single mutation is often enough to change the functionality of the SLiM, giving them a high degree of evolutionary plasticity [166]. The importance of the gain and loss of different SLiM motifs was studied extensively in the segmentation of the *Drosophila* lineage [163].

In conclusion, changes in regulatory domains of transcription factors seem to be important in the evolution of gene regulation, and it can arise from the appearance of new simple modular elements or a single amino acid mutation, as we presented in the case of the ATF2 TAD.

Complex combinatorial response of the ATF2 phosphoswitch to MAPK signaling flux

Physiological responses to extracellular signals depend on a complex activation pattern of different MAPKs (e.g. ERK1/2, JNK and p38). The response is not exclusive but combinatorial, and not binary (i.e. on or off) but quantitative. Moreover, deviation from a “normal” pattern may lead to signaling related diseases such as cancer or inflammation [3,11], or even to drug resistance[167]. For ATF2 we created a simplified model how this MAPK substrate reads out different MAPK activation profiles. The mechanistic basis behind this apparently complex process is simple: MAPK binding regions and the phosphorylation sites are organized into a specific linear pattern.

Interestingly, in the similarly built Elk-1 TAD phosphorylation sites provide a self-limiting response to ERK activation in a different way. The phosphorylation rate of distinct sites was found to be determined by their position relative to ERK2 docking motifs binding to D- or F-site. Residues that were fast phosphorylated promoted but residues that were phosphorylated slowly attenuated co-activator protein binding. In brief, the Elk-1 TAD harbors a MAPK controlled phosphoswitch capable of directing a self-limiting response [70].

In our work, we provided the biochemical basis and a simplified model on how different JNK and p38 fluxes regulate the modularly built ATF2-TAD in invertebrates and vertebrates. Surprisingly, ATF2 TAD does not simply integrate the signal coming from JNK and p38, but due to its unique architecture may sense the relative strength of the two MAPK pathways in vertebrates. The basic signal integration capacity of the pre-vertebrate ATF2-TAD architecture comprised of JNK and p38 binding sites became more complex due to an amino-acid change (Asn to Ser at 90) in the critical p38 binding region in vertebrates. JNK acquired the capacity to have a direct influence on how another MAPK, p38, effects ATF2 mediated transcription. ATF2 is a constitutively expressed protein and plays a major role in controlling the transcription of other intermediate early (IE) transcription factors and its knock-out in mice has defects in skeletal and central nervous system development [84]. We assume that JNK/p38 based co-regulation of ATF2 activity may contribute to primary (IE) gene response diversity which is characteristic to different cell-types or development processes [155]. Unfortunately, the exact biological significance of this complex regulation of the ATF2 phosphoswitch is not known yet but further studies addressing gene regulation at the systems level (e.g. transcriptomics) may provide valuable insights into how the ATF2 TAD governs transcription in different cellular environments.

6. Acknowledgment

I would like to express my gratitude to my supervisor Attila Reményi, for his continuous support and guidance of my work, for every opportunity and granted freedom during my PhD research. I am also thankful for him for organizing multiple collaborations.

I was honored to be the student of Zeke András. I am thankful for the many intellectual discussions, and for sharing his expertise and for the help in my initial experiments.

I would like to thank to my friends, Péter Sok and Ádám Levente Póti graduate students for the inspirations and lifting mood during along all the years we spent in the lab.

I would like to thank to Anita Alexa for the unconditional help in every aspect of the lab work. I would like to thank all of my other colleges from the Reményi lab, Anna Sebő, Péter Egri, Neha Singh, Eszter Kállainé Szarka, Kinga Papp and alumni members, Gábor Glatz, Gergő Gógl and Ágnes Garai. I would like to thank Marianna Rakács and Krisztián Albert for their constant assistance.

I am grateful to Tóke Orsolya for her immediate help and advice for the NMR measurements. I also wish to thank Ashish Sethi and Paul Gooley for the help in NMR studies and Marie Bogoyevitch for supporting my stay in the University of Melbourne, where I have gained a lot of experience. I am grateful for the data collection of the protein crystals to Isabel Bento, EMBL Hamburg. I am thankful for the experiments carried out by Ganeshan Senthil Kumar in the group of Wolfgang Peti. I am thankful for Imre Tímea and Szabó Pál for the MS analysis of the protein samples. Additionally, I would like to thank Péter Kele and Krisztina Németh for the collaboration and the opportunity to gain insight into chemical biology. I would like to thank all colleges in the Institute of Enzymology and the Institute of Organic Chemistry for their technical help and discussions.

I am grateful to my good friends inside and outside the research community for their moral support.

I would like to express my special thanks to my parents and brother for giving me the opportunity to study and for the encouragement. I would like to thank to my husband's family for their continuous help. Last but not the least, I would like to thank my husband for his support, care and patience throughout my graduate studies.

7. Summary

Cells are very flexible to adapt to their environment through intracellular signal transduction pathways. Mitogen-activated protein kinases (MAPKs) are ubiquitous proteins in the human signaling network, as they mediate responses to growth factors, various stress signals, or proinflammatory cytokines. After pathway activation, they phosphorylate their substrates on the target S/TP motif. For the specific recognition of substrates and other partners - such as activators and regulatory proteins - they utilize their protein-protein interaction grooves (DRS and FRS) to bind well-defined linear motifs (D-motifs and F-motifs). These regular or canonical interactions play a well-established role in the MAPK interactome. In some – non-canonical - cases, the MAPK-partner complex is structurally unique and cannot be predicted based on sequence analysis. In my thesis I studied two non-canonical MAPK substrate candidates to better understand their phosphoregulation.

The phosphoswitch in the transactivation domain of the ATF2 transcription factor can be regulated by JNK and p38 MAPKs. I presented and structurally characterized the non-canonical interactions of ATF2 towards both MAPKs. I determined the crystal structure of JNK bound to the minimized ATF2 transactivation domain. Our biochemical and structural data show how a small Zn-finger domain in ATF2 increases the specificity of an adjacent linear D-motif to the JNK DRS, and the same time reduces the entropic cost of the interaction. Additionally, I found that a linear motif from my other candidate substrate, the DCX protein binds to the JNK DRS in an unusual backbone conformation. I identified and determined the crystal structure of an F-motif from the ATF2-TAD in complex with activated p38. This shows for the first time how the FRS site of the MAPK is engaged in substrate binding and reveals why this interaction depends on the phosphorylation state of the kinase. I further characterized ATF2-TAD binding to p38 biochemically and described its bipartite binding properties. Intriguingly, I showed how a JNK-dependent phosphorylation site in the the F-motif diminishes p38 binding in vertebrates (S90). Importantly, this amino acid cannot be regulated by JNK in invertebrates (N90) and causes stronger binding to p38. With *in silico* network modeling I compared the vertebrate and invertebrate ATF-JNK-p38 module under different upstream signaling flux conditions. Unexpectedly, I found that the ATF2 TAD does not simply integrate the signal coming from JNK and p38, but due to its unique architecture may sense the relative strength of these two MAPK pathways in vertebrates. This latter regulatory capacity has risen because of a single amino-acid change (N to S) at a critical position in the more ancient ATF2 phosphoswitch region found in invertebrates.

In conclusion, I studied non-canonical complexes of ATF2 with JNK and p38 and provided the mechanistic basis of co-regulation of the ATF2-TAD phosphoswitch by two kinases. Although I did not find a fundamentally different or non-canonical interaction between DCX and JNK, I described a new D-motif in DCX.

8. Összefoglalás

Az élő sejt képes alkalmazkodni a különféle környezeti változásokhoz, melyet a sejten belül megvalósuló jelátvitel mechanizmusa tesz lehetővé. A Mitogén-aktivált protein kinázok (MAPK) nélkülözhetetlen szereplői az emberi jelátviteli hálózatoknak, hiszen képesek reagálni növekedési faktorokra vagy éppen a környezeti stresszre. Aktiválódásuk után szubsztrátaikat S/TP motívumon foszforilálják. A szubsztrátok és egyéb partnerfehérjék specifikus felismerésére a MAP kinázok különálló fehérje-fehérje kölcsönhatási árkokat (DRS és FRS) használnak, melyek meghatározott konszenzus szekvenciával rendelkező lineáris motívumokat (D- és F- motívum) kötnek. Ezek a klasszikus vagy kanonikus kölcsönhatások határozzák meg a MAP kináz interakomjának jelentős részét. Ennek ellenére ismerünk olyan nem kanonikus eseteket, ahol a fehérje-fehérje komplex képződése szerkezetileg egyedi, és nem jósolható meg az aminosav szekvencia alapján. A disszertációmban kettő ilyen, vélhetően nem kanonikus MAPK szubsztrátot vizsgáltam, hogy jobban megértsem a foszfo-szabályozásukat.

Az ATF2 transzkripciós faktor foszfokapcsolóját a JNK és p38 szabályozza. Bemutattam, hogy az ATF2 nem kanonikus interakcióban vesz részt mindkét MAPK-val. Meghatároztam a JNK1 az ATF2-TAD minimális kötőrégiójával alkotott komplexének a szerkezetét. Ez a szerkezeti modell rávilágít arra, hogyan képes megváltoztatni a lineáris D-motívummal átlapoló cink-ujj domén a MAP kináz specificitást és hogyan csökkenti a kötődés entropikus költségét. Ezen kívül, bemutattam, hogy egy D-motívum a másik vizsgált szubsztrátból, a DCX-ből, szokatlan kötésmóddal foglalja el a JNK DRS-t. Meghatároztam a p38 és az ATF2-TAD-ban található F-motívumnak a szerkezetét is. Ez az első röntgenszerkezet a MAPK FRS-árok + F-motívum kötődésről, és megmagyarázza, hogy miért függ ez a típusú kölcsönhatás a kináz foszforilációs állapotától. Kimutattam azt is, hogy az ATF2-TAD a p38-al bipartikus kölcsönhatásban vesz részt. Továbbá felderítettem, hogyan befolyásolja egy JNK-függő foszforilációs hely (S90) az ATF2-p38 kölcsönhatást gerincesekben. Gerinctelen állatokban ez az aminosav (N90) nem szabályozható JNK által, és egyben erősebb p38 kötést eredményez. *In silico* modellezéssel összehasonlítottam a gerinces és gerinctelen ATF2 TAD foszforilációs szintjét különböző JNK és p38 bemenetek mellett. Az ATF2 TAD nem csupán integrálja a JNK és p38 felől érkező jeleket, hanem a két MAPK jelpálya relatív erősségét is képes érzékelni a gerincesekben, mindössze egyetlen aminosavcsere miatt (N-ből S).

Összefoglalásul, doktori munkámban az ATF2 és aktiváló kinázai, a JNK és p38 nem kanonikus interakcióival foglalkoztam, és tanulmányoztam az ATF2-TAD foszfokapcsoló szabályozását a két kináz közreműködésével. Bár a DCX és JNK közötti kötés kanonikusnak bizonyult, mert egy D-motívum révén képes autonóm módon létrejönni, a DCX-ben lévő JNK kötőmotívum egy újfajta kötési módot mutat be.

9. References

1. Betts MJ, Wichmann O, Utz M, Andre T, Petsalaki E, Minguéz P, et al. Systematic identification of phosphorylation-mediated protein interaction switches. *PLoS Comput Biol*. 2017;13(3):1–20.
2. Hotamisligil GS, Davis RJ. Cell signaling and stress responses. *Cold Spring Harb Perspect Biol*. 2016;8(10).
3. Kim EK, Choi EJ. Compromised MAPK signaling in human diseases: an update. Vol. 89, *Archives of Toxicology*. Springer Verlag; 2015. p. 867–82.
4. Burley SK, Bhikadiya C, Bi C, Bittrich S, Chen L, Crichlow G V., et al. RCSB Protein Data Bank: Powerful new tools for exploring 3D structures of biological macromolecules for basic and applied research and education in fundamental biology, biomedicine, biotechnology, bioengineering and energy sciences. *Nucleic Acids Res*. 2021;49(1):D437–51.
5. Garai Á, Zeke A, Gógl G, Törő I, Fördős F, Blankenburg H, et al. Specificity of linear motifs that bind to a common mitogen-activated protein kinase docking groove. *Sci Signal*. 2012 Oct 9;5(245):ra74.
6. Lavoie H, Therrien M. Regulation of RAF protein kinases in ERK signalling. *Nat Rev Mol Cell Biol*. 2015;16(5):281–98.
7. Morrison DK. MAP kinase pathways. *Cold Spring Harb Perspect Biol*. 2012;4(11):1–6.
8. Takekawa M, Saito H. A family of stress-inducible GADD45-like proteins mediate activation of the stress-responsive MTK1/MEKK4 MAPKKK. *Cell*. 1998;95(4):521–30.
9. Coffey ET. Nuclear and cytosolic JNK signalling in neurons. *Nat Rev Neurosci*. 2014;15(5):285–99.
10. Keren A, Tamir Y, Bengal E. The p38 MAPK signaling pathway: A major regulator of skeletal muscle development. *Mol Cell Endocrinol*. 2006;252(1–2):224–30.
11. Wagner EF, Nebreda ÁR. Signal integration by JNK and p38 MAPK pathways in cancer development. Vol. 9, *Nature Reviews Cancer*. 2009. p. 537–49.
12. Yan L, Carr J, Ashby PR, Murry-Tait V, Thompson C, Arthur JSC. Knockout of ERK5 causes multiple defects in placental and embryonic development. *BMC Dev Biol*. 2003;3:1–21.
13. Whitmarsh AJ, Davis RJ. Regulation of transcription factor function by phosphorylation. *Cell Mol Life Sci*. 2000;57(8–9):1172–83.

14. Olson BL, Hock MB, Ekholm-Reed S, Wohlschlegel JA, Dev KK, Kralli A, et al. SCFCdc4 acts antagonistically to the PGC-1 α transcriptional coactivator by targeting it for ubiquitin-mediated proteolysis. *Genes Dev.* 2008;22(2):252–64.
15. Chang L, Jones Y, Ellisman MH, Goldstein LSB, Karin M. JNK1 is required for maintenance of neuronal microtubules and controls phosphorylation of microtubule-associated proteins. *Dev Cell.* 2003;4(4):521–33.
16. Moens U, Kostenko S, Sveinbjörnsson B. The role of mitogen-activated protein kinase-activated protein kinases (MAPKAPKs) in inflammation. *Genes (Basel).* 2013;4(2):101–33.
17. Kannan N, Neuwald AF. Evolutionary constraints associated with functional specificity of the CMGC protein kinases MAPK, CDK, GSK, SRPK, DYRK, and CK2 α . *Protein Sci.* 2004;13(8):2059–77.
18. Gógl G, Kornev AP, Reményi A, Taylor SS. Disordered Protein Kinase Regions in Regulation of Kinase Domain Cores. *Trends Biochem Sci.* 2019;44(4):300–11.
19. Matte A, Tari LW, Delbaere LT. How do kinases transfer phosphoryl groups? *Structure.* 1998;6(4):413–9.
20. Jacobs D, Glossip D, Xing H, Muslin AJ, Kornfeld K. Multiple docking sites on substrate proteins form a modular system that mediates recognition by ERK MAP kinase. *Genes Dev.* 1999;13(2):163–75.
21. Ubersax JA, Ferrell JE. Mechanisms of specificity in protein phosphorylation. *Nat Rev Mol Cell Biol.* 2007;8(7):530–41.
22. Rainey MA, Callaway K, Barnes R, Wilson B, Dalby KN. Proximity-induced catalysis by the protein kinase ERK2. *J Am Chem Soc.* 2005;127(30):10494–5.
23. Reményi A, Good MC, Lim W a. Docking interactions in protein kinase and phosphatase networks. *Curr Opin Struct Biol.* 2006 Dec;16(6):676–85.
24. Cheng KY, Noble MEM, Skamnaki V, Brown NR, Lowe ED, Kontogiannis L, et al. The role of the phospho-CDK2/cyclin A recruitment site in substrate recognition. *J Biol Chem.* 2006;281(32):23167–79.
25. Elia AEH, Rellos P, Haire LF, Chao JW, Ivins FJ, Hoepker K, et al. The molecular basis for phosphodependent substrate targeting and regulation of Plks by the Polo-box domain. *Cell.* 2003;115(1):83–95.
26. Sheridan DL, Kong Y, Parker SA, Dalby KN, Turk BE. Substrate discrimination among mitogen-activated protein kinases through distinct docking sequence motifs. *J Biol Chem.* 2008 Jul 11;283(28):19511–20.

27. Lee T, Hoofnagle AN, Kabuyama Y, Stroud J, Min X, Goldsmith EJ, et al. Docking motif interactions in Map kinases revealed by hydrogen exchange mass spectrometry. *Mol Cell*. 2004;14(1):43–55.
28. Dosztányi Z, Mészáros B, Simon I. ANCHOR: Web server for predicting protein binding regions in disordered proteins. *Bioinformatics*. 2009;25(20):2745–6.
29. Schymkowitz J, Borg J, Stricher F, Nys R, Rousseau F, Serrano L. The FoldX web server: An online force field. *Nucleic Acids Res*. 2005;33(SUPPL. 2):382–8.
30. Zeke A, Bastys T, Alexa A, Garai Á, Mészáros B, Kirsch K, et al. Systematic discovery of linear binding motifs targeting an ancient protein interaction surface on MAP kinases. *Mol Syst Biol*. 2015;11(11):837.
31. Gouw M, Michael S, Sámano-Sánchez H, Kumar M, Zeke A, Lang B, et al. The eukaryotic linear motif resource - 2018 update. *Nucleic Acids Res*. 2018;46(D1):D428–34.
32. Pellegrini E, Palencia A, Braun L, Kapp U, Bougdour A, Belrhali H, et al. Structural Basis for the Subversion of MAP Kinase Signaling by an Intrinsically Disordered Parasite Secreted Agonist. *Structure*. 2017;25(1):16–26.
33. Glatz G, Gógl G, Alexa A, Reményi A. Structural mechanism for the specific assembly and activation of the extracellular signal regulated kinase 5 (ERK5) module. *J Biol Chem*. 2013 Mar 22;288(12):8596–609.
34. Piserchio A, Ramakrishan V, Wang H, Kaoud TS, Arshava B, Dutta K, et al. Structural and dynamic features of F-recruitment site driven substrate phosphorylation by ERK2. *Sci Rep*. 2015 Jun 8;5.
35. Dajani R, Fraser E, Roe SM, Yeo M, Good VM, Thompson V, et al. Structural basis for recruitment of glycogen synthase kinase 3 β to the axin-APC scaffold complex. *EMBO J*. 2003;22(3):494–501.
36. Bax B, Carter PS, Lewis C, Guy AR, Bridges A, Tanner R, et al. The structure of phosphorylated GSK-3 β complexed with a peptide, FRATtide, that inhibits β -catenin phosphorylation. *Structure*. 2001;9(12):1143–52.
37. Miskei M, Horvath A, Vendruscolo M, Fuxreiter M. Sequence-Based Prediction of Fuzzy Protein Interactions. *J Mol Biol*. 2020;432(7):2289–303.
38. Ozenne V, Bauer F, Salmon L, Huang JR, Jensen MR, Segard S, et al. Flexible-meccano: A tool for the generation of explicit ensemble descriptions of intrinsically disordered proteins and their associated experimental observables. *Bioinformatics*. 2012;28(11):1463–70.
39. de Vries SJ, van Dijk M, Bonvin AMJJ. The HADDOCK web server for data-driven biomolecular docking. *Nat Protoc*. 2010;5(5):883–97.

40. Róycki B, Kim YC, Hummer G. SAXS ensemble refinement of ESCRT-III CHMP3 conformational transitions. *Structure*. 2011;19(1):109–16.
41. Fantz DA, Jacobs D, Glossip D, Kornfeld K. Docking Sites on Substrate Proteins Direct Extracellular Signal-regulated Kinase to Phosphorylate Specific Residues. *J Biol Chem*. 2001;276(29):27256–65.
42. Piserchio A, Warthaka M, Kaoud TS, Callaway K, Dalby KN, Ghose R. Local destabilization, rigid body, and fuzzy docking facilitate the phosphorylation of the transcription factor Ets-1 by the mitogen-activated protein kinase ERK2. *Proc Natl Acad Sci*. 2017;114(31):E6287–96.
43. MacE PD, Wallez Y, Egger MF, Dobaczewska MK, Robinson H, Pasquale EB, et al. Structure of ERK2 bound to PEA-15 reveals a mechanism for rapid release of activated MAPK. *Nat Commun*. 2013;4.
44. Liu X, Zhang CS, Lu C, Lin SC, Wu JW, Wang ZX. A conserved motif in JNK/p38-specific MAPK phosphatases as a determinant for JNK1 recognition and inactivation. *Nat Commun*. 2016;7.
45. Zhang YY, Wu JW, Wang ZX. A distinct interaction mode revealed by the crystal structure of the kinase p38 α with the MAPK binding domain of the phosphatase MKP5. *Sci Signal*. 2011;4(204):1–10.
46. Kumar GS, Zettl H, Page R, Peti W. Structural basis for the regulation of the mitogen-activated protein (MAP) kinase p38 α by the dual specificity phosphatase 16 MAP kinase binding domain in solution. *J Biol Chem*. 2013;288(39):28347–56.
47. Lu C, Liu X, Zhang CS, Gong H, Wu JW, Wang ZX. Structural and Dynamic Insights into the Mechanism of Allosteric Signal Transmission in ERK2-Mediated MKP3 Activation. *Biochemistry*. 2017;56(46):6166–76.
48. Liu S, Sun JP, Zhou B, Zhang ZY. Structural basis of docking interactions between ERK2 and MAP kinase phosphatase 3. *Proc Natl Acad Sci U S A*. 2006;103(14):5326–31.
49. Farooq A, Chaturvedi G, Mujtaba S, Plotnikova O, Zeng L, Dhalluin C, et al. Solution structure of ERK2 binding domain of MAPK phosphatase MKP-3: Structural insights into MKP-3 activation by ERK2. *Mol Cell*. 2001;7(2):387–99.
50. Goldsmith EJ. Three-dimensional docking in the MAPK p38 α . *Sci Signal*. 2011;4(204):3–5.
51. Song H, Hanlon N, Brown NR, Noble MEM, Johnson LN, Barford D. Phosphoprotein-protein interactions revealed by the crystal structure of kinase-associated phosphatase in complex with phosphoCDK2. *Mol Cell*. 2001;7(3):615–26.

52. Bhattacharyya RP, Reményi A, Good MC, Bashor CJ, Falick AM, Lim W a. The Ste5 scaffold allosterically modulates signaling output of the yeast mating pathway. *Science*. 2006;311(5762):822–6.
53. De Nicola GF, Martin ED, Chaikuad A, Bassi R, Clark J, Martino L, et al. Mechanism and consequence of the autoactivation of p38 α mitogen-activated protein kinase promoted by TAB1. *Nat Struct Mol Biol*. 2013;20(10):1182–92.
54. De Nicola GF, Bassi R, Nichols C, Fernandez-Caggiano M, Golfroush PA, Thapa D, et al. The TAB1-p38 α complex aggravates myocardial injury and can be targeted by small molecules. *JCI insight*. 2018;3(16).
55. Francis DM, Ră B, Koveal D, Hummer G, Page R, Peti W. Structural basis of p38 α regulation by hematopoietic tyrosine phosphatase. *Nat Chem Biol*. 2011;7(12):916–24.
56. Delaforge E, Kragelj J, Tengo L, Palencia A, Milles S, Bouvignies G, et al. Deciphering the Dynamic Interaction Profile of an Intrinsically Disordered Protein by NMR Exchange Spectroscopy. *J Am Chem Soc*. 2018;140(3):1148–58.
57. Alexa A, Gógl G, Glatz G, Garai Á, Zeke A, Varga J, et al. Structural assembly of the signaling competent ERK2-RSK1 heterodimeric protein kinase complex. *Proc Natl Acad Sci U S A*. 2015;112(9):2711–6.
58. White A, Pargellis C a, Studts JM, Werneburg BG, Farmer BT. Molecular basis of MAPK-activated protein kinase 2:p38 assembly. *Proc Natl Acad Sci U S A*. 2007;104(15):6353–8.
59. Sok P, Gógl G, Kumar GS, Alexa A, Singh N, Kirsch K, et al. MAP Kinase-Mediated Activation of RSK1 and MK2 Substrate Kinases. *Structure*. 2020;28(10):1101-1113.e5.
60. Francis DM, Róycki B, Tortajada A, Hummer G, Peti W, Page R. Resting and active states of the ERK2:HePTP complex. *J Am Chem Soc*. 2011;133(43):17138–41.
61. Sharrocks AD, Yang SH, Galanis A. Docking domains and substrate-specificity determination for MAP kinases. *Trends Biochem Sci*. 2000;25(9):448–53.
62. Yang S-H, Yates PR, Whitmarsh AJ, Davis RJ, Sharrocks AD. The Elk-1 ETS-Domain Transcription Factor Contains a Mitogen-Activated Protein Kinase Targeting Motif. *Mol Cell Biol*. 1998;18(2):710–20.
63. Ghose R. Nature of the Pre-Chemistry Ensemble in Mitogen-Activated Protein Kinases. *J Mol Biol*. 2019;431(2):145–57.
64. Seidel JJ, Graves BJ. An ERK2 docking site in the Pointed domain distinguishes a subset of ETS transcription factors. *Genes Dev*. 2002;16(1):127–37.

65. Humphreys JM, Piali AT, Akella R, He H, Goldsmith EJ. Precisely ordered phosphorylation reactions in the p38 mitogen-activated protein (MAP) kinase cascade. *J Biol Chem.* 2013;288(32):23322–30.
66. Waas WF, Lo HH, Dalby KN. The kinetic mechanism of the dual phosphorylation of the ATF2 transcription factor by p38 mitogen-activated protein (MAP) kinase alpha. Implications for signal/response profiles of MAP kinase pathways. *J Biol Chem.* 2001 Feb 23;276(8):5676–84.
67. Rubinstein BY, Mattingly HH, Berezhkovskii AM, Shvartsman SY. Long-Term dynamics of multisite phosphorylation. *Mol Biol Cell.* 2016;27(14):2331–40.
68. Salazar C, Höfer T. Multisite protein phosphorylation - From molecular mechanisms to kinetic models. *FEBS J.* 2009;276(12):3177–98.
69. Balamotis MA, Pennella MA, Stevens JL, Wasylyk B, Belmont AS, Berk AJ. Complexity in transcription control at the activation domain-Mediator interface. *Sci Signal.* 2009;2(69):1–12.
70. Mylona A, Theillet FX, Foster C, Cheng TM, Miralles F, Bates PA, et al. Opposing effects of Elk-1 multisite phosphorylation shape its response to ERK activation. *Science (80-).* 2016;354(6309):233–7.
71. Chen RH, Abate C, Blenis J. Phosphorylation of the c-Fos transrepression domain by mitogen-activated protein kinase and 90-kDa ribosomal S6 kinase. *Proc Natl Acad Sci U S A.* 1993 Dec 1;90(23):10952–6.
72. Smeal T, Binetruy B, Mercola DA, Birrer M, Karin M. Oncogenic and transcriptional cooperation with Ha-Ras requires phosphorylation of c-Jun on serines 63 and 73. *Nature.* 1991;354:56–8.
73. Livingstone C, Patel G, Jones N. ATF-2 contains a phosphorylation-dependent transcriptional activation domain. *EMBO J.* 1995;14(8):1785–97.
74. Duyndam MCA, Van Dam H, Smits PHM, Verlaan M, Van Der Eb AJ, Zantema A. The N-terminal transactivation domain of ATF2 is a target for the co-operative activation of the c-jun promoter by p300 and 12S E1A. *Oncogene.* 1999 Apr 8;18(14):2311–21.
75. Kawasaki H, Song J, Eckner R, Ugai H, Chiu R, Taira K, et al. p300 and ATF-2 are components of the DRF complex, which regulates retinoic acid- and E1A-mediated transcription of the c-jun gene in F9 cells. *Genes Dev.* 1998;12(2):233–45.
76. Dunn C, Wiltshire C, MacLaren A, Gillespie DAF. Molecular mechanism and biological functions of c-Jun N-terminal kinase signalling via the c-Jun transcription factor. *Cell Signal.* 2002;14(7):585–93.

77. Hibi M, Lin A, Smeal T, Minden A, Karin M. Identification of an oncoprotein- and UV-responsive protein kinase that binds and potentiates the c-Jun activation domain. *Genes Dev.* 1993;7(11):2135–48.
78. Gupta S, Campbell D, Dérijard B, Davis RJ. Transcription factor ATF2 regulation by the JNK signal transduction pathway. *Science (80-)*. 1995;267(5196):389–93.
79. Raingeaud J, Whitmarsh AJ, Barrett T, Dérijard B, Davis RJ. MKK3- and MKK6-regulated gene expression is mediated by the p38 mitogen-activated protein kinase signal transduction pathway. *Mol Cell Biol.* 1996;16(3):1247–55.
80. Gdalyahu A, Ghosh I, Levy T, Sapir T, Sapoznik S, Fishler Y, et al. DCX, a new mediator of the JNK pathway. *EMBO J.* 2004 Mar 25;23(4):823–32.
81. Maekawa T, Sakura H, Kanei-Ishii C, Sudo T, Yoshimura T, Fujisawa J, et al. Leucine zipper structure of the protein CRE-BP1 binding to the cyclic AMP response element in brain. *EMBO J.* 1989;8(7):2023–8.
82. Watson G, Ronai Z, Lau E. ATF2, a paradigm of the multifaceted regulation of transcription factors in biology and disease. *Pharmacol Res.* 2017;119:347–57.
83. Lau E, Ronai Z a. ATF2 - at the crossroad of nuclear and cytosolic functions. *J Cell Sci.* 2012 Jun 15;125(Pt 12):2815–24.
84. Reimold AM, Grusby MJ, Kosaras B, Fries JWU, Mori R, Maniwa S, et al. Chondrodysplasia and neurological abnormalities in ATF-2-deficient mice. Vol. 379, *Nature*. 1996. p. 262–5.
85. Ackermann J, Ashton G, Lyons S, James D, Hornung JP, Jones N, et al. Loss of ATF2 function leads to cranial motoneuron degeneration during embryonic mouse development. *PLoS One.* 2011;6(4).
86. Hai T, Curran T. Cross-family dimerization of transcription factors Fos/Jun and ATF/CREB alters DNA binding specificity. *Proc Natl Acad Sci U S A.* 1991;88(9):3720–4.
87. Breitwieser W, Lyons S, Flenniken AM, Ashton G, Bruder G, Willington M, et al. Feedback regulation of p38 activity via ATF2 is essential for survival of embryonic liver cells. *Genes Dev.* 2007;21(16):2069–82.
88. Li XY, Green MR. Intramolecular inhibition of activating transcription factor-2 function by its DNA-binding domain. *Genes Dev.* 1996;10(5):517–27.
89. Liu H, Deng X, Shyu YJ, Li JJ, Taparowsky EJ, Hu C-D. Mutual regulation of c-Jun and ATF2 by transcriptional activation and subcellular localization. *EMBO J.* 2006;25(5):1058–69.

90. van Dam H, Wilhelm D, Herr I, Steffen a, Herrlich P, Angel P. ATF-2 is preferentially activated by stress-activated protein kinases to mediate c-jun induction in response to genotoxic agents. *EMBO J.* 1995;14(8):1798–811.
91. Zeke A, Misheva M, Reményi A, Bogoyevitch MA. JNK Signaling: Regulation and Functions Based on Complex Protein-Protein Partnerships. *Microbiol Mol Biol Rev.* 2016 Sep;80(3):793–835.
92. Nagadoi a, Nakazawa K, Uda H, Okuno K, Maekawa T, Ishii S, et al. Solution structure of the transactivation domain of ATF-2 comprising a zinc finger-like subdomain and a flexible subdomain. *J Mol Biol.* 1999;287(3):593–607.
93. Laughlin JD, Nwachukwu JC, Figuera-Losada M, Cherry L, Nettles KW, Lograsso P V. Structural mechanisms of allostery and autoinhibition in JNK family kinases. *Structure.* 2012;20(12):2174–84.
94. Frankel AD, Berg JM, Pabo CO. Metal-dependent folding of a single zinc finger from transcription factor IIIA. *Proc Natl Acad Sci U S A.* 1987;84(14):4841–5.
95. McColl DJ, Honchell CD, Frankel AD. Structure-based design of an RNA-binding zinc finger. *Proc Natl Acad Sci U S A.* 1999;96(17):9521–6.
96. Zu YL, Maekawa T, Matsuda S, Ishii S. Complete putative metal finger and leucine zipper structures of CRE-BP1 are required for the E1A-induced trans-activation. *J Biol Chem.* 1991;266(35):24134–9.
97. Hendriks BS, Seidl KM, Chabot JR. Two additive mechanisms impair the differentiation of “substrate-selective” p38 inhibitors from classical p38 inhibitors in vitro. *BMC Syst Biol.* 2010;4.
98. Ivanova IA, Nakrieko KA, Dagnino L. Phosphorylation by p38 MAP kinase is required for E2F1 degradation and keratinocyte differentiation. *Oncogene.* 2009;28(1):52–62.
99. Ploia C, Antoniou X, Sclip A, Grande V, Cardinetti D, Colombo A, et al. JNK plays a key role in tau hyperphosphorylation in alzheimer’s disease models. *J Alzheimer’s Dis.* 2011;26(2):315–29.
100. Kuan CY, Yang DD, Samanta Roy DR, Davis RJ, Rakic P, Flavell RA. The Jnk1 and Jnk2 protein kinases are required for regional specific apoptosis during early brain development. *Neuron.* 1999;22(4):667–76.
101. Kawauchi T, Chihama K, Nabeshima YI, Hoshino M. The in vivo roles of STEF/Tiam1, Rac1 and JNK in cortical neuronal migration. *EMBO J.* 2003;22(16):4190–201.
102. Bai J, Ramos RL, Ackman JB, Thomas AM, Lee R V., LoTurco JJ. RNAi reveals doublecortin is required for radial migration in rat neocortex. *Nat Neurosci.* 2003;6(12):1277–83.

103. Gdalyahu A, Ghosh I, Levy T, Sapir T, Sapoznik S, Fishler Y, et al. DCX, a new mediator of the JNK pathway. *EMBO J.* 2004;23(4):823–32.
104. Reiner O, Gdalyahu A, Ghosh I, Levy T, Sapoznik S, Nir R, et al. DCX's phosphorylation by not just another kinase (JNK). Vol. 3, *Cell Cycle*. Taylor and Francis Inc.; 2004. p. 745–9.
105. Des Portes V, Pinar JM, Billuart P, Vinet MC, Koulakoff A, Carrié A, et al. A novel CNS gene required for neuronal migration and involved in X-linked subcortical laminar heterotopia and lissencephaly syndrome. *Cell.* 1998;92(1):51–61.
106. Kim MH, Cierpicki T, Derewenda U, Krowarsch D, Feng Y, Devedjiev Y, et al. The DCX-domain tandems of doublecortin and doublecortin-like kinase. *Nat Struct Biol.* 2003;10(5):324–33.
107. Manka SW, Moores CA. The role of tubulin–tubulin lattice contacts in the mechanism of microtubule dynamic instability. *Nat Struct Mol Biol.* 2018;25(7).
108. Manka SW, Moores CA. Pseudo repeats in doublecortin make distinct mechanistic contributions to microtubule regulation. *EMBO Rep.* 2020;21(12):1–17.
109. Jin J, Suzuki H, Hirai S-I, Mikoshiba K, Ohshima T. JNK phosphorylates Ser332 of doublecortin and regulates its function in neurite extension and neuronal migration. *Dev Neurobiol.* 2010 Dec;70(14):929–42.
110. Moslehi M, Ng DCH, Bogoyevitch MA. Dynamic microtubule association of Doublecortin X (DCX) is regulated by its C-terminus. *Sci Rep.* 2017;7(1):1–11.
111. Tsukada M, Prokscha A, Oldekamp J, Eichele G. Identification of neurabin II as a novel doublecortin interacting protein. *Mech Dev.* 2003;120(9):1033–43.
112. Tanaka T, Serneo FF, Tseng HC, Kulkarni AB, Tsai LH, Gleeson JG. Cdk5 Phosphorylation of Doublecortin Ser297 Regulates Its Effect on Neuronal Migration. *Neuron.* 2004;41(2):215–27.
113. Moslehi M, Ng DCH, Bogoyevitch MA. Doublecortin X (DCX) serine 28 phosphorylation is a regulatory switch, modulating association of DCX with microtubules and actin filaments. *Biochim Biophys Acta - Mol Cell Res.* 2019;1866(4):638–49.
114. Toriyama M, Mizuno N, Fukami T, Iguchi T, Toriyama M, Tago K, et al. Phosphorylation of doublecortin by protein kinase A orchestrates microtubule and actin dynamics to promote neuronal progenitor cell migration. *J Biol Chem.* 2012 Apr 13;287(16):12691–702.
115. Delaglio F, Grzesiek S, Vuister GW, Zhu G, Pfeifer J, Bax A. NMRPipe: A multidimensional spectral processing system based on UNIX pipes. *J Biomol NMR.* 1995;6(3):277–93.
116. Lee W, Tonelli M, Markley JL. NMRFAM-SPARKY: Enhanced software for biomolecular NMR spectroscopy. *Bioinformatics.* 2015;31(8):1325–7.

117. Ulrich EL, Akutsu H, Doreleijers JF, Harano Y, Ioannidis YE, Lin J, et al. BioMagResBank. *Nucleic Acids Res.* 2008;36(SUPPL. 1):402–8.
118. Kumar GS, Clarkson MW, Kunze MBA, Granata D, Joshua Wand A, Lindorff-Larsen K, et al. Dynamic activation and regulation of the mitogen-activated protein kinase p38. *Proc Natl Acad Sci U S A.* 2018;115(18):4655–60.
119. Marsh JA, Singh VK, Jia Z, Forman-Kay JD. Sensitivity of secondary structure propensities to sequence differences between α - and γ -synuclein: Implications for fibrillation. *Protein Sci.* 2006;15(12):2795–804.
120. van Zundert GCP, Rodrigues JPGLM, Trellet M, Schmitz C, Kastiris PL, Karaca E, et al. The HADDOCK2.2 Web Server: User-Friendly Integrative Modeling of Biomolecular Complexes. *J Mol Biol.* 2015;428(4):720–5.
121. Emsley P, Lohkamp B, Scott WG, Cowtan K. Features and development of Coot. *Acta Crystallogr Sect D Biol Crystallogr.* 2010;66(4):486–501.
122. Nagadoi A, Nakazawa K, Uda H, Okuno K, Maekawa T, Ishii S, et al. Solution structure of the transactivation domain of ATF-2 comprising a zinc finger-like subdomain and a flexible subdomain. *J Mol Biol.* 1999;287(3):593–607.
123. Brünger AT, Adams PD, Clore GM, Delano WL, Gros P, Grosse-Kunstleve RW, et al. Crystallography & NMR system: A new software suite for macromolecular structure determination. *Acta Crystallogr Sect D Biol Crystallogr.* 1998;54(5):905–21.
124. Soundararajan M, Roos AK, Savitsky P, Filippakopoulos P, Kettenbach AN, Olsen J V., et al. Structures of down syndrome kinases, DYRKs, reveal mechanisms of kinase activation and substrate recognition. *Structure.* 2013;21(6):986–96.
125. Lee B, Richards FM. The interpretation of protein structures: Estimation of static accessibility. *J Mol Biol.* 1971;55(3).
126. Tzarum N, Eisenberg-Domovich Y, Gills JJ, Dennis PA, Livnah O. Lipid molecules induce p38 α activation via a novel molecular switch. *J Mol Biol.* 2012;424(5):339–53.
127. Tzarum N, Komornik N, Chetrit D Ben, Engelberg D, Livnah O. DEF pocket in p38 α facilitates substrate selectivity and mediates autophosphorylation. *J Biol Chem.* 2013;288(27):19537–47.
128. Sali A, Blundell T. Sali, A. & Blundell, T. L. Comparative modelling by satisfaction of spatial restraints. *J. Mol. Biol.* 234, 779-815. Vol. 234, Journal of molecular biology. 1994. p. 779–815.
129. Kabsch W. XDS. *Acta Crystallogr D Biol Crystallogr.* 2010;66:125–32.
130. McCoy AJ, Grosse-Kunstleve RW, Adams PD, Winn MD, Storoni LC, Read RJ. Phaser crystallographic software. *J Appl Crystallogr.* 2007;40(4):658–74.

131. Adams PD, Afonine P V., Bunkóczi G, Chen VB, Echols N, Headd JJ, et al. The Phenix software for automated determination of macromolecular structures. *Methods*. 2011;55(1):94–106.
132. Franke D, Petoukhov M V., Konarev P V., Panjkovich A, Tuukkanen A, Mertens HDT, et al. ATSAS 2.8: A comprehensive data analysis suite for small-angle scattering from macromolecular solutions. *J Appl Crystallogr*. 2017;50:1212–25.
133. Konarev P V., Volkov V V., Sokolova A V., Koch MHJ, Svergun DI. PRIMUS: A Windows PC-based system for small-angle scattering data analysis. *J Appl Crystallogr*. 2003;36(5):1277–82.
134. Svergun DI. Determination of the regularization parameter in indirect-transform methods using perceptual criteria. *J Appl Crystallogr*. 1992;25(pt 4):495–503.
135. Svergun DI. Restoring low resolution structure of biological macromolecules from solution scattering using simulated annealing. *Biophys J*. 1999;76(6):2879–86.
136. Petoukhov M V., Franke D, Shkumatov A V., Tria G, Kikhney AG, Gajda M, et al. New developments in the ATSAS program package for small-angle scattering data analysis. *J Appl Crystallogr*. 2012;45(2):342–50.
137. Volkov V V., Svergun DI. Uniqueness of ab initio shape determination in small-angle scattering. In: *Journal of Applied Crystallography*. 2003. p. 860–4.
138. Svergun D, Barberato C, Koch MH. CRY SOL - A program to evaluate X-ray solution scattering of biological macromolecules from atomic coordinates. *J Appl Crystallogr*. 1995;28(6):768–73.
139. Bach M, Grigat S, Pawlik B, Fork C, Utermöhlen O, Pal S, et al. Fast set-up of doxycycline-inducible protein expression in human cell lines with a single plasmid based on Epstein-Barr virus replication and the simple tetracycline repressor. *FEBS J*. 2007;274(3):783–90.
140. Dixon AS, Schwinn MK, Hall MP, Zimmerman K, Otto P, Lubben TH, et al. NanoLuc Complementation Reporter Optimized for Accurate Measurement of Protein Interactions in Cells. *ACS Chem Biol*. 2016 Feb 19;11(2):400–8.
141. Harris LA, Hogg JS, Tapia JJ, Sekar JAP, Gupta S, Korsunsky I, et al. BioNetGen 2.2: Advances in rule-based modeling. *Bioinformatics*. 2016;32(21):3366–8.
142. Mitra ED, Suderman R, Colvin J, Ionkov A, Hu A, Sauro HM, et al. PyBioNetFit and the Biological Property Specification Language. *iScience*. 2019;19:1012–36.
143. Zhang T, Inesta-Vaquera F, Niepel M, Zhang J, Ficarro SB, MacHleidt T, et al. Discovery of potent and selective covalent inhibitors of JNK. *Chem Biol*. 2012;19(1):140–54.
144. Szafranska AE, Dalby KN. Kinetic mechanism for p38 MAP kinase alpha. A partial rapid-equilibrium random-order ternary-complex mechanism for the phosphorylation of a protein substrate. *FEBS J*. 2005;272(18):4631–45.

145. Morton S, Davis RJ, Cohen P. Signalling pathways involved in multisite phosphorylation of the transcription factor ATF-2. *FEBS Lett.* 2004;572(1–3):177–83.
146. Tzarum N, Eisenberg-Domovich Y, Gills JJ, Dennis PA, Livnah O. Lipid molecules induce p38 α activation via a novel molecular switch. *J Mol Biol.* 2012 Dec 14;424(5):339–53.
147. Richardson JS, Richardson DC. Amino acid preferences for specific locations at the ends of alpha helices. *Science (80-)*. 1988 Jun 17;240(4859):1648 LP – 1652.
148. Hendus-Altenburger R, Lambrughi M, Terkelsen T, Pedersen SF, Papaleo E, Lindorff-Larsen K, et al. A phosphorylation-motif for tuneable helix stabilisation in intrinsically disordered proteins – Lessons from the sodium proton exchanger 1 (NHE1). *Cell Signal.* 2017;37(January):40–51.
149. Ouwens DM, De Ruiter ND, Van der Zon GCM, Carter AP, Schouten J, Van der Burgt C, et al. Growth factors can activate ATF2 via a two-step mechanism: Phosphorylation of Thr71 through the Ras-MEK-ERK pathway and of Thr69 through RaIGDS-Src-p38. *EMBO J.* 2002;21(14):3782–93.
150. Horesh D, Sapir T, Francis F, Wolf SG, Caspi M, Elbaum M, et al. Doublecortin, a stabilizer of microtubules. *Hum Mol Genet.* 1999;8(9):1599–610.
151. Kirsch K, Zeke A, Tóke O, Sok P, Sethi A, Sebó A, et al. Co-regulation of the transcription controlling ATF2 phosphoswitch by JNK and p38. *Nat Commun.* 2020;11(1):1–15.
152. Rao T, Ruiz-Gómez G, Hill TA, Hoang HN, Fairlie DP, Mason JM. Truncated and Helix-Constrained Peptides with High Affinity and Specificity for the cFos Coiled-Coil of AP-1. *PLoS One.* 2013;8(3):1–12.
153. Yadahalli S, Neira JL, Johnson CM, Tan YS, Rowling PJE, Chattopadhyay A, et al. Kinetic and thermodynamic effects of phosphorylation on p53 binding to MDM2. *Sci Rep.* 2019;9(1):1–15.
154. Lau YH, De Andrade P, Quah ST, Rossmann M, Laraia L, Sköld N, et al. Functionalised staple linkages for modulating the cellular activity of stapled peptides. *Chem Sci.* 2014;5(5):1804–9.
155. Hazzalin CA, Mahadevan LC. MAPK-Regulated transcription: A continuously variable gene switch? Vol. 3, Nature Reviews Molecular Cell Biology. 2002. p. 30–40.
156. Gille H, Strahl T, Shaw PE. Activation of ternary complex factor Elk-1 by stress-activated protein kinases. *Curr Biol.* 1995;5(10):1191–200.
157. Marinissen MJ, Chiariello M, Pallante M, Gutkind JS. A Network of Mitogen-Activated Protein Kinases Links G Protein-Coupled Receptors to the c-*jun* Promoter: a Role for c-Jun NH₂-Terminal Kinase, p38s, and Extracellular Signal-Regulated Kinase 5. *Mol Cell Biol.* 1999;19(6):4289–301.

158. Panne D, Maniatis T, Harrison SC. Crystal structure of ATF-2/c-Jun and IRF-3 bound to the interferon- β enhancer. *EMBO J*. 2004;23(22):4384–93.
159. Chen L, Glovert JNM, Hogan PG, Rao A, Harrison SC. Structure of the DNA-binding domains from NFAT, Fos and Jun bound specifically to DNA. *Nature*. 1998;392(6671):42–8.
160. Sano Y, Akimaru H, Okamura T, Nagao T, Okada M, Ishii S. Drosophila activating transcription factor-2 is involved in stress response via activation by p38, but not c-Jun NH(2)-terminal kinase. *Mol Biol Cell*. 2005 Jun;16(6):2934–46.
161. Seong KH, Li D, Shimizu H, Nakamura R, Ishii S. Inheritance of stress-induced, ATF-2-dependent epigenetic change. *Cell*. 2011 Jun 24;145(7):1049–61.
162. Shiozaki K, Russell P. Conjugation, meiosis, and the osmotic stress response are regulated by Spc1 kinase through Atf1 transcription factor in fission yeast. *Genes Dev*. 1996;10(18):2276–88.
163. Lynch VJ, Wagner GP. Resurrecting the role of transcription factor change in developmental evolution. *Evolution (N Y)*. 2008;62(9):2131–54.
164. Galant R, Carroll SB. Evolution of a transcriptional repression domain in an insect Hox protein. *Nature*. 2002;415(6874):910–3.
165. Lynch VJ, May G, Wagner GP. Regulatory evolution through divergence of a phosphoswitch in the transcription factor CEBPB. *Nature*. 2011;480(7377):383–6.
166. Neduva V, Russell RB. Linear motifs: Evolutionary interaction switches. *FEBS Lett*. 2005;579(15):3342–5.
167. Lee S, Rauch J, Kolch W. Targeting MAPK signaling in cancer: Mechanisms of drug resistance and sensitivity. Vol. 21, International Journal of Molecular Sciences. MDPI AG; 2020.
168. Kocieniewski P, Faeder JR, Lipniacki T. The interplay of double phosphorylation and scaffolding in MAPK pathways. *J Theor Biol*. 2012;295:116–24.

10. Publication list

Publications related to the doctoral thesis

- ◆ **Kirsch K**, Zeke A, Tóke O, Sok P, Sethi A, Sebő A, Kumar GS, Egri P, Póti ÁL, Gooley P, Peti W, Bento I, Alexa A, Reményi A. Co-regulation of the transcription controlling ATF2 phosphoswitch by JNK and p38. *Nat Commun.* 2020 Nov 13;11(1):5769. doi: 10.1038/s41467-020-19582-3. PMID: 33188182PMCID: PMC7666158.
- ◆ Zeke A, Bastys T, Alexa A, Garai Á, Mészáros B, **Kirsch K**, Dosztányi Z, Kalinina OV, Reményi A. Systematic discovery of linear binding motifs targeting an ancient protein interaction surface on MAP kinases. *Mol Syst Biol.* 2015 Nov 3;11(11):837. doi: 10.15252/msb.20156269. PMID: 26538579; PMCID: PMC4670726.

Other publications

- ◆ Sok P, Gógl G, Kumar GS, Alexa A, Singh N, **Kirsch K**, Sebő A, Drahos L, Gáspári Z, Peti W, Reményi A. MAP Kinase-Mediated Activation of RSK1 and MK2 Substrate Kinases. *Structure.* 2020 Oct 6;28(10):1101-1113.e5. doi: 10.1016/j.str.2020.06.007. Epub 2020 Jul 9. PMID: 32649858; PMCID: PMC7544624.
- ◆ **Kirsch K**, Sok P, Reményi A. Structural Reconstruction of Protein-Protein Complexes Involved in Intracellular Signaling. *Adv Exp Med Biol.* 2016;896:315-26. doi: 10.1007/978-3-319-27216-0_20. PMID: 27165334. (book chapter)
- ◆ Kovács Z, Simon-Sarkadi L, Sovány C, **Kirsch K**, Galiba G, Kocsy G. Differential effects of cold acclimation and abscisic acid on free amino acid composition in wheat. *Plant Sci.* 2011 Jan;180(1):61-8. doi: 10.1016/j.plantsci.2010.08.010. Epub 2010 Aug 26. PMID: 21421348.

Conference attendances

- ◆ **Kirsch K**, Zeke A, Sok P, Reményi A. Phospho-switches in the MAP kinase pathway - a case study of ATF2. *From Protein Complexes to Cell-Cell Communication Conference 2019*, Esztergom, Hungary (selected talk)
- ◆ **Kirsch K**, Zeke A, Reményi A. Exploring the binding mechanism of the ATF2 transcription factor to the JNK mitogen activated protein kinase. *Interdisciplinary Signaling Workshop 2014*, Visegrád, Hungary (poster presentation)

11. Appendix

Appendix Table 1. Crystallographic data collection and refinement statistics

	JNK-ATF2(19-58)	pp-p38-ATF2(83-102)	JNK-DCX(342-366)
Data collection			
Space group	P 1 21 1	P 2 21 21	C 1 2 1
Cell dimensions			
<i>a</i> , <i>b</i> , <i>c</i> (Å)	57.23 110.40 77.63	39.40 84.60 122.53	236.71 135.56 62.97
α , β , γ (°)	90.00 94.39 90.00	90.00 90.00 90.00	90.00 91.64 90.00
Resolution range (Å)	44.94 - 2.70	69.62 - 1.95	44.68 - 3.50
CC _{1/2}	99.6 (86.8)	99.9 (42.5)	99.7(78.2)
<i>R</i> _{merge} †	6.2 (43.0)	7.8 (146.4)	12.8(107.7)
$\langle I/\sigma(I) \rangle$	10.3 (2.4)	17.8 (1.1)	9.4(2.0)
Completeness (%)	91.4	98.9	99.9
Redundancy	3.3	12.5	6.9
No. reflections	23961	30380	25107
Refinement			
<i>R</i> _{work} / <i>R</i> _{free}	0.182 , 0.256	0.186, 0.220	0.215, 0.257
No. atoms			
Protein	5971	2886	8773
Ligand/ion	6	1	9
Solvent	125	351	0
B-factors (Å ²)			
Protein	77.5	43.32	147.2
Ligand	49.7	34.96	120.4
Solvent	66.1	52.94	75.3
<i>Ramachandran</i>			
Favored (%)	95	98	96
Allowed (%)	5	2	4
Outliers (%)	0	0	0
Rotamer outliers (%)	4	0	0
R.m.s deviations			
Bond lengths (Å)	0.012	0.008	0.004
Bond angles (°)	1.376	1.085	0.70
PDB ID	6ZR5	6ZQS	-

$$\dagger R_{\text{merge}} = \frac{\sum_{\text{hkl}} \sum_i |I_i(\text{hkl}) - \langle I(\text{hkl}) \rangle|}{\sum_{\text{hkl}} \sum_i I_i(\text{hkl})}$$

Appendix Code. Model of ATF2 activation by JNK and p38 written in BioNetGen language

```

begin model
begin parameters
kon1 5.6           #WT: 5.6 JNK binding to ATF2 [uM-1*s-1]
koff1 19.6        #JNK release from ATF2 [s-1]
kon2 17.2         #WT: 17.2, S90N: 77.1, MUT4: 1.2 #p38 binding to both ATF2 sites [uM-1*s-1]
koff2 429        #p38 release from both ATF2 sites [s-1]
kon3 0.429       #WT: 0.429 p38 binding only at ATF2 D-site [uM-1*s-1]
koff3 429        #p38 release only from ATF2 D-site [s-1]
k1 3.52          #CTR: 3.52, JNKIN8: 0 #JNK activity on T71->pT71 and T69->pT69 [s-1]
k2 0.78          #CTR: 0.78, JNKIN8: 0, S90N: 0 #JNK activity on F-site (S90) [s-1]
k3 8.2           #p38 activity on T71->pT71, T69->pT69 and T69pT71->pT69pT71 [s-1]
k4 1.67          #p38 activity on pT69T71->pT69pT71 [s-1]
kstim7 0.00009074 #MKK7 activity on JNK [s-1]
dp1 0.000626     #phosphatase activity on pp-JNK [s-1]
kstim6 0.000116  #MKK6 activity on p38 [s-1]
dp2 0.00176     #phosphatase activity on pp-p38 [s-1]
dp3 0.00954     #phosphatase activity on ATF2 pT69 and pT71 [s-1]
dp4 0.00450     #phosphatase activity on ATF2 pS90 [s-1]
totJNK 1         #total concentration of JNK species [uM]
totp38 2.65     #total concentration of p38 species [uM]
totATF2 1        #total concentration of ATF2 species [uM]
end parameters

begin molecule types
JNK(DRS,TY-0-p)
p38(DRS,FRS,TY-0-p)
ATF2(D,T71-0-p,T69-0-p,F-0-p)
end molecule types

begin seed species
JNK(DRS,TY-0) totJNK
p38(DRS,FRS,TY-0) totp38
ATF2(D,T71-0,T69-0,F-0) totATF2
end seed species

begin observables
Molecules pT69pT71 ATF2(T71-p,T69-p)
Molecules p38ATF2all p38(DRS!2,FRS!3,TY-p).ATF2(D!2,F-0!3),p38(DRS!2,FRS,TY-0).ATF2(D!2,F),p38(DRS!2,FRS,TY-p).ATF2(D!2,F-p)
Molecules ppp38 p38(TY-p)
Molecules ppJNK JNK(TY-p)
end observables

begin reaction rules
#JNK and p38 phosphorylation and dephosphorylation, when it is not bound to ATF2
JNK(DRS,TY-0) -> JNK(DRS,TY-p) kstim7
JNK(DRS,TY-p) -> JNK(DRS,TY-0) dp1
p38(DRS,FRS,TY-0) -> p38(DRS,FRS,TY-p) kstim6
p38(DRS,FRS,TY-p) -> p38(DRS,FRS,TY-0) dp2

#JNK-ATF2 binding
JNK(DRS) + ATF2(D) <-> JNK(DRS!1).ATF2(D!1) kon1,koff1

#JNK-ATF2 phosphorylation
JNK(DRS!1,TY-p).ATF2(D!1,T71-0,T69-0) -> JNK(DRS!1,TY-p).ATF2(D!1,T71-p,T69-0) k1
JNK(DRS!1,TY-p).ATF2(D!1,T71-p,T69-0) -> JNK(DRS!1,TY-p).ATF2(D!1,T71-0,T69-0) k1
JNK(DRS!1,TY-p).ATF2(D!1,T71-0,T69-0) -> JNK(DRS!1,TY-p).ATF2(D!1,T71-0,T69-p) k1
JNK(DRS!1,TY-p).ATF2(D!1,T71-0,T69-p) -> JNK(DRS!1,TY-p).ATF2(D!1,T71-p,T69-p) k1
JNK(DRS!1,TY-p).ATF2(D!1,F-0) -> JNK(DRS!1,TY-p).ATF2(D!1,F-p) k2

#p38-ATF2 binding at both sites
p38(DRS,FRS,TY-p) + ATF2(D,F-0) <-> p38(DRS!2,FRS!3,TY-p).ATF2(D!2,F-0!3) kon2,koff2

#p38-ATF2 binding only at D-site
p38(DRS,FRS,TY-0) + ATF2(D,F) <-> p38(DRS!2,FRS,TY-0).ATF2(D!2,F) kon3,koff3
p38(DRS,FRS,TY-p) + ATF2(D,F-p) <-> p38(DRS!2,FRS,TY-p).ATF2(D!2,F-p) kon3,koff3

#p38-ATF2 phosphorylation - when binds both sites
p38(DRS!2,FRS!3,TY-p).ATF2(D!2,T71-0,T69-0,F-0!3) -> p38(DRS!2,FRS!3,TY-p).ATF2(D!2,T71-p,T69-0,F-0!3) k3
p38(DRS!2,FRS!3,TY-p).ATF2(D!2,T71-p,T69-0,F-0!3) -> p38(DRS!2,FRS!3,TY-p).ATF2(D!2,T71-0,T69-p,F-0!3) k3
p38(DRS!2,FRS!3,TY-p).ATF2(D!2,T71-0,T69-p,F-0!3) -> p38(DRS!2,FRS!3,TY-p).ATF2(D!2,T71-0,T69-p,F-0!3) k3
p38(DRS!2,FRS!3,TY-p).ATF2(D!2,T71-0,T69-p,F-0!3) -> p38(DRS!2,FRS!3,TY-p).ATF2(D!2,T71-p,T69-p,F-0!3) k4

#p38-ATF2 phosphorylation - when binds only D-site
p38(DRS!2,FRS,TY-p).ATF2(D!2,T71-0,T69-0,F-p) -> p38(DRS!2,FRS,TY-p).ATF2(D!2,T71-p,T69-0,F-p) k3
p38(DRS!2,FRS,TY-p).ATF2(D!2,T71-p,T69-0,F-p) -> p38(DRS!2,FRS,TY-p).ATF2(D!2,T71-0,T69-p,F-p) k3
p38(DRS!2,FRS,TY-p).ATF2(D!2,T71-0,T69-0,F-p) -> p38(DRS!2,FRS,TY-p).ATF2(D!2,T71-0,T69-p,F-p) k3
p38(DRS!2,FRS,TY-p).ATF2(D!2,T71-0,T69-p,F-p) -> p38(DRS!2,FRS,TY-p).ATF2(D!2,T71-p,T69-p,F-p) k4

#ATF2 dephosphorylation
ATF2(T71-p) -> ATF2(T71-0) dp3
ATF2(T69-p) -> ATF2(T69-0) dp3
ATF2(F-p) -> ATF2(F-0) dp4
end reaction rules
end model

# generate reaction network
generate_network({overwrite=>1})
# Equilibration
setParameter("kstim7",0.000004695); # keq7
setParameter("kstim6",0.0000174); # keq6
simulate({prefix=>"01",method=>"ode",t_start=>-20000,t_end=>0,n_steps=>10});
# Stimulation
setParameter("kstim7",0.00009074);
setParameter("kstim6",0.000116);
simulate({prefix=>"01",method=>"ode",t_start=>0,t_end=>2400,n_steps=>2400})

```

Appendix Table 2. Fitted parameters of the in silico model

unit	parameter	WT	WT +JNKi	S90N	S90N +JNKi	MUT4	fitted from
$\mu\text{M}^{-1}\text{s}^{-1}$	kon1	5.6	*	*	*	*	in vitro
s^{-1}	koff1	19.6	*	*	*	*	in vitro
$\mu\text{M}^{-1}\text{s}^{-1}$	kon2	17.2	*	4.5x ^a	4.5x ^a	0.07x ^b	in vitro
s^{-1}	koff2	429	*	*	*	*	in vitro
$\mu\text{M}^{-1}\text{s}^{-1}$	kon3	0.429	*	*	*	*	assumption ^c
s^{-1}	koff3	429	*	*	*	*	assumption ^c
s^{-1}	k1	3.52	0	*	0	*	in vitro
s^{-1}	k2	0.78	0	0	0	*	in vitro
s^{-1}	k3	8.2	*	*	*	*	in vitro
s^{-1}	k4	1.67	*	*	*	*	in vitro
s^{-1}	keq7	4.70E-06	*	*	*	*	WB
s^{-1}	kstim7	9.07E-05	*	*	*	*	WB
s^{-1}	dp1	6.26E-04	*	*	*	*	WB
s^{-1}	keq6	1.74E-05	*	*	*	*	NanoBit
s^{-1}	kstim6	1.16E-04	*	*	*	*	NanoBit
s^{-1}	dp2	1.76E-03	*	*	*	*	NanoBit
s^{-1}	dp3	9.54E-03	*	*	*	*	WB
s^{-1}	dp4	4.50E-03	*	*	*	*	NanoBit
μM	totJNK	1	*	*	*	*	assumption ^d
μM	totp38	2.65	*	*	*	*	estimated from WB ^e
μM	totATF2	1	*	*	*	*	assumption ^d

* same as in WT

^a based on Ki values determined in vitro (Fig. 4b)

^b based on enzyme kinetic data (Fig. 3c)

^c based on enzyme kinetic data of the phosphorylation of ATF2(19-83) construct (0.5-100 μM) by p38. MM curve cannot be fitted in the applied concentration range, therefore binding affinity was assumed to be 1 mM. koff3 was set to the same as koff2.

^d based on ref[168]

^e To measure the NanoBit signal for p38-ATF2 TAD binding, cells were transfected with a heterologous p38 construct that increased the total in-cell concentration of the p38 enzyme. This was estimated based on quantitative WB data and heterologous p38 level was ~ 1.65 fold of the endogenous (which was assumed to be 1 μM).

in vitro: fitted to in vitro enzyme kinetics (quantitative dot-blot or phosphorimaging)

WB: fitted to cell-based Western-blot

NanoBit: fitted to in-cell luciferase complementation based protein-protein interaction data

Appendix Table 3. List of primers.

Primer name	Primer sequence (5'-3')
PCR primers for E.coli constructs	
ATF2-19-BamHI-Fw	CTGGGATCCATGAGTGATGACAAACCCTTTCTATGTACTGC
ATF2-100-NotI-Rev	TTTTTAAT GCGGCCGCT TGAAGCTTTCTTGAATTCATTCTCAAATGG
ATF2-78-NotI-Rev	AAACCCAC GCGGCCGCT GTTTTTCAAGAATCTTGTGGTGTGGGG
ATF2-58-NotI-Rev	ATTAGACT GCGGCCGCT TGCTGGACCAAATTCAGTGTCTATCTC
ATF2-50-NotI-Rev	CCAAATTT GCGGCCGCT CTCATGTTTATGTTTATGGACAGCCAAATGATCC
ATF2-Y-19-BamHI-Fw	TTATTAGGATCCATAGTGATGACAAACCCTTTCTATGTACTGC
ATF2-58-XhoI-Rev	TATTTACTCGAGTCACTATGCTGGACCAAATTCAG
cJUN-1-BamHI-Fw	TTATTAGGATCCATGACTGCAAAGATGGAAACGACCTTCTATGACG
cJUN-78-NotI-Rev	ATTAAATTGCGGCCGCTGCGCTCCAGCTCGGGC
ATF2-59-Not1-Fw	ATTAAATTGCGGCCGCAATGACAGTGTCAATTGTGGC
ATF2-100-XhoI-Rev	TAATATCTCGAGTGAAGCTTTCTTGAATTCATTCTCAAATGG
ATF2-78-XhoI-Rev	TTATATCTCGAGTCAGTTTTTCAAGAATCTTGTGGTGTGGGG
ATF2-100-MUT4-NotI-Rev	TTATATTAGCGGCCGCTTGAAGCTTTCTTGGCTTCATTCTCAGCTGGACTCGC CAACTC
ATF2-106-XhoI-Rev	TATTAECTCGAGTCACTATTTTTTAATGTCATCTTCTGAAGCTTTCTTG
ATF2-19-CACA-BamHI-Fw	TTATTAGGATCCATGAGTGATGACAAACCCTTTCTAGCTACTGCGCCTGGAG CTGGCC
ATF2-90-NotI-Rev	TATTTATAGCGGCCGCTACTCGCCAACTCATTAAACAAACCC
ATF2-83-NotI-Rev	TATATATGCGGCCGCTACCCACTTCTTCACAGTTTTTCAAG
ATF2-83-XhoI-Rev	TATTTACTCGAGACCCACTTCTTCACAGTTTTTCAAG
DCX-1-SalI-Fw	TAATTAGTCGACATGGAACCTTGATTTTGGACACTTTGACG
DCX-366-NotI-Rev	ATTAAATTGCGGCCGCCATGGAATCACCAAGCGAGTCCG
DCX-49-SalI-Fw	TTATTAGTCGACGAGAAGAAAGCCAAGAAGGTACGT
DCX-150-NotI-Rev	ATTAAATTGCGGCCGCTTACGTTGACAGACCAGTTGGGATTGAC
DCX-287-NotI-Rev	ATTAAATTGCGGCCGCCGATGCCTTTGGGCCAGC
DCX-286-BamHI-Fw	TTATTAGGATCCGCATCCCCAACACCTCAGAAGAC
DCX-dC23-XhoI-Rev	CAGACTCGAGGAGGCTGCCAGGACTGGTG
DCX-170-SalI-Fw	TTATTAGTCGACGCCAGGGAGAACAAGGACTTTGTG
DCX-264-NotI-Fw	ATTAAATTGCGGCCGCTTTTCTCTGGATGAAAATGAATGCCG
DCX-366-XhoI-Rev	TAATATCTCGAGCATGGAATCACCAAGCGAGTCCG
Oligos for annealed oligo cloning (with BamHI/NotI sites)	
pepATF2(23-55)-Fw1	GATCCAAACCGTTTCTGTGCACCGCCCCGGGCTGCGGCCAGCGCTTACCA ACGA

pepATF2(23-55)-Fw2	AGATCATCTGGCCGTGCATAAACATAAACATGAAATGACCCTGAAATTTGGCAGC
pepATF2(23-55)-Rev1	GGCCGCTGCCAAATTCAGGGTCATTTTCATGTTTATGTTT
pepATF2(23-55)-Rev2	ATGCACGGCCAGATGATCTTCGTTGGTAAAGCGCT
pepATF2(23-55)-Rev3	GGCCGCAGCCCGGGGCGGTGCACAGAAACGGTTTG
pepATF2(23-50)-Fw1	GATCCAAACCGTTTCTGTGCACCGCCCCGGGCTGCGGCCAGCGCTTTACCAACGA
pepATF2(23-50)-Fw1	AGATCATCTGGCCGTGCATAAACATAAACATGAAAGC
pepATF2(23-50)-Rev1	GGCCGCAGCCCGGGGCGGTGCACAGAAACGGTTTG
pepATF2(23-50)-Rev2	GGCCGCTTTCATGTTTATGTTTATGCACGGCCAGATGATCTTCGTTGGTAAAGCGCT
pepATF2(42-55)-Fw1	GATCCCTGGCCGTGCATAAACATAAACATGAAA
pepATF2(42-55)-Fw2	TGACCCTGAAATTTGGCAGC
pepATF2(42-55)-Rev1	ATGCACGGCCAGG
pepATF2(42-55)-Rev2	GGCCGCTGCCAAATTCAGGGTCATTTTCATGTTTATGTTT
pepATF2(81-95)-Fw	GATCCGAAGTGGGTCTGTTTAAACGAACTGGCCAGCCCGTTTGAAAACGAAAGC
pepATF2(81-95)-Rev	GGCCGCTTTCGTTTTCAAACGGGCTGGCCAGTTCGTAAACAGACCCACTTCG
pepMEF2A-Fw	GATCCAGTAGGAAACCAGATCTTCGAGTTGTCATCCCCCTTCAAGCGC
pepMEF2A-Rev	GGCCGCGCTTGAAGGGGGATGACAACTCGAAGATCTGGTTTCCTACTG
pepDCX-Ct23-Fw1	GATCCCGTAAGCATAAAGTAGACCTCT
pepDCX-Ct23-Fw2	ATCTTCCACTGAGTCTTGACGACTCGGACTCGCTTGGTGATTCCATGAGC
pepDCX-Ct23-Rev1	GGCCGCTCATGGAATCACCAAGCGAG
pepDCX-Ct23-Rev2	TCCGAGTCGTCAAGACTCAGTGGAAGATAGAGGTCTACTTTATGCTTACGG
PCR primers for NanoBit assay	
ATF2-19-XhoI-Fw	TTATCTCTCGAGCGGTATGAGTGATGACAAACCCTTTCTATGTAC
ATF2-100-NheI-Rev	TATTTAGCTAGCTGAAGCTTCTTGAATTCATTCTCAAATGGAC
ATF2-MUT1-Rev	ATTAAGCTAGCTGAAGCTTCTTGAATTCATTCTCAAATGGACTCGCCGCTCATTAGCCAAACCCACTTC
ATF2-MUT2-Rev	TTATATGCTAGCTGAAGCTTCTTGAATTCATTCTCAGCTGGACTCGCC
ATF2-MUT3-Rev	TATTTAGCTAGCTGAAGCTTCTTGGCTTCATTCTCAAATGGACTCGC
ATF2-MUT4-Rev	TATAATGCTAGCTGAAGCTTCTTGGCTTCATTCTCAGCTGGACTCGCCAACTC
ATF2-MUT Δ -Rev	TATTTAGCTAGCTGAAGCTTCTTGAATTCATTCTCAAATGGACTCGCACAGTTTTTCAAGAATCTTGTTGGTGTGGGG
ATF2-90-Rev	TATTTAGCTAGCACTCGCCAACTCATTAACAAACCC
DCX-1-XbaI-Fw	TTAATTTCTAGAATGGAACCTGATTTTGGACACTTTGACG
DCX-366-XhoI-Rev	TATTTACTCGAGCCCATGGAATCACCAAGCGAGTCCG
DCX-dC23-XhoI-Rev	TATATTCTCGAGCCGAGGCTGCCAGGACTGGTGG

PCR primers for GAL4 assay	
GAL4-ATF2-19-BamHI-Fw	TATTTAGGATCCCAATGAGTGATGACAAACCCTTTCTATGTAC
GAL4-ATF2-100-NotI-Rev	TATTTATAGCGGCCGCTGAAGCTTTCTTGAATTCATTCTCAAATGG
GAL4-ATF2-19-CACA-BamHI-Fw	TATATAGGATCCCAATGAGTGATGACAAACCCTTTCTAGCTAC
Primers for HT-MKK7-MLK3 and HT-MKK6EE	
MKK7-HindIII-Fw	CTTAAGCTTGCCACCATGGCGGCGTCCTCCCTGGAAC
MKK7-BamHI-Rev	CCACCAGCACTGGATCCCCTGAAGAAGGGCAGGTGGGGC
linker-MLK3-BamHI-Fw	AGGGGATCCAGTGCTGGTGGTAGTGCTGGTGGTAGTGCTGGTGGTAGTGCTGGTGGTAGTGCTGGTGGTCTGCGGCTGGAGGAGGTGATC
MLK3-XhoI-Rev	TTGCTCGAGCAGCGCCTCCAACCTGCTGCAGGAT
MKK6-HindIII-Fw	TATTTAAAGCTTGCCACCATGTCTCAGTCGAAAGGCAAGAAGCG
MKK6-NotI-Rev	TATTATTTAGCGGCCGCTGTCTCCAAGAATCAGTTTTACAAAAGATGC
Primers for BiFC assay	
ATF2-1-BamHI-Fw	TTATTAGGATCCATGAAATTCAGTTACATGTGAATTCTGCCAGGC
ATF2-505-NotI-Rev	ATTAAATTGCGGCCGCTACTTCCTGAGGGCTGTGACTGG
c-JUN-1-BamHI-Fw	TTATTAGGATCCATGACTGCAAAGATGGAAACGACCTTCTATGACG
c-JUN-331-NotI-Rev	ATTAAATTGCGGCCGCTAAATGTTTGCAACTGCTGCGTTAGCATGAG
Mutagenesis primers	
ATF2-K48E-Fwd	GGATCATTTGGCTGTCCATAAACATGAACATGAGATGACACTGAAATTTGGTCC
ATF2-K48E-Rev	GGACCAAATTTTCAGTGTCATCTCATGTTCATGTTTATGGACAGCCAAATGATCC
cJUN-K35E-Fw	CTACAGTAACCCCAAGATCCTGGAACAGAGCATGACCCTGAACCTGGCC
cJUN-K35E-Rev	GGCCAGGTTTCAGGGTCATGCTCTGTTCCAGGATCTTGGGGTTACTGTAG
ATF2-K48A-Fwd	GGATCATTTGGCTGTCCATAAACATGCACATGAGATGACACTGAAATTTGGTCC
ATF2-K48A-Rev	GGACCAAATTTTCAGTGTCATCTCATGTGCATGTTTATGGACAGCCAAATGATCC
ATF2-V44A-Fw	CGAGGATCATTTGGCTGCCATAAACATAAACATGAGATGAC
ATF2-V44A-Rev	GTCATCTCATGTTTATGTTTATGGGCAGCCAAATGATCCTCG
ATF2-V44E-Fw	CGAGGATCATTTGGCTGAGCATAAACATAAACATGAGATGAC
ATF2-V44E-Rev	GTCATCTCATGTTTATGTTTATGCTCAGCCAAATGATCCTCG
ATF2-H47E-Fw	GGATCATTTGGCTGTCCATAAAGAGAAACATGAGATGACACTGAAATTTGG
ATF2-H47E-Rev	CCAAATTTTCAGTGTCATCTCATGTTTCTCTTTATGGACAGCCAAATGATCC
ATF2-H47R-Fw	GGATCATTTGGCTGTCCATAAACGTAAACATGAGATGACACTGAAATTTGG
ATF2-H47R-Rev	CCAAATTTTCAGTGTCATCTCATGTTTACGTTTATGGACAGCCAAATGATCC
ATF2-Q34R-Fw	GCCTGGATGTGGCCGGCGTTTTACCAACGAGG

ATF2-Q34-Rev	CCTCGTTGGTAAAACGCCGGCCACATCCAGGC
ATF2-CACA-Rev	GTAAAACGCTGGCCAGCTCCAGGCGCAGTAGCTAGAAAGGGTTTGTTCATCA C
ATF2-L53E-Fw	CCATAAACATAAACATGAGATGACAGAGAAATTTGGTCCAGCACG
ATF2-L53E-Rev	CGTGCTGGACCAAATTTCTCTGTCATCTCATGTTTATGTTTATGG
ATF2-T69AT71A-Fw	GTCATTGTGGCTGATCAGGCCCCAGCACCAACAAGATTCTTGAAAAAC
ATF2-T69AT71A-Rev	GTTTTTCAAGAATCTTGTGGTGGCTGGGGCCTGATCAGCCACAATGAC
ATF2-S90A-Fw	GTTTGTTTAATGAGTTGGCGGCTCCATTTGAGAATGAATTCAAG
ATF2-S90A-Rev	CTTGAATTCATTCTCAAATGGAGCCGCCAATCATTAAACAAAC
ATF2-S90N-Fw	GTTTGTTTAATGAGTTGGCGAATCCATTTGAGAATGAATTCAAG
ATF2-S90N-Rev	CTTGAATTCATTCTCAAATGGATTCGCCAACTCATTAAACAAAC
MKK6-EE-Fw	GTGGCTACTTGGTGGACGAGGTTGCTAAAGAAATTGATGCAGGTTGCAAAC C
MKK6-EE-Rev	GGTTTGCAACCTGCATCAATTTCTTTAGCAACCTCGTCCACCAAGTAGCCAC

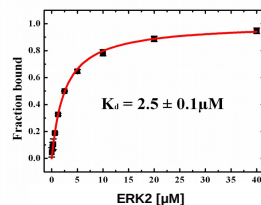
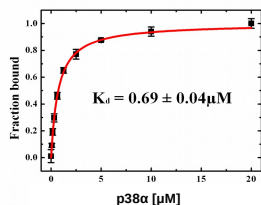
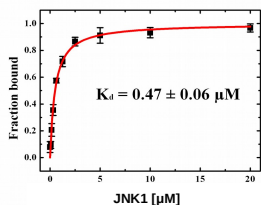
Appendix Figure 1. Fluorescence polarization measurements

A

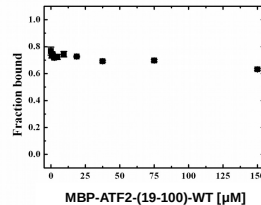
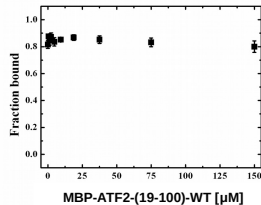
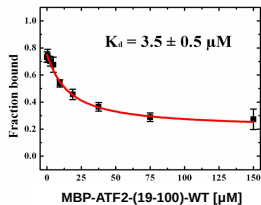
JNKβ1
CF-evJIP

p38α
CF-RHDF1

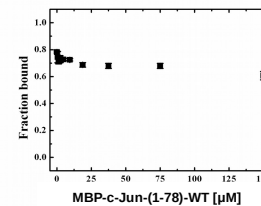
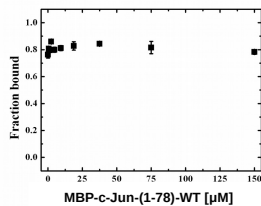
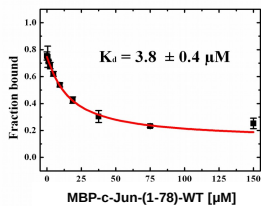
ERK2
CF-RHDF1



ATF2

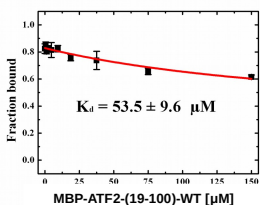


c-Jun

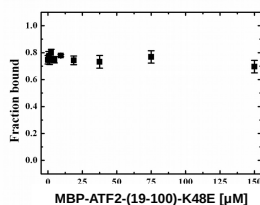


JNKβ1
CF-evJIP

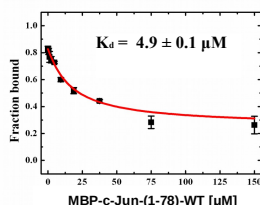
ATF2 + EDTA



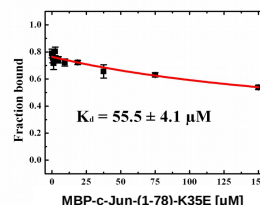
ATF2-K48E



c-Jun + EDTA

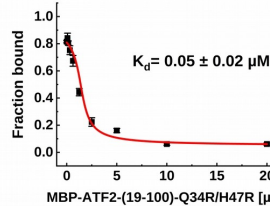
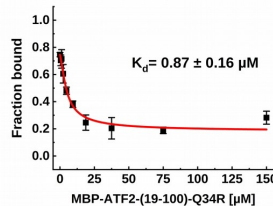
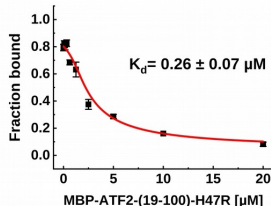
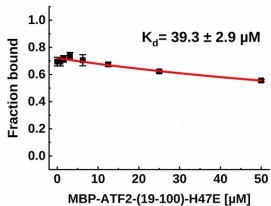
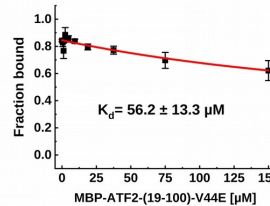
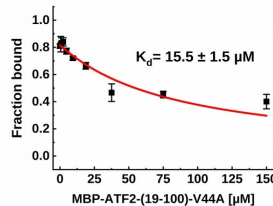
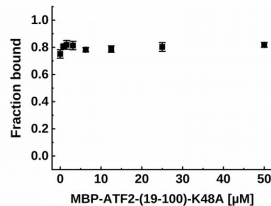


c-JUN-K35E



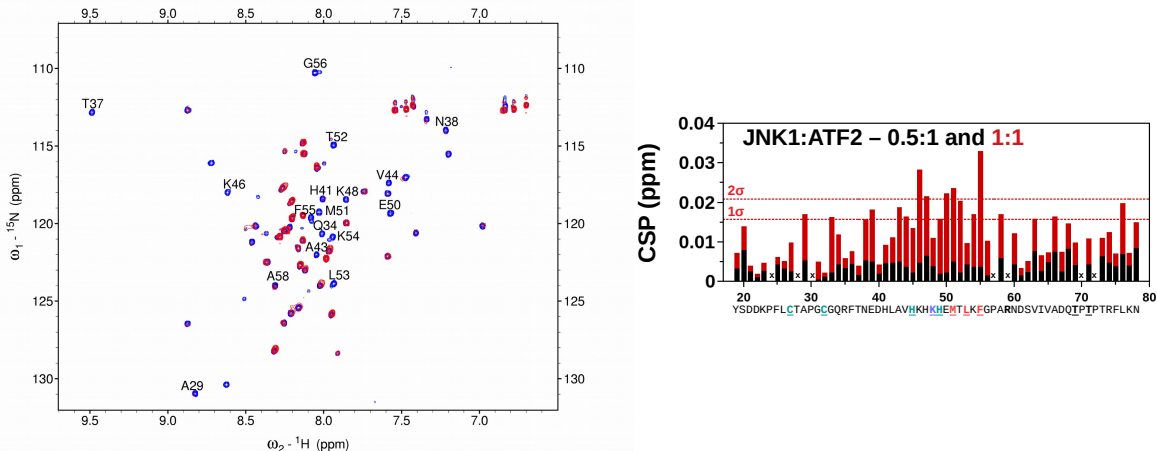
B

other ATF2 mutants

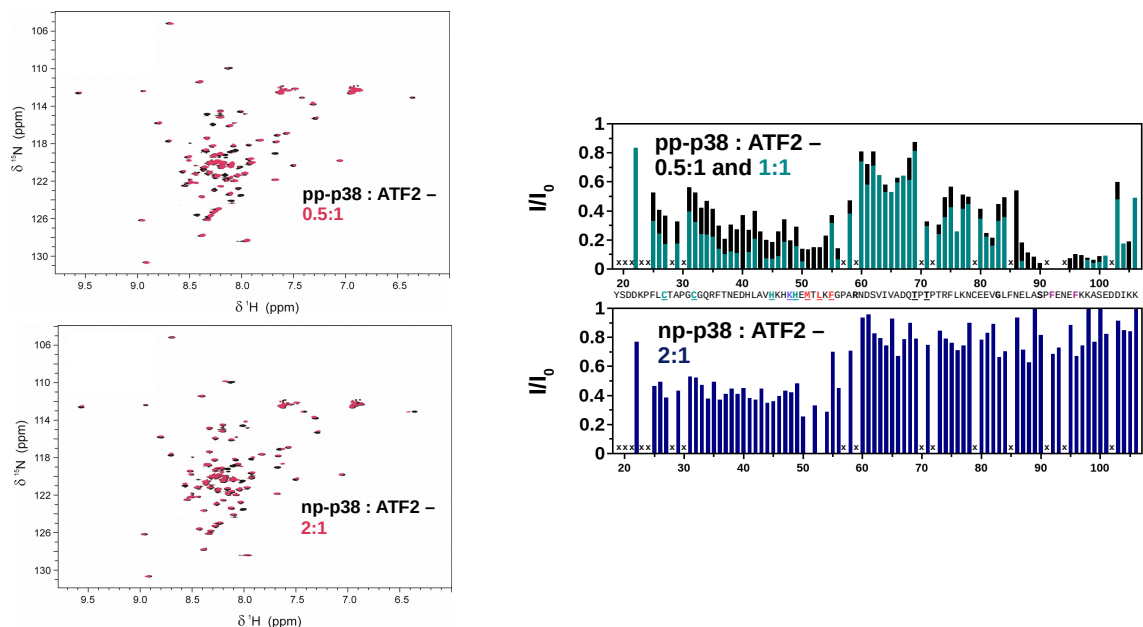


Appendix Figure 2. Nuclear magnetic resonance (NMR) studies

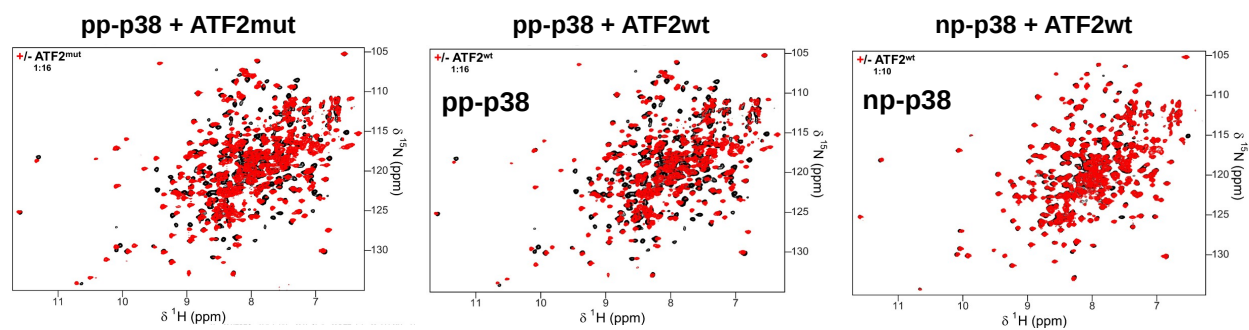
A ^{15}N -ATF2(19-78) + JNK1



B ^{15}N -ATF2(19-106) + pp-p38 / np-p38



C ^2H , ^{15}N -pp-p38 / np-p38 + ATF2(83-102) (SPFENEF) wt and mut (S90N)



Appendix Figure 1. Fluorescence polarization measurements

A) The first row shows the direct titration curves of MAPKs with a fluorescently labeled reporter docking peptide (CF-evJIP or CF-RHDF1). The following panels show competitive titrations with purified MBP-ATF2(19-100)-WT or MBP-cJUN(1-78)-WT (wild-type), EDTA treated WT and lysine mutant constructs. B) Competitive titration curves with different MBP-ATF2(19-100) mutants. Data were fit to a competition binding equation and errors indicate uncertainty in the fit. Error bars on the binding isotherms show SD based on three independent measurements (n=3). Data points are represented as mean values +/- SD.

Appendix Figure 2. Nuclear magnetic resonance (NMR) studies

A) Interaction region mapping of ATF2-JNK1. HSQC spectra of the 50 μM ^{15}N -labeled ATF2(19-58) construct (blue: apo ATF2, red: JNK1-ATF2, 1:1 molar ratio). $^1\text{H}/^{15}\text{N}$ amide resonances of residues where $I/I_0 < 0.1$ are labeled. Histogram shows the $^1\text{H}/^{15}\text{N}$ chemical shift perturbations (CSPs) vs. residue number with (0.5:1 (black) and 1:1 (red) JNK:ATF2 molar ratio) in the right. 'x' indicates resonances of residues which are not resolved in the spectra therefore could not be quantified or proline. B) Interaction region mapping of ATF2-p38. pp-p38 was mixed with 100 μM N^{15} -labelled ATF2(19-106) in two different molar ratio and intensity changes, normalized to the peak intensity without pp-p38, for ATF2 backbone amide HSQC peaks for the 0.5:1 (black) or 1:1 (cyan) pp-p38:ATF2 experiment were plotted. The lower panel shows the results when ATF2 was mixed with nonphosphorylated p38 in 2:1 molar ratio. 'x' indicates resonances of residues which are not resolved in the spectra therefore could not be quantified or proline. The HSQC spectra of the pp-p38:ATF2 (0.5:1) and np-p38:ATF2(2:1) are shown in the left. Black peaks indicate the apo spectra of ATF2, whereas titrated ATF2 peaks are colored with red. C) NMR analysis of p38 binding to SPFENEFF motif peptides. 2D [^1H , ^{15}N] TROSY NMR spectra of [^2H , ^{15}N]-labeled double-phosphorylated p38 (pp-p38) or nonphosphorylated p38 (np-p38) alone (black) or in the presence of excess amounts (1:16 and 1:10 molar ratio, respectively) of the WT (ATF2wt) or S90N mutant (ATF2mut) SPFENEFF peptide (red).

Appendix Figure 3. Conservation analysis of ATF2-TAD (invertebrates) and p38-FRS

A) Co-occurrence of ATF2-type bZIP and ATF2 TAD elements in Opisthokonta. (Zn: C2H2 type zinc-finger, D: NFAT4 type docking motif, F: F-type S/NPFE/D..F motif). The analysis performed with BLASTp on non-redundant protein sequence database using human sequence templates of ATF2, ATF7 and CREB5. The thick line indicates a good match while the thin line indicates a weak match in the linker region between TAD and bZIP according to the BLASTp algorithm. Multiple alignments with selected sequences were performed using clustalX software. (SALR5 – *Salpingoeca rosetta*, CAPO3 – *Capsaspora owczarzakii*, SCHPO – *Schizosaccharomyces pombe*). * Note that *Salpingoeca rosetta* ATF2-TAD and bZIP module were found in two different transcripts. B) Evolution of ATF2-type transcription factors in Protostomata. Loss of the Zn-finger+D-motif module is observable in Nematoda and gradually in Diptera. (CAEEL – *Caenorhabditis elegans*, AEDEA – *Aedes aegypti*, CERCA – *Ceratitidis capitata*, DROME – *Drosophila melanogaster*). C) Evolutionary sequence conservation of p38 α through the animal kingdom (Metazoa) and yeast. Amino acids involved in the formation of the upper and lower pocket of the FRS are highlighted with red and cyan, respectively.

ADATLAP

a doktori értekezés nyilvánosságra hozatalához*

I. A doktori értekezés adatai

A szerző neve: Pongorné Kirsch Klára

MTMT-azonosító: 10052485

A doktori értekezés címe és alcíme: Non-canonical interactions of the Mitogen Activated Protein (MAP) kinases

DOI-azonosító⁴⁶: 10.15476/ELTE.2021.040

A doktori iskola neve: Biológia Doktori Iskola

A doktori iskolán belüli doktori program neve: Szerkezeti Biokémia Program

A témavezető neve és tudományos fokozata: Reményi Attila, Ph.D., D.Sc.

A témavezető munkahelye: Biomolekuláris Kölcsönhatások Kutatócsoport, Szerves Kémiai Intézet, Természettudományi Kutatóközpont

II. Nyilatkozatok

1. A doktori értekezés szerzőjeként

- a) hozzájárulok, hogy a doktori fokozat megszerzését követően a doktori értekezésem és a tézisek nyilvánosságra kerüljenek az ELTE Digitális Intézményi Tudástárban. Felhatalmazom a Természettudományi kar Dékáni Hivatali Doktori, Habilitációs és Nemzetközi Ügyek Csoportjának ügyintézőjét, hogy az értekezést és a téziseket feltöltse az ELTE Digitális Intézményi Tudástárba, és ennek során kitöltse a feltöltéshez szükséges nyilatkozatokat.
- b) kérem, hogy a mellékelt kérelemben részletezett szabadalmi, illetőleg oltalmi bejelentés közzétételéig a doktori értekezést ne bocsássák nyilvánosságra az Egyetemi Könyvtárban és az ELTE Digitális Intézményi Tudástárban;
- c) kérem, hogy a nemzetbiztonsági okból minősített adatot tartalmazó doktori értekezést a minősítés (*dátum*)-ig tartó időtartama alatt ne bocsássák nyilvánosságra az Egyetemi Könyvtárban és az ELTE Digitális Intézményi Tudástárban;
- d) kérem, hogy a mű kiadására vonatkozó mellékelt kiadó szerződésre tekintettel a doktori értekezést a könyv megjelenéséig ne bocsássák nyilvánosságra az Egyetemi Könyvtárban, és az ELTE Digitális Intézményi Tudástárban csak a könyv bibliográfiai adatait tegyék közzé. Ha a könyv a fokozatszerzést követően egy évig nem jelenik meg, hozzájárulok, hogy a doktori értekezésem és a tézisek nyilvánosságra kerüljenek az Egyetemi Könyvtárban és az ELTE Digitális Intézményi Tudástárban.

2. A doktori értekezés szerzőjeként kijelentem, hogy

- a) az ELTE Digitális Intézményi Tudástárba feltöltendő doktori értekezés és a tézisek saját eredeti, önálló szellemi munkám és legjobb tudomásom szerint nem sértem vele senki szerzői jogait;
- b) a doktori értekezés és a tézisek nyomtatott változatai és az elektronikus adathordozón benyújtott tartalmak (szöveg és ábrák) mindenben megegyeznek.

3. A doktori értekezés szerzőjeként hozzájárulok a doktori értekezés és a tézisek szövegének plágiumkereső adatbázisba helyezéséhez és plágiumellenőrző vizsgálatok lefuttatásához.

Kelt: 2021. 03. 18.


.....
a doktori értekezés szerzőjének aláírás

*ELTE SZMSZ SZMR 12. sz. melléklet